

REPORT DOCUMENTATION PAGE

Form Approved
OMB No. 0704-0188

Public reporting burden for this collection of information is estimated to average 1 hour per response, including the time for reviewing instructions, searching existing data sources, gathering and maintaining the data needed, and completing and reviewing this collection of information. Send comments regarding this burden estimate or any other aspect of this collection of information, including suggestions for reducing this burden to Department of Defense, Washington Headquarters Services, Directorate for Information Operations and Reports (0704-0188), 1215 Jefferson Davis Highway, Suite 1204, Arlington, VA 22202-4302. Respondents should be aware that notwithstanding any other provision of law, no person shall be subject to any penalty for failing to comply with a collection of information if it does not display a currently valid OMB control number. **PLEASE DO NOT RETURN YOUR FORM TO THE ABOVE ADDRESS.**

1. REPORT DATE 30-11-2011	2. REPORT TYPE Final Report	3. DATES COVERED 14 March 2008 to 30 Nov.2011
------------------------------	--------------------------------	--

4. TITLE AND SUBTITLE Nonlinear Structural Health Monitoring of the Responsive Space Satellite Systems using Magneto Elastic Active Sensors (MEAS)	5a. CONTRACT NUMBER FA9550-08-1-0128
---	---

	5b. GRANT NUMBER
--	------------------

	5c. PROGRAM ELEMENT NUMBER
--	----------------------------

6. AUTHOR(S) Zagrai, Andrei N.	5d. PROJECT NUMBER
---------------------------------------	--------------------

	5e. TASK NUMBER
--	-----------------

	5f. WORK UNIT NUMBER
--	----------------------

7. PERFORMING ORGANIZATION NAME(S) AND ADDRESS(ES) New Mexico Institute of Mining and Technology	8. PERFORMING ORGANIZATION REPORT NUMBER
---	--

--	--

801 Leroy Place Socorro, NM 87801	
--------------------------------------	--

9. SPONSORING / MONITORING AGENCY NAME(S) AND ADDRESS(ES) USAF, AFRL	10. SPONSOR/MONITOR'S ACRONYM(S)
---	----------------------------------

AFOSR / PKC	
-------------	--

875 Randolph St. Room 3112	11. SPONSOR/MONITOR'S REPORT NUMBER(S)
----------------------------	--

Arlington, VA 22203	AFRL-OSR-VA-TR-2012-0237
---------------------	--------------------------

12. DISTRIBUTION / AVAILABILITY STATEMENT A
--

13. SUPPLEMENTARY NOTES

14. ABSTRACT

The project explores application of magneto-elastic active sensors (MEAS) for structural health monitoring (SHM) of responsive space satellite systems. Design, development and fabrication procedures for MEAS are presented and associated electrical and mechanical characteristics are discussed. MEAS miniaturization efforts are highlighted. Examples of MEAS-enabled SHM testing in aerospace structures of simple and complex geometry, such a honeycomb and realistic satellite panels, are provided. Nonlinear SHM methodologies using MEAS are considered and its use for acousto-elastic assessment of bolted joints is recommended. A new SHM methodology - magneto-mechanical impedance (MMI) testing is suggested and explored from both theoretical and practical perspectives. The MMI measurement technique demonstrates ability for non-contact structural dynamic measurements and effectiveness in detection of fatigue damage at early stage, well before onset of fracture and crack development. Analytical and numerical models of MEAS and MMI are suggested. Finally, MEAS capability for recording dynamics of payload during sub-orbital space flight is validated. The results of the sub-orbital flight measurements suggest feasibility of using MEAS in space environment although characterization of dynamic events was not possible due to limitation of the on-board data acquisition system. It is advocated that MEAS could find its own niche in traditional and innovative SHM methodologies.

15. SUBJECT TERMS

Structural health monitoring, magnetic, magneto-elastic, embedded ultrasonics, nonlinear diagnostics, space structures, structural joints, sub-orbital.

16. SECURITY CLASSIFICATION OF:	17. LIMITATION OF ABSTRACT	18. NUMBER OF PAGES	19a. NAME OF RESPONSIBLE PERSON
---------------------------------	----------------------------	---------------------	---------------------------------

a. REPORT	b. ABSTRACT	c. THIS PAGE	Andrei Zagrai
-----------	-------------	--------------	---------------

			19b. TELEPHONE NUMBER 575-835-5636
--	--	--	---------------------------------------

Nonlinear Structural Health Monitoring of the Responsive Space Satellite Systems using Magneto Elastic Active Sensors (MEAS)

Andrei Zagrai^{*}, Timothy Barnes[†], Davit Kukhalashvili[†], Rakhim Aitbaev[‡] and David Conrad[†].

New Mexico Institute of Mining and Technology,
Department of Mechanical Engineering
801 Leroy Pl., Socorro, NM 87801
575-835-5636, Fax 575-835-5209, azagrai@nmt.edu

Award Number: FA9550-08-1-0128

Date: November 30, 2011

^{*} Associate Professor and PI,

[†] Graduate Student, [‡] Associate Professor

ABSTRACT

The project explores application of magneto-elastic active sensors (MEAS) for structural health monitoring (SHM) of responsive space satellite systems. Design, development and fabrication procedures for MEAS are presented and associated electrical and mechanical characteristics are discussed. MEAS miniaturization efforts are highlighted. Examples of MEAS-enabled SHM testing in aerospace structures of simple and complex geometry, such a honeycomb and realistic satellite panels, are provided. Nonlinear SHM methodologies using MEAS are considered and its use for acousto-elastic assessment of bolted joints is recommended. A new SHM methodology – magneto-mechanical impedance (MMI) testing is suggested and explored from both theoretical and practical perspectives. The MMI measurement technique demonstrates ability for non-contact structural dynamic measurements and effectiveness in detection of fatigue damage at early stage, well before onset of fracture and crack development. Analytical and numerical models of MEAS and MMI are suggested. Finally, MEAS capability for recording dynamics of payload during sub-orbital space flight is validated. The results of the sub-orbital flight measurements suggest feasibility of using MEAS in space environment although characterization of dynamic events was not possible due to limitation of the on-board data acquisition system. It is advocated that MEAS could find its own niche in traditional and innovative SHM methodologies.

Table of Contents

1	INTRODUCTION.....	1
1.1	MOTIVATION	1
1.2	PRIOR WORK AND STATE OF THE ART	2
2	RESEARCH ACCOMPLISHMENTS.....	4
2.1	MAGNETO-ELASTIC ACTIVE SENSOR (MEAS) DEVELOPMENT AND CHARACTERIZATION	4
2.1.1	<i>Pancake MEAS</i>	4
2.1.2	<i>MEAS Miniaturization</i>	17
2.1.3	<i>Shear-Wave MEAS</i>	21
2.2	MEAS APPLICATION IN MAGNETO-MECHANICAL IMPEDANCE (MMI) TECHNOLOGY.....	25
2.2.1	<i>Overview of the MMI Technology</i>	25
2.2.2	<i>MMI Analytical Modeling</i>	27
2.2.3	<i>Semi-Analytical MMI Model for Complex Structures</i>	34
2.2.4	<i>Examples of MMI SHM Applications</i>	35
2.3	MEAS MODELING.....	43
2.3.1	<i>Finite Element Model using COMSOL</i>	43
2.3.2	<i>Point-source Heuristic Model of MEAS</i>	45
2.4	MEAS APPLICATION IN WAVE PROPAGATION SHM	47
2.4.1	<i>Far-Field Crack Detection</i>	47
2.4.2	<i>Near-Field Crack Detection</i>	49
2.4.3	<i>Detection of Disbonds in Honeycomb Panels</i>	50
2.5	NONLINEAR SHM WITH MEAS	52
2.5.1	<i>Acousto-elastic Assessment of Bolted Joints in Elastic Plates</i>	52
2.5.2	<i>Magneto-Mechanical Impedance Acousto-Elastic Assessment of Realistic Satellite Panel</i>	55
2.5.3	<i>Multiple Harmonic Resonance Tests</i>	57
2.6	MAGNETO-ELASTIC SENSING DURING SUB-ORBITAL FLIGHT.....	59
3	CONCLUSIONS	63
4	PROJECT PERSONNEL.....	64
5	PUBLICATIONS	64
5.1	JOURNAL PAPERS.....	64
5.2	CONFERENCE PAPERS	64
6	ACKNOWLEDGMENTS	65
7	REFERENCES.....	65

List of Figures

FIGURE 1	ELECTRO-MAGNETIC-ELASTIC INTERACTION OF A SENSOR AND A METALLIC STRUCTURE.	1
FIGURE 2	SCHEMATICS OF MEAS ASSEMBLY.	4
FIGURE 3	PLOT OF TRANSDUCER SIGNAL STRENGTH AS A FUNCTION OF NUMBER OF TURNS IN THE COIL.....	7
FIGURE 4	PLOT OF RECEIVED SIGNAL AMPLITUDE VS. NUMBER OF MAGNETS ON TOP OF TRANSDUCER B8.	8
FIGURE 5	PLOT OF RECEIVED AMPLITUDE VERSUS FREQUENCY FOR A NUMBER OF MEAS TRANSDUCERS.....	9
FIGURE 6	COMPARISON OF MEAS FRF ON ALUMINUM AND COPPER.	9
FIGURE 7	COMPARISON OF THE FREQUENCY RESPONSE FUNCTIONS OF PWAS AND 0.75-INCH DIAMETER MEAS.....	9
FIGURE 8	DIRECTIVITY PLOT FOR TRANSDUCER C-1.....	10
FIGURE 9	EXPERIMENTAL SETUP FOR DIRECTIVITY MEASUREMENT.....	10
FIGURE 10	IMPEDANCE MATCHING CIRCUIT RECOMMENDED BY RITEC.....	10
FIGURE 11	REAL (A) AND IMAGINARY (B) PARTS OF IMPEDANCE FOR FOUR MEAS. SOLID CURVES SHOW EXPERIMENTAL DATA; DASHED LINES REPRESENT LEAST-SQUARES LINEAR FIT.	11
FIGURE 12	SCHEMATIC OF MATCHING CIRCUITS.	12
FIGURE 13	PHOTOGRAPH OF ACTUAL TEST CIRCUIT.	12
FIGURE 14	FREQUENCY RESPONSE FOR TRANSDUCER B-6 (A) AND B-9 (B), WITH AND WITHOUT L-MATCHING.....	13
FIGURE 15	FREQUENCY RESPONSE OF TRANSDUCERS B-5 AND B-10 WITH TRANSFORMER MATCHING.....	14
FIGURE 16	(A) RECEIVED SIGNAL AMPLITUDE TRANSMITTED FROM C3 AND RECEIVED WITH A PWAS. (B) FRF OF C3, CORRECTED FOR FREQUENCY RESPONSE OF PWAS.	15
FIGURE 17	COMPARISON OF FRFs OF TRANSDUCER C3 WITH AND WITHOUT AN IMPEDENCE-BALANCING CAPACITOR.....	15
FIGURE 18	FRF OF VARIOUS TRANSDUCERS WITH CAPACITIVE IMPEDANCE MATCHING.....	16
FIGURE 19	COMPARISON OF SIGNAL FRF WITH VARIOUS IMPEDANCE-MATCHED RECEIVERS.	17
FIGURE 20	TYPICAL MINIATURIZED MEAS.....	19
FIGURE 21	COMPARISON OF TRANSDUCER SIZE. FROM LEFT TO RIGHT: C1, E2, E5.	19
FIGURE 22	COMPARISON OF MEAS FRFs AS MEASURED BY A PWAS RECEIVER.	19
FIGURE 23	MINIATURE MEAS SIGNAL AT VARIOUS FREQUENCIES.	20
FIGURE 24	FREQUENCY RESPONSE OF E1 AND E3, RECEIVING WITH E2.....	20
FIGURE 25	SIGNAL TRANSMITTED AND RECEIVED WITH E5 AND E6 FOR VARIOUS LEVELS OF SIGNAL AVERAGING.	20
FIGURE 26	SIGNAL TRANSMITTED AND RECEIVED WITH E1 AND E2 FOR VARIOUS LEVELS OF SIGNAL AVERAGING.	21
FIGURE 27	EXPLODED VIEW OF RACETRACK COIL MEAS FOR SH-WAVE EXCITATION, SHOWING PERIODIC PERMANENT MAGNET ARRAY (PPM), COIL, AND COPPER MASK.	21
FIGURE 28	PHOTOGRAPHS OF TRANSDUCERS D5 (A) AND D2 (B), CONSISTING OF A MASKED RACETRACK COIL AND PPM ARRAY WITH A HALF-PERIOD OF 1/4 AND 1/32 OF AN INCH RESPECTIVELY.....	22
FIGURE 29	TRANSDUCTION PATTERN REQUIRED FOR OMNIDIRECTIONAL SH MEAS. BLUE ARROWS SHOW MAGNETIC FIELD, YELLOW ARROWS SHOW INDUCED EDDY CURRENTS, RED	

	ARROWS SHOW LORENTZ FORCE DIRECTION AND RESULTING LATTICE DISPLACEMENT.	22
FIGURE 30	TOROIDAL EXCITATION COIL.	22
FIGURE 31	PROTOTYPE OF OMNIDIRECTIONAL SH-WAVE MEAS.	23
FIGURE 32	DISPERSION DATA FOR OMNIDIRECTIONAL TRANSDUCER C-1 (A) AND SH MEAS D-1.	23
FIGURE 33	TYPICAL SIGNAL TRANSMITTED BY TOROIDAL-COIL MEAS AND RECEIVED BY PWAS.	24
FIGURE 34	EXPERIMENTAL SETUP FOR MMI MEASUREMENTS USING HP4192A PHASE GAIN IMPEDANCE ANALYZER.	25
FIGURE 35	MMI RESPONSES OF THE ALUMINUM BEAM MEASURED WITH MEAS-1 AND MEAS-2.	26
FIGURE 36	STRUCTURAL RESPONSES EXTRACTED FROM MMI SIGNATURES AND SUPERIMPOSED THEORETICALLY CALCULATED NATURAL FREQUENCIES OF THE FREE-FREE ALUMINUM BEAM.	26
FIGURE 37	(A) MAGNETO-MECHANICAL AND ELECTRO-MECHANICAL IMPEDANCES OF SMALL ALUMINUM BEAMS. (B) DETAILS OF MMI AND EMI RESPONSES AT 5 KHZ.	27
FIGURE 38	VERTICAL COMPONENT OF THE EXCITATION FORCE EXERTED BY MEAS ONTO THE METALLIC STRUCTURE: (A) SINGLE-POINT LOAD, (B) PIN-FORCE LOAD, (C) TRIANGULAR LOAD.	28
FIGURE 39	EQUIVALENT CIRCUIT FOR MAGNETO-ELASTIC ACTIVE SENSING.	31
FIGURE 40	THEORETICALLY CALCULATED AND EXPERIMENTALLY MEASURED MMI RESPONSES OF AN ALUMINUM BEAM. BROADBAND (A) AND NARROWBAND (B), (C), (D) REPRESENTATIONS OF MMI.	33
FIGURE 41	EFFECT OF RESISTANCE (A) AND INDUCTANCE (B) OF THE STRUCTURAL ELEMENT ON THE MAGNETO-MECHANICAL IMPEDANCE.	34
FIGURE 42	(A) GEOMETRY OF THE DOG-BONE SPECIMEN USED IN FEA; (B) FEA RESULTS FOR ONE OF VIBRATION MODES OF THE DOG-BONE SPECIMEN.	35
FIGURE 43	COMPARISON OF EXPERIMENTAL AND THEORETICAL MMI RESPONSES OF THE DOG-BONE SPECIMEN.	35
FIGURE 44	ALUMINUM BEAM USED IN EXPERIMENTS.	36
FIGURE 45	MAGNETO-MECHANICAL IMPEDANCE OF BEAMS (A) AND (B,C,D) WITH SELECTED ZOOM-IN.	36
FIGURE 46	DOG-BONE SPECIMENS MEASURED IN TEST.	37
FIGURE 47	DOG-BONE SPECIMENS MMI SIGNATURES.	37
FIGURE 48	MAGNETO-MECHANICAL IMPEDANCE OF THE S3B SAMPLE (A) WITH SELECTED ZOOM-IN PEAKS (B,C,D).	39
FIGURE 49	MAGNETO-MECHANICAL IMPEDANCE OF THE S3Ba SAMPLE (A) WITH SELECTED ZOOM-IN PEAKS (B,C,D).	39
FIGURE 50	MAGNETO-MECHANICAL IMPEDANCE OF THE S5B SAMPLE (A) WITH SELECTED ZOOM-IN PEAKS (B,C,D).	40
FIGURE 51	MAGNETO-MECHANICAL IMPEDANCE OF THE SYB SAMPLE (A) WITH SELECTED ZOOM-IN PEAKS (B,C,D).	40
FIGURE 52	SYB AND BROKEN SXB DOG-BONE SPECIMENS.	41
FIGURE 53	SIDE VIEW OF ALUMINUM HONEYCOMB PANEL (A) AND MEAS LOCATIONS IN ASSOCIATED EXPERIMENTS (B).	42
FIGURE 54	IMPEDANCE SIGNATURES COLLECTED AT INDICATED LOCATIONS ON A FRONT SIDE OF THE HONEYCOMB PANEL.	42
FIGURE 55	IMPEDANCE SIGNATURES COLLECTED AT INDICATED LOCATIONS ON A BACK SIDE OF THE HONEYCOMB PANEL.	42

FIGURE 56	INFINITE WIRE: THE RELATIVE ERROR OF THE NUMERICAL SOLUTION FOR THE MAGNETIC INDUCTION ALONG THE X-AXIS.....	44
FIGURE 57	CIRCULAR WIRE: (A) THE NUMERICAL SOLUTION FOR THE MAGNETIC INDUCTION FIELD; (B) THE EXACT (RED) AND THE NUMERICAL (BLUE) SOLUTIONS ON Z-AXIS.	44
FIGURE 58	(A) FE MESH OF 2-D AXISYMMETRIC MMI MODEL; (B) EXAMPLE OF CALCULATED MAGNETO-MECHANICAL IMPEDANCE.	44
FIGURE 59	(A) SURFACE PLOT OF CURRENT DENSITY IN VICINITY OF MEAS. (B) PLOT OF PARTICLE VELOCITY WITHIN THE PLATE UNDER THE TRANSMITTING MEAS SHOWING PROPAGATING LAMB WAVE.	45
FIGURE 60	COMPARISON OF MEASURED AND MODELED MEAS SIGNALS AT VARIOUS FREQUENCIES, TAKING EFFECTIVE EXCITATION DIAMETER INTO ACCOUNT.	46
FIGURE 61	SENSOR PAIR POSITIONS FOR PITCH-CATCH CRACK DETECTION EXPERIMENT. ``	47
FIGURE 62	TYPICAL SIGNAL THROUGH CRACK. FIRST PULSE IS S_0 ; SECOND AND THIRD ARE ECHOES.	47
FIGURE 63	ENVELOPE OF SIGNAL TRANSMITTED THROUGH CRACK FOR VARIOUS POSITIONS OF MEAS PAIR.	47
FIGURE 64	EFFECT OF DISTANCE ON SIGNAL AMPLITUDE REDUCTION CAUSED BY A CRACK ON THE WAVE PROPAGATION PATH.	48
FIGURE 65	POSITION OF SENSOR PAIRS FOR FAR-FIELD CRACK DETECTION ON FATIGUED PLATE. ...	48
FIGURE 66	COMPARISON OF RECORDED PULSES FOR SENSOR PAIRS WITH 4" AND 8" SEPARATION ON FATIGUED PLATE.	48
FIGURE 67	ILLUSTRATION OF SENSOR PLACEMENT FOR NEAR-FIELD CRACK DETECTION EXPERIMENT.....	49
FIGURE 68	WAVEFORMS AND SIGNAL ENVELOPS OBTAINED IN NEAR-FIELD CRACK DETECTION EXPERIMENT.....	49
FIGURE 69	A TYPICAL ALUMINUM HONEYCOMB PANEL.....	50
FIGURE 70	DIAGRAM OF DISBOND AND SENSOR LOCATIONS ON HONEYCOMB PANEL.....	50
FIGURE 71	SIGNALS FROM HONEYCOMB PANEL EXPERIMENT TRANSMITTED PERPENDICULAR TO PLATE EDGES AND REFLECTED BACK TO RECEIVER.....	51
FIGURE 72	SIGNALS FROM HONEYCOMB PANEL EXPERIMENT TRANSMITTED PARALLEL TO THE PLATE EDGES.	51
FIGURE 73	ILLUSTRATION OF BOLTED JOINT.	52
FIGURE 74	SIGNALS TRANSMITTED THROUGH BOLTED JOINT AT FIVE CONDITIONS OF THE CENTRAL BOLT.....	52
FIGURE 75	SIGNALS TRANSMITTED THROUGH BOLTED JOINT AT VARIOUS TORQUE LEVELS.....	53
FIGURE 76	(A) ENVELOPES OF SIGNALS TRANSMITTED THROUGH THE BOLTED JOINT, (B) MEASURED SIGNAL AMPLITUDE AS A FUNCTION OF BOLT TORQUE.....	53
FIGURE 77	ZOOMED-IN VIEW OF A PORTION OF THE SIGNAL SHOWN IN FIGURE 75.....	53
FIGURE 78	MEAS POSITION ON BOLTED PLATES IN 4 EXPERIMENTS.	54
FIGURE 79	SIGNAL RECORDS CORRESPONDING TO "TIGHT" AND "LOOSE" CONDITIONS OF A BOLT FOR EXPERIMENTS 1 (A), 2 (B), 3 (C) AND 4 (D).....	54
FIGURE 80	A REALISTIC SATELLITE PANEL CONSISTING OF TWO ALUMINUM PLATES WITH ISO-GRID FRAMES ON THE BACK SIDE (A), (B) DETAILS OF THE ISO-GRID STRUCTURE.	55
FIGURE 81	MEAS WITH A SHIELDING COVER AND CABLE CONNECTION REMOVED FOR CLARITY OF ILLUSTRATION.....	55
FIGURE 82	MMI CHARACTERISTICS OF THE DE34 QUADRANT DURING INCREMENTAL LOOSENING OF STRUCTURAL BOLTS.....	56
FIGURE 83	ENERGY DISTRIBUTIONS CALCULATED FOR MMI RESPONSES OBTAINED IN THE MMI CHARACTERISTICS OF THE DE34 QUADRANT (INCREMENTAL LOOSENING).....	56

FIGURE 84	MMI CHARACTERISTICS OF THE DE34 QUADRANT DURING INCREMENTAL TIGHTENING OF STRUCTURAL BOLTS.....	57
FIGURE 85	ENERGY DISTRIBUTIONS CALCULATED FOR MMI RESPONSES OBTAINED IN THE MMI CHARACTERISTICS OF THE DE34 QUADRANT (INCREMENTAL TIGHTENING).....	57
FIGURE 86	FREQUENCY RESPONSES OF THE S4B DOG-BONE SPECIMEN MEASURED USING RITEC AT FUNDAMENTAL AND HARMONIC (2 ND AND 3 RD) FREQUENCIES.	58
FIGURE 87	SPACELOFT XL VEHICLE. (WWW.UPAEROSPACE.COM).	59
FIGURE 88	EXAMPLE OF MEAS RECORD COLLECTED DURING LABORATORY TESTING.....	59
FIGURE 89	INTERIOR OF NMIMT PAYLOAD.	60
FIGURE 90	UNSYNCHRONIZED MEAS IN-FLIGHT DATA DOWNLOADED FROM THE MICROCONTROLLER UNIT.	60
FIGURE 91	MEAS RECORD DURING SL5 FLIGHT.....	61
FIGURE 92	ZOOM INTO MEAS IN-FLIGHT RECORD.....	61
FIGURE 93	SL5 LAUNCH ON MAY 20, 2011; (B) FLIGHT PROFILE OF SL5.	62
FIGURE 94	ALTITUDE AND ACCELERATION OF SL5 ROCKET.....	62

List of Tables

TABLE 1: COIL TYPE EXPERIMENT.....	5
TABLE 2: WINDING STYLE EXPERIMENT	6
TABLE 3: WIRE DIAMETER EXPERIMENT.....	6
TABLE 4: MAGNET GRADE AND THICKNESS.....	8
TABLE 5: IMPEDANCE MATCHING SOLUTIONS AT 300 KHz	11
TABLE 6: VOLTAGE STEP-UP RATIOS FOR MEAS	13
TABLE 7: IMPEDANCE OF TRANSDUCERS FROM FIGURE 19	17
TABLE 8 FATIGUE CHARACTERISTICS OF EXPERIMENTAL SAMPLES IN MMI TESTS.	38
TABLE 9: DISTANCE BETWEEN SENSORS IN FIGURE 61	47
TABLE 10: SENSOR POSITIONS FOR NEAR-FIELD EXPERIMENT.....	49

1 INTRODUCTION

1.1 Motivation

Modern structural health monitoring (SHM) increasingly relies on a diverse suite of sensing technologies. Because of their high efficiency, Piezoelectric Wafer Active Sensors (PWAS) are widely used (Boller et al. 2009). However, PWAS suffer from a number of inherent limitations. Many of these limitations arise from the necessity to adhesively bond the transducer to the host structure. In particular, the rigid bond between the sensor and the structure effectually makes the sensor part of the structure, slightly altering its local stiffness and mass distribution. In most practical cases this effect is negligible (Giurgiutiu, 2007), as PWAS are small (6mm diameter by <1mm thick is typical), but for very delicate structures or very sensitive measurements, this can be problematic. Moreover, because the adhesive layer must translate mechanical strains between the PWAS and the host structure, signal integrity becomes critically dependent upon bond integrity, and if the sensor is not adequately bonded to the structure, or if the adhesive should lose its adherence to either the sensor or the host structure, the sensor's ability to transmit and receive elastic waves is impaired. Though methods exist for system self-diagnosis and automated detection of debonded sensors (Park, 2009), this remains an inherent limitation of PWAS. It is desirable to improve survivability of SHM sensors and eliminate, if possible, dependence of monitoring results on the quality of a bond layer between the sensors and the structure.

Magneto-Elastic Active Sensors (MEAS), the term derived by analogy to PWAS, offer an alternative to piezoelectric sensors with the potential to overcome the shortcomings indicated above. In the most general case, a MEAS consists of a wire, or collection of wires, in close proximity to a conductive structure, and positioned within a magnetic field supplied by a permanent magnet. When an electrical current is passed through the wire, eddy currents will be induced in the host structure, and the interaction of these eddy currents with the magnetic field will produce elastic waves within the structure (Banik and Overhauser, 1977 and Quinn, 1967). Illustration of MEAS configuration and respective orientation of applied magnetic field, induced eddy current and resultant forces is presented in Figure 1. Although a number of phenomena may contribute to wave excitation, the Lorentz force mechanism governing transduction in nonferrous metals will be considered because the majority of metallic structures for space applications are made from aluminum alloys. The pattern of transduction for a given MEAS is dependent upon mutual orientation of coil windings and applied magnetic field and a variety of different configurations are possible. Because the electromagnetic-acoustic transduction also works in reverse,

MEAS can be used for passive sensing and reception of actively generated elastic wave; therefore, operating as a transmitter and receiver. A unique aspect of MEAS is that because the transduction takes place within the host structure itself, there is no need for a mechanical connection between host structure and the MEAS, and hence non-contact measurements with MEAS are possible. In practice, the MEAS may still be glued to the host structure, but adhesive layer is anticipated to have negligible effect upon the transduction. Therefore, MEAS may be

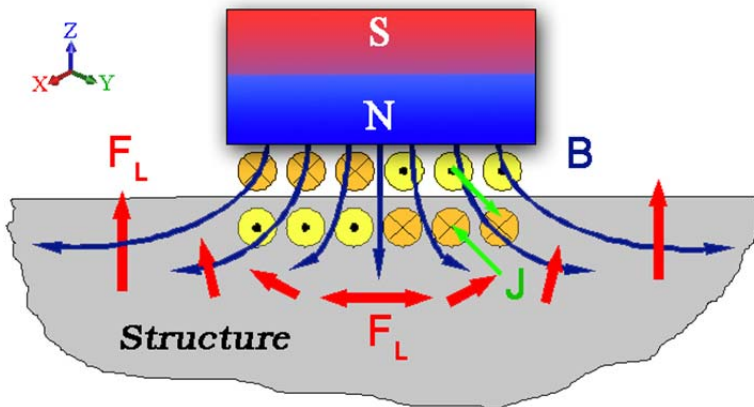


Figure 1 Electro-magnetic-elastic interaction of a sensor and a metallic structure.

used in high temperature applications (limited by permanent magnet and material used in assembly), through paint/dirt inspection and other non-contact applications requiring a small separation gap between the sensor and structure. It should be noted that the transduction mechanism employed by MEAS is similar to that of Electro-Magnetic Acoustic Transducers (EMATs). However, in contrast to EMATs, MEAS design is miniaturized and optimized for embedded applications in SHM and configured to enable magneto-mechanical impedance SHM methodology.

1.2 Prior Work and State of the Art

In 1969, James R. Houck, Henry V. Bohm, and Bruce W. Maxfield patented an ultrasonic transducer that embodied what would come to be known as an EMAT. After the invention was patented, Maxfield *et al* published a paper on the design of permanent-magnet EMATs, in which they discuss the construction of “compact” (weighed 250 grams) EMATs using then-newly-available samarium-cobalt permanent magnets (1976). They also predicted (quite accurately) that in the future, improvements in high-current ultrasonic equipment and real-time signal averaging would increase the signal-to-noise ratio (SNR) of compact EMATs sufficiently to make them practical for NDE applications. (Maxfield *et al*, 1976). The same year, C. M. Fortunko and R. B. Thompson (1976) published a paper on EMAT optimization. In it, they present a number of excitation coil designs, including the flat circular spiral now known as a “pancake coil,” the “serpentine coil,” better known as a meanderline, and a masked double-spiral coil for generating shear waves. Recent study by Aliouane *et al* (2000) presented a prototype EMAT design, and discussed the effects sensor liftoff, static field excitation current, composition of the host structure, and coil design upon EMAT efficiency and wave mode generation. Their prototype design consisted of a PCB excitation coil situated between the poles of an electromagnetic yoke, the whole assembly being surrounded by a cylindrical metallic shield to form a “compact” transducer. Though exact overall dimensions were not specified, their transducer appears to have been about 1.5 inches in diameter by about 1.5 inches in height. Wilcox *et al* (2005) performed an experimental study of omni-directional pancake-coil EMAT design, pursuant to construction of an omnidirectional EMAT array for manual inspection of large plate structures. Their study yielded five conclusions: First, that as long as the inner diameter of the pancake coil is less than half of the outer diameter, it plays no significant role in determining EMAT performance parameters. Second, that for the particular EMAT design and equipment that they were using, the EMAT frequency response function peaks at a frequency such that the wavelength of the transmitted elastic wave is equal to about two thirds the outer diameter of the excitation coil. Third, that when the transducer is driven at the peak response frequency for the S_0 lamb-wave mode, the amplitude of the transmitted A_0 mode is about an order of magnitude lower than that of the S_0 mode. Fourth, that in reception, EMAT efficiency is directly proportional to the number of turns in the coil. And fifth, that in transmission, EMAT efficiency peaks at a finite number of turns, which is determined by electrical impedance-matching considerations. Boonsang and Dewhurst (2005) investigated the design of high-sensitivity EMAT receiver systems. The research, however, focused more on a novel preamplifier designs to enhance the effective signal-to-noise ratio of the EMAT receiver, when an on-board preamplifier circuit was built into the receiving transducer. Jian and Dixon (2006) studied the effect of coil backing material on the performance of eddy current probes and EMATs. The authors derived an analytic solution to estimate the magnitude of the eddy currents induced in metallic structures by excitation coils with different kinds of backing, and concluded that for maximum efficiency, it is desirable to employ a backing material with high magnetic permeability but low electrical conductivity. This conclusion was verified experimentally, using an excitation coil alternately with no back plate, an aluminum back plate, or a ferrite back plate. Experimental results showed that the ferrite backing provided the best transduction efficiency, followed by the air backing, with the aluminum backing last. Dutton *et al* (2006) used finite element techniques to model magnetic fields in the vicinity permanent magnets used for EMAT construction for the purpose of refining EMAT design for hybrid laser-EMAT ultrasound systems. The EMAT consisted of a small

N38SH neodymium disc magnet with an 80-turn coil of magnet wire wound longitudinally around the disc to form a rectangular coil, with the rectangle in a plane perpendicular to the plate being inspected. They then used FEMLAB (a precursor of COMSOL) software to create a finite element model of the magnet, and also to model the field around two small N38SH block magnets in close proximity to one another with like poles facing each other. The model showed a significantly stronger field between the two block magnets than over the surface of the disc magnet.

In summary, the development of the EMAT, and particularly the compact EMATs made possible by high-strength permanent magnets, laid the groundwork for the development of MEAS, a MEAS being an ultra-compact EMAT employed in embedded SHM applications instead of manual NDE. As such, the many contributions of the above researchers to refinement and modeling of EMATs deserve due recognition. However, even the “compact” transducer prototypes described in the literature are prohibitively large and/or expensive for many embedded SHM applications. Typical sizes for the most compact EMATs appear to be on the order of a cubic inch. Thus, further research and refinement of the EMAT concept is necessary to develop a truly embeddable EMAT, or rather MEAS.

While MEAS overcome many of the limitations of PWAS by virtue of the employed non-contact transduction mechanism it suffers from one significant shortcoming: low efficiency. Because of their low efficiency, MEAS have not found application in SHM heretofore. In EMATs, the low transduction efficiency has been overcome by a variety of means. Traditionally, resonance-based methods dominated the use of EMATs in NDE, for the reason that if many signals are coherently superimposed the observed signal amplitude is greatly increased (Hirao & Ogi, 2003). Resonance methods may find significant use in SHM, but to serve as a replacement for PWAS, MEAS must also be able to send and receive individual acoustic signals and enable popular SHM methodologies such as pitch-catch ultrasonics, nonlinear diagnosis, and dynamic mechanical impedance assessment. The purpose of this report is to present developments towards achieving this goal.

2 RESEARCH ACCOMPLISHMENTS

2.1 Magneto-Elastic Active Sensor (MEAS) Development and Characterization

Embedded ultrasonics is a significant field of study in SHM (Boller et al., 2009). This inspection format is typically carried out using a small circular PWAS (Piezoelectric Wafer Active Sensor) to produce a nearly-omnidirectional radiation of ultrasonic guided waves. Therefore, an omnidirectional MEAS for generating guided waves would be immediately applicable to a variety of SHM techniques already developed for PWAS. Moreover, such a transducer should be readily realizable, as a pancake coil with an axially polarized disc magnet mounted atop it should generate the required Lorentz force distribution to effect omnidirectional guided waves generation (e.g. Wilcox *et al*, 2005). In realizing a miniaturized and potentially embeddable MEAS both fabrication aspects and studies of factors affecting MEAS efficiency were considered and discussed below.

2.1.1 Pancake MEAS

2.1.1.1. Fabrication of MEAS

The MEAS transducers were fabricated in-house. Such fabrication allows the transducer design to be freely modified, and yet was much cheaper than outsourcing fabrication to a custom transducer manufacturer. The mechanical construction of the MEAS is less trivial than might initially be supposed. Depending upon coil design, it may be necessary to insulate the coil electrically from its surroundings, which can be accomplished by application of a polymer film, such acrylic packing tape, to both sides of the flat coil. Unfortunately, the insulating polymer film applied to the coil tends to complicate the problem of bonding it to the required permanent magnet. In this study, both conventional epoxy and cyanoacrylate adhesives proved incapable of forming a bond with the acrylic tape. The solution for assembly of the transducer came in the form of a double-sided fiberglass mesh adhesive tape, which was capable of forming a strong, resilient bond with both the acrylic insulation applied to PCB coils and the nickel-plated surface of the neodymium magnets. A schematic of this basic transducer assembly is shown in Figure 2. Further details of MEAS fabrication can be found in the MS thesis of Mr. Timothy Barnes.

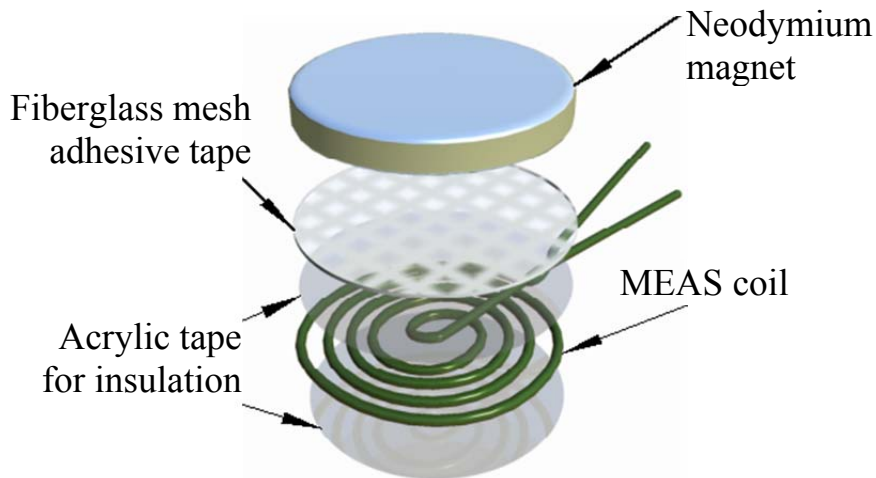


Figure 2 Schematics of MEAS assembly.

2.1.1.2. Factors Affecting MEAS Signal Amplitude

In order to explore the affect of various MEAS design parameters on signal amplitude, a series of experiments were conducted. In each case, several MEAS were fabricated, varying only the parameter of interest from one sensor to another. These sensors were then alternately placed at a marked location

on a thin plate of 6061-T6 alloy Aluminum, and connected to the gated-amplifier output of a RITEC RAM-5000 system. The RAM-5000 was employed to excite each transducer with a tone burst signal. The sensor was not bonded to the plate, but if necessary, a small mass of non-conductive material was placed on top of the sensor to ensure that it lay flat on the surface and prevent it from moving. A PWAS, bonded to the surface of the aluminum plate was utilized to measure the elastic wave generated by the MEAS. The output signal of the PWAS was measured with a National Instruments PXI-4152 14-bit digitizer sampling at 100 mega-samples/second. The peak amplitude of the received tone burst was taken as a measure of the signal strength. To quantify the level of random error that could be expected in such measurements, an initial set of ten independent measurements of MEAS B8 output were taken. The results suggest rather low variability of measurement results with the standard deviation reaching only one percent. However, it should be kept in mind that, due to amplification capability of the measurement system, signal amplitudes reported for any given experiment were measured using the same gain, and are thus comparable, but amplitudes from separate experiments reported herein are not necessarily commensurate.

2.1.1.2.1. Coil Type

There are two primary types of coils that may be used in MEAS construction: Printed Circuit Board (PCB) coils and wound wire coils. At the outset of this study, a few coils of each type were fabricated, and incorporated into MEAS transducers. The amplitude of signals produced by the transducers was measured and compared; the results are recorded in Table 1. Clearly, of the transducers tested, those with wound coils exhibited better response. In fact, the best wound-coil transducer was more than an order of magnitude more effective than the best PCB-coil transducer tested in this initial experiment. Thus, while these results do not necessarily prove wound coils to be fundamentally advantageous over PCB coils, further MEAS development was pursued under the assumption that wound coils would be employed for excitation.

Table 1: Coil Type Experiment			
PCB Coils		Wound Coils	
Transducer	Received Amplitude ($\times 10^{-3}$)	Transducer	Received Amplitude ($\times 10^{-3}$)
A1	1.2	B4	4.4
A2	1.2	B8	3.0
A3	0.5	B9	7.1
A5	0.5	B10	14.1

2.1.1.2.2. Winding Style

Having thus determined to focus on wound coils for excitation, the first coil parameter studied was winding style, by which is meant the number of strands of wire which are wound onto the coil at once, or equivalently, the number of times that a unit of electrical charge will traverse the full radius of the coil in passing through the turns of the coil. For this experiment, transducers B3 and B4 were fabricated. The two transducers were identical double-layer transducers, save that B3 utilized a double-wound coil while B4 utilized a single-wound coil. The results of the experiment are shown in Table 2. The received amplitude of transducer B2 is also included in the table, for reference purposes; B2 was a single-wound coil similar to B4, but with only one layer and thus only half as many turns of wire. As can be seen in the table, adding a second layer of windings on a single-wound coil doubled the

efficiency of the MEAS as a transmitter, but switching to a double-wound coil reduced the efficiency by more than four times.

Table 2: Winding Style Experiment		
Transducer	Winding Style	Received Amplitude ($\times 10^{-3}$)
B2	Single-Layer, Single-Wound	2.2
B3	Double-Layer, Double-Wound	0.84
B4	Double-Layer, Single-Wound	4.4

This result seems to agree with theory. If coil thickness is doubled, the current density over a given point on the plate in the region of transduction increases, since the same current now flows over the point twice—once in each layer. Because the second layer is further from the plate, its effect is expected to be less, but if the layer thickness is small, the reduction may be only very slight. However, if the double-layer coil is double-wound instead of single-wound then the current in the second layer will flow in the opposite direction from the current in the first layer, and the result will be a net reduction in the magnitude of the eddy current induced in the plate. This explains the low signal strength observed for the double-wound coil. Thus, it may be concluded that for guided wave excitation using omnidirectional pancake-coil MEAS, a single-wound excitation coil is preferable.

2.1.1.2.3. Wire Specification

Another parameter in MEAS design is the wire specification used in winding coils. Wound coils are typically made with enamel-insulated magnet wire, but such wire is available in a wide variety of gages. In order to ascertain what gage of wire would perform best in MEAS applications, transducers B5, B6, and B7 were fabricated. All three transducers employed 3/4-inch-diameter single-layer single-wound pancake coils and identical disc magnets to provide the static magnetic field required for transduction. The coil for B5 was wound using AWG-30 magnet wire, while that for B6 was wound using AWG-26, and B7 was wound using AWG-22. The three transducers were tested using a previously described procedure and the results are shown in Table 3.

Table 3: Wire Diameter Experiment	
Transducer	Received Pulse Amplitude ($\times 10^{-3}$)
B5	2.8
B6	1.7
B7	1.0

The table seems to show an inverse correlation between wire diameter and transducer performance. It is not clear from the table how far this trend would continue as successively finer and finer wires were employed. It may be that there exists a certain wire diameter for which transmission efficiency is absolutely maximum, or it may be that efficiency continues to increase in the limit as wire diameter goes to zero and number of turns approaches infinity. However, mechanical considerations impose constraints on the wire sizes that can actually be employed in transducer fabrication. As a strand of wire is wound onto a coil, it is necessary to apply a certain tensile force to the wire in order to insure a coherent coil. Thus, the use of excessively fine wire tends to lead to frequent wire breakage. With the equipment used for R&D coil winding in this study, it seemed impractical to use any wire finer than AWG-30. Thus, it was concluded that for the purpose of this study, AWG-30 magnet wire appears to be the optimal wire specification for MEAS excitation coils.

2.1.1.2.4. Coil Thickness

Another factor in wound-coil MEAS design is the coil thickness, or number of layers incorporated into the coil. For coils of a given inner diameter, outer diameter, and wire specification, coil thickness also determines the total number of turns in the coil. As coil thickness increases, the current density for a

given magnitude of current flowing in the wire over the surface of the structure increases, and so the magnitude of the eddy currents induced in the structure should likewise increase. Thus, increasing the coil thickness should increase transducer efficiency, as was seen in the previous experiment. However, as coil thickness increases, the liftoff of the permanent magnet from the structure also increases. As the magnet is moved further from the structure, the intensity of its magnetic field in the region of transduction decreases. Thus, increasing coil thickness should reduce transducer efficiency. The existence of these opposing effects implies that there exists optimal coil thickness which will produce the maximum possible signal strength for a given magnet configuration.

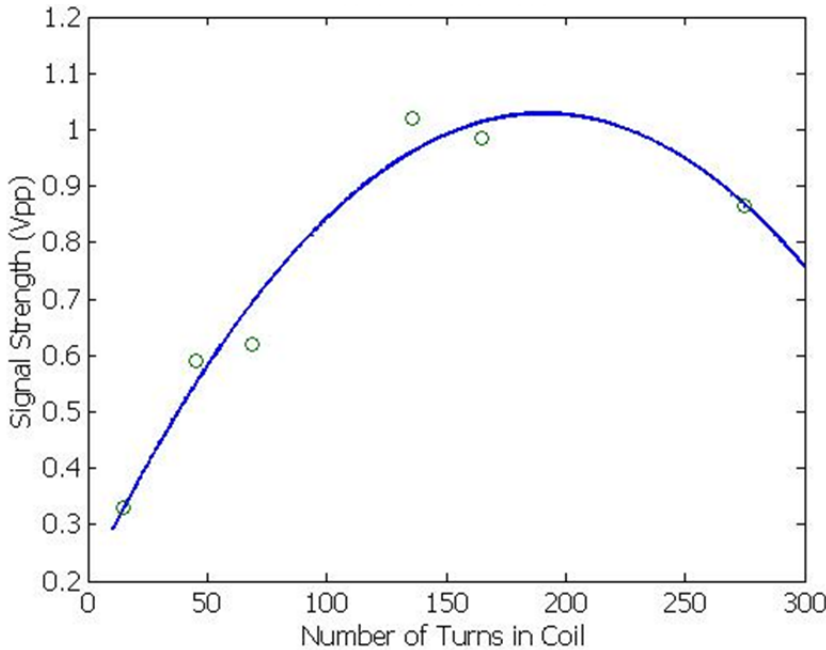


Figure 3 Plot of transducer signal strength as a function of number of turns in the coil.

In order to determine this optimal point, a number of transducers with different numbers of turns (as determined by coil thickness) were fabricated and tested. The experimental results are shown in Figure 3, along with a best-fit polynomial curve.

All of the transducers tested employed identical 3/4-inch (~19mm) diameter by 1/8-inch (~3.2mm) thick neodymium-iron-boron magnets of grade N52. Based upon Figure 3, it appears that maximum transducer efficiency for this magnet configuration on this type of transducer can be obtained with around 190 turns, corresponding to a coil with about 9 layers.

2.1.1.2.5. Magnet Configuration

Axially polarized neodymium-iron-boron disc magnets were employed as a means of providing the static magnetic bias field required for MEAS transduction. The strength and size of the magnet employed in a given transducer are design parameters that deserve consideration. These parameters are not independent, since the strength of such a magnet is proportional to its thickness and to degree of magnetization. It is to be expected that magnets of higher grade would produce more efficient MEAS, since, for a magnet of a given size, the higher the grade, the stronger the magnetic field. This prediction was verified experimentally.

Transducers B2, B6, and B8 are identical, save for the grade and thickness of their respective magnets. All are single-layer pancake coils with an outer diameter of about three quarters of an inch, with a three-quarter-inch-diameter disc magnet bonded to the top of the coil. However, the three transducers incorporated magnets of grade N40, N48, and N52, respectively, and the magnet of B6 was half as thick as the other two. The signal amplitude generated by these transducers was compared, and is presented in Table 4.

Table 4: Magnet Grade and Thickness			
Transducer	Magnet Grade	Magnet Thickness	Amplitude ($\times 10^{-3}$)
B2	N40	0.125"	2.2
B6	N48	0.0625"	1.7
B8	N52	0.125"	3.0

As can be seen in the table, the MEAS with the N52 magnet transmitted a substantially stronger pulse than the one with the N40 magnet. Reducing the thickness of the magnet reduced the transmission efficiency, but the reduction was partially compensated for by the increase in grade from N40 to N48. Thus, for maximum transmission amplitude, it is desirable to have both a high-grade magnet and a thick one. Yet for embeddable applications, the height of the transducer may be limited by other considerations; thus, it is also pertinent to note that a sufficient increase in grade can compensate for a reduction in thickness.

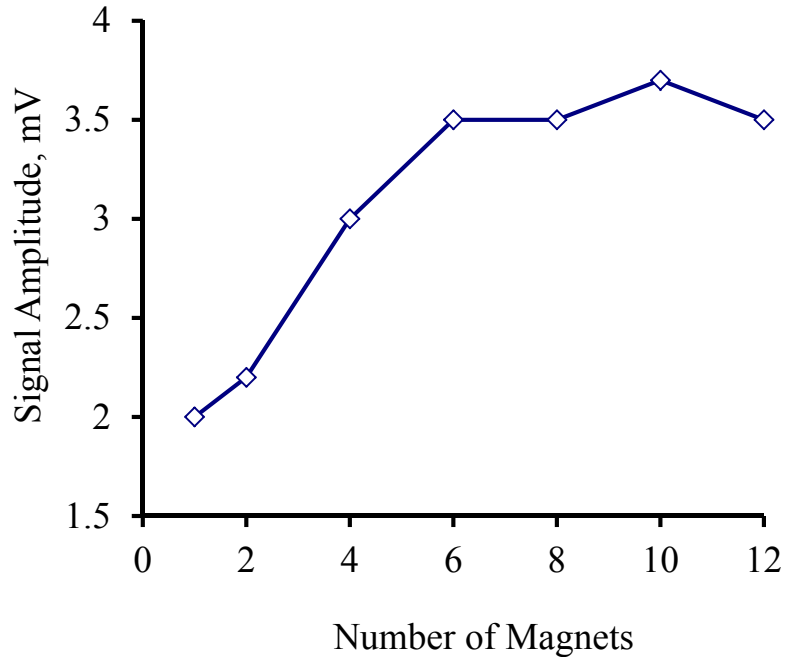


Figure 4 Plot of received signal amplitude vs. number of magnets on top of transducer B8.

To further explore the effect of magnet thickness, transducer B8 was used as a transmitter, and additional magnets identical to the N52 disc already mounted on it were stacked sequentially on top of the transducer, effectually increasing the magnet thickness. The amplitude of the pulse received by a piezoelectric transducer was then measured as a function of the number of magnets on the transducer, equivalent to the effective magnet thickness measured in eighths of an inch. The results are presented in in Figure 4. Based on Figure 4, it appears that signal strength increases almost linearly until the effective magnet thickness equals the magnet diameter, and then levels off for additional increase in thickness. This result agrees well with the conclusions of Maxfield *et al* (1976), who proposed that as a rule of thumb in EMAT design, the ratio of thickness to width should be close to unity.

2.1.1.2.6. Shielding

Incasing of a MEAS is desirable for a variety of reasons. If the housing is electrically conductive, it will enable shielding of the sensor signal from electromagnetic interference. In addition, it protects the MEAS from damage relating to wear or accidental impact. Finally, and perhaps most significantly, if the housing is ferromagnetic, its geometry will influence the distribution of the transducer's magnetic field, which could potentially improve the efficiency of the transducer. A metallic enclosure provides electromagnetic shielding and physical robustness. In order to ascertain what portions, if any, of the enclosure should be ferromagnetic, an experiment was performed. Experimental results have indicated

that the addition of ferromagnetic backing in any form increased transduction efficiency, but the largest increase was realized with the cup enclosure. Accordingly, a machined steel cup design was selected as shielding for initial MEAS prototypes, though lighter and more compact alternatives were sought later.

2.1.1.3. Frequency Response

Frequency response is one of the most important characteristics of a transducer. Therefore, studies were conducted to characterize MEAS transduction efficiency as a function of frequency. In the initial test setup, only start and end of the data acquisition was synchronized. MEAS was set up as a transmitter and PWAS was utilized as a receiver. Figure 5 shows the frequency response determined according to this procedure for a number of MEAS. It should be noted that a smoothing function was applied to the plotted FRF curves to reduce the level of apparent noise and thereby make overall trends more visible in the plots. However, instant drops in frequency responses are noticeable, which may be attributed to synchronization deficiencies.

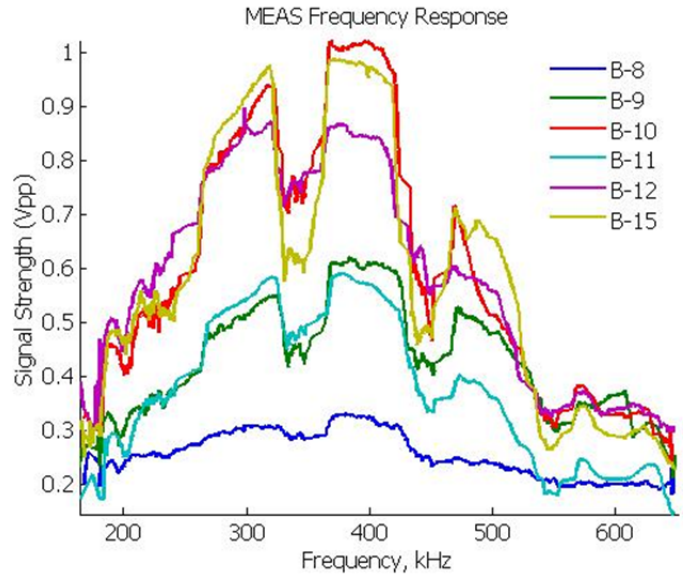


Figure 5 Plot of received amplitude versus frequency for a number of MEAS transducers

Figure 5 illustrates that different transducers have different efficiencies, but all seem to follow the same general pattern with regard to frequency response. It is apparent that while coil thickness and magnet specification may affect signal amplitude, they do not appreciably affect the frequency of maximum response. Additional experimental data (Zagrai et al., 2009) indicates that amplitude of the frequency response is substantially influenced by geometry (thickness in particular) and composition of the inspected structure. Figure 6 illustrates that peak response on the copper plate is obtained at a much lower frequency than the response on the aluminum plate. This result is due to the lower sound speed in copper in comparison to aluminum.

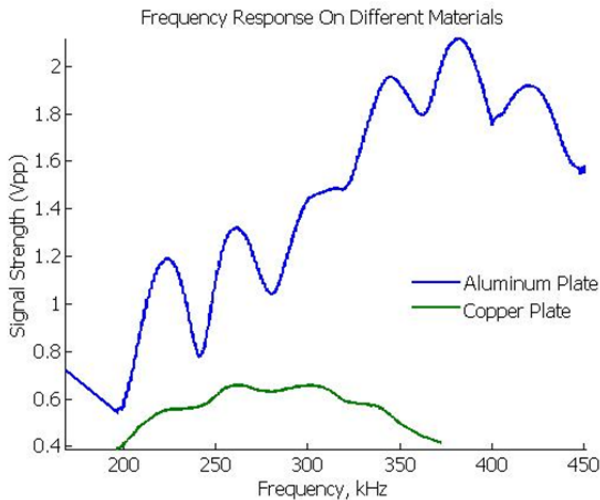


Figure 6 Comparison of MEAS FRF on aluminum and copper.

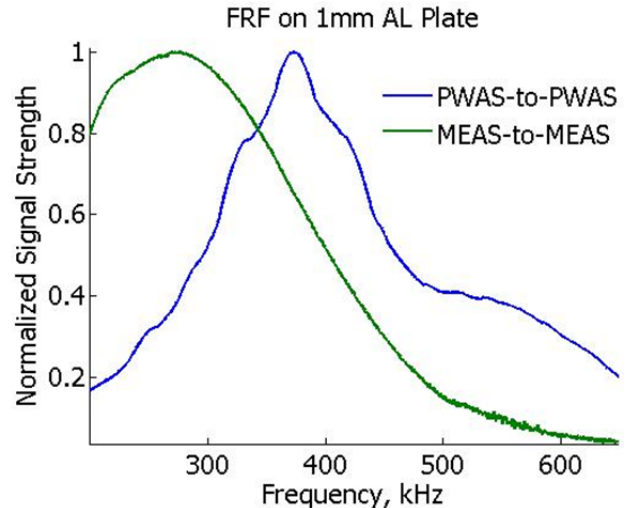


Figure 7 Comparison of the frequency response functions of PWAS and 0.75-inch diameter MEAS.

Later on in this study, LabVIEW-compatible device drivers were obtained for the RAM-5000 power supply, allowing a new algorithm for experimental determination of sensor frequency response functions to be created. MEAS efficiency was also improved to enable MEAS-to-MEAS transduction and frequency response measurement. Comparison of MEAS-to-MEAS and PWAS-to-PWAS frequency responses is presented in Figure 7. The peak amplitude of each FRF was normalized to unity to expedite comparison, as the absolute response of the PWAS is much higher than that of the MEAS. As it can be seen in the figure, PWAS response is less uniform and is confined to a narrower frequency band.

Studies were also conducted to confirm dependence of MEAS-to-MEAS frequency response peak position on structural material. Conclusions were similar to analysis followed from Figure 6.

2.1.1.4. Directivity

Directivity pattern of the pancake-coil MEAS was investigated by analyzing a signal transmitted from transducer C-1 to PWAS through a thin aluminum plate. In this experiment, a transducer C-1 was rotated in 15 degrees steps as illustrated in Figure 9. The result of the experiment is shown in Figure 8. As it could be seen in the figure, circumferential distribution of received signal amplitude is uniform and, therefore, the directivity of MEAS with pancake coil may be considered omnidirectional.

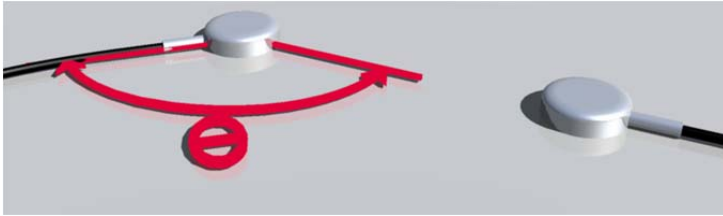


Figure 9 Experimental setup for directivity measurement.

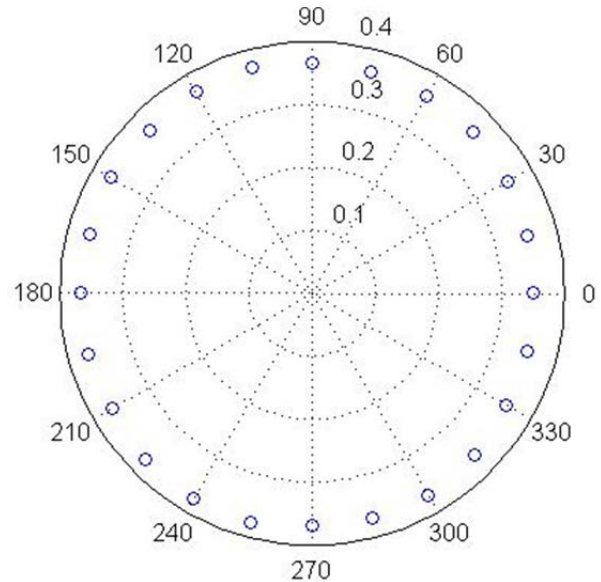


Figure 8 Directivity plot for transducer C-1.

2.1.1.5. Impedance Matching

Maximum signal strength demands maximum power transfer to the transducer. Maximum power transfer, in turn, is achieved through impedance matching. Several methods of impedance matching were investigated and their respective effectiveness was compared.

2.1.1.5.1. L-Matching Network Method

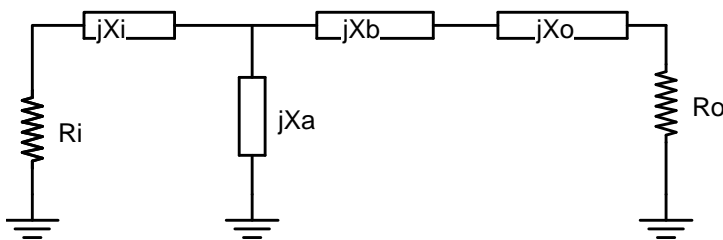


Figure 10 Impedance matching circuit recommended by RITEC.

The RITEC corporation recommends the “L-Matching Network” technique, which is described in detail by Gary Peterson (1995). In this method, two reactive elements are added to the driving circuit between the power supply and the transducer in order to improve impedance matching. One of these elements is placed in series with the transducer, while the other is placed in parallel. A schematic for this setup is shown in Figure 10.

In the figure, R_i and X_i represent the real and imaginary parts of the source impedance, respectively, while R_o and X_o likewise represent the real and imaginary parts of the load impedance, or in this case, the impedance of the transducer. X_a and X_b are the reactive loads added to the circuit. Considering the impedance of the gated amplifier output of the RAM-5000 is 50Ω (i.e. $R_i=50$, $X_i=0$), these parameters are determined as:

$$X_a = \frac{-50\Omega}{Q}, \quad X_b = QR_o - X_o, \quad \text{where } Q = \pm \sqrt{\frac{50\Omega}{R_o} - 1} \quad (1)$$

In order to calculate the values of the matching components, the impedance of the test transducers was measured using an HP 1492A Impedance Analyzer. The resulting plots of real and imaginary impedance are shown in Figure 11. The impedance plots were used to derive linear regression approximations of real and imaginary impedance for each of the four test transducers, and expressions above were used to calculate the required values of the matching circuit elements. An example of solutions for the matching circuit component values are shown in Table 5.

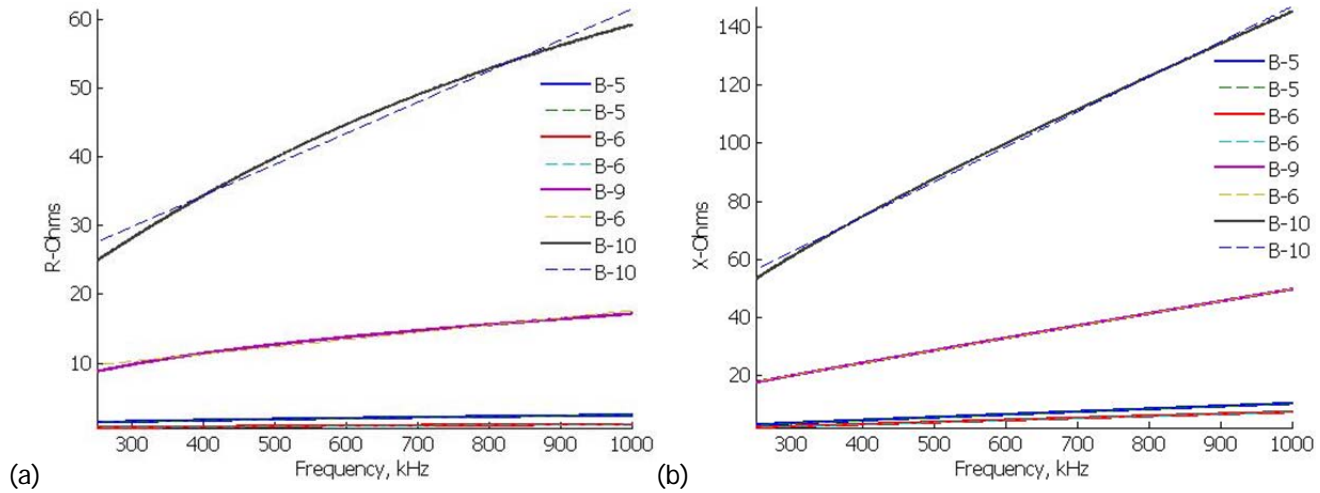


Figure 11 Real (a) and imaginary (b) parts of impedance for four MEAS. Solid curves show experimental data; dashed lines represent least-squares linear fit.

Table 5: Impedance Matching Solutions at 300 kHz								
Transducer			First Solution			Second Solution		
Model	R_0, Ω	X_0, Ω	Q	X_a, Ω	X_b, Ω	Q	X_a, Ω	X_b, Ω
B-5	1.5613	3.7014	5.57	-8.9766	4.9949	-5.57	8.9766	-12.398
B-6	0.68158	2.5368	8.5064	-5.8779	3.261	-8.5064	5.8779	-8.3346
B-9	10.295	20.107	1.9639	-25.459	0.11061	1.9639	25.459	-40.324
B-10	29.857	62.567	0.82137	-60.874	-38.043	0.8213	60.874	-87.09

It should be noted that the measured impedance of a MEAS is substantially lower when it is placed on a conductive surface (as it is when in use) than when it is remote from any conductive surface. Since the matching must be effected for a MEAS in use, the impedance was measured with the transducer lying on an aluminum plate. In principle, the thickness of the plate should affect the impedance. However, only a very slight change in impedance was observed between a transducer placed on a 1/16-inch-thick aluminum plate and the same transducer placed on a 1/2-inch-thick aluminum plate. Thus, in practice, the effect of plate thickness on transducer impedance can be considered negligible.

Common ceramic disc capacitors were utilized in an experiment to study the effect of impedance matching on MEAS transduction efficiency. Inductors in the values required for the matching circuits were not commercially available and were fabricated in house in accordance with RITEC recommendations. The recommendations suggested that the inductors must be wound with an air core (or equivalent), as ferrites will produce unwanted saturation effects. Fabrication procedure is described in details in Timothy Barnes MS thesis (2010). Illustrations of the matching circuitry are depicted in Figure 12 and Figure 13.

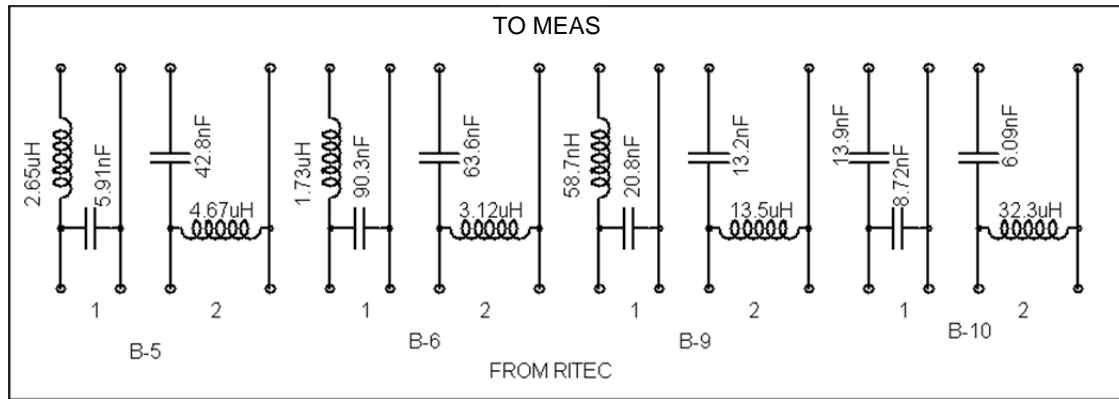


Figure 12 Schematic of matching circuits.

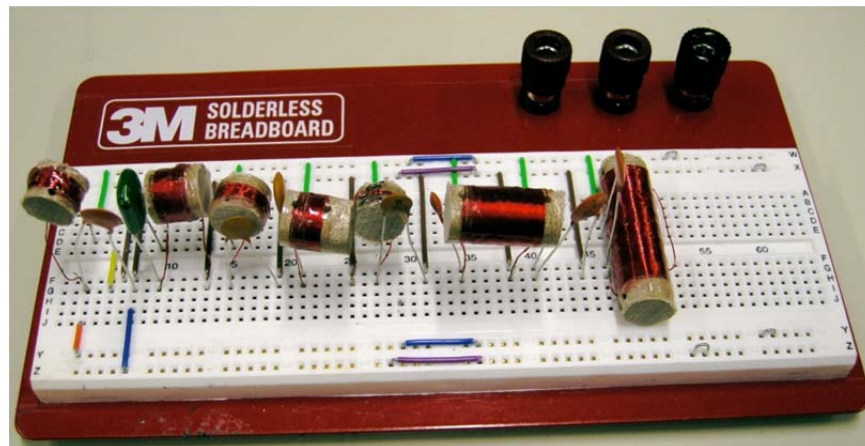


Figure 13 Photograph of actual test circuit.

The frequency response of each of the selected transducers was recorded for cases in which the transducer was alternately driven directly and through each of its two respective matching circuits. Examples of MEAS response are shown in Figure 14.

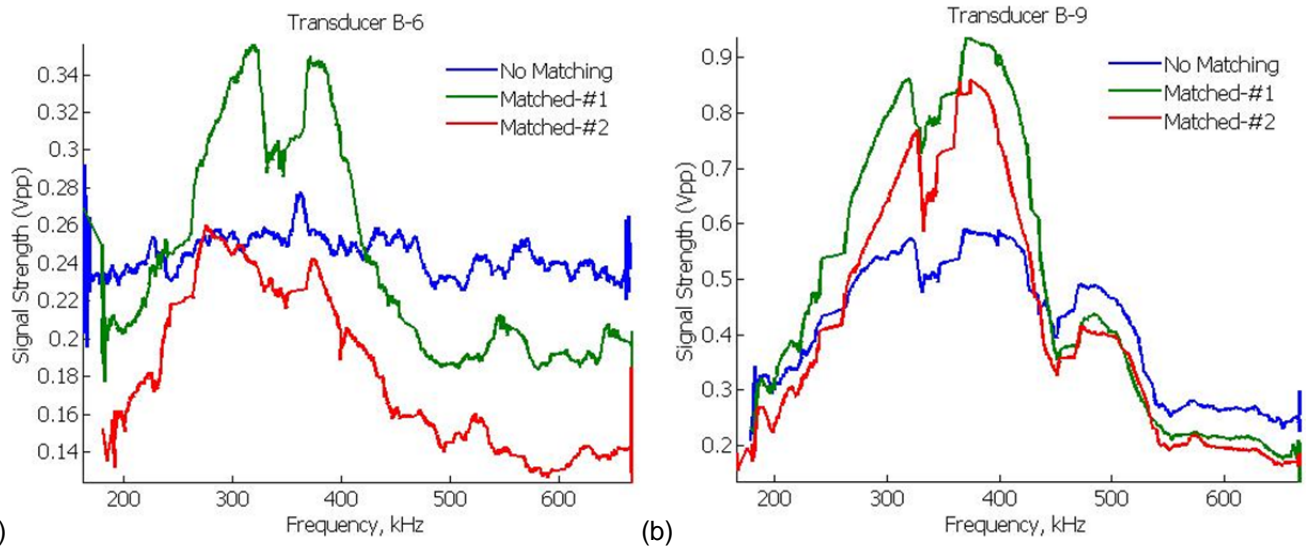


Figure 14 Frequency response for transducer B-6 (a) and B-9 (b), with and without L-matching.

As can be seen in the figure, the effect of impedance matching upon received amplitude varies, possibly due to approximations that were made in creating the matching circuits. Transducer B-9 provides a good example of the expected response to impedance matching: use of either matching circuit affords a substantial increase in amplitude, accompanied by a slight change in the shape of the frequency response curve, characterized in this case by a shift of the central peak toward lower frequencies. It should be emphasized that while L-matching may be capable of securing substantial increases in transducer efficiency, the matching must be very precise. If components are only available for an approximation of the required matching circuit, the value of this technique may be questionable.

2.1.1.5.2. Transformer Method

An alternative to L-matching networks is transformer matching. RITEC provides the following equation for calculating the voltage step-up ratio of a transducer driving circuit:

$$\frac{E_{transducer}}{E_{Out}} = \frac{|Z_o|}{\sqrt{50 * R_o}} \quad (2)$$

Using this equation, voltage step-up ratios were calculated for the transducers employed in the L-matching network experiment at three different frequencies. The calculated ratios are shown in Table 6. It may be observed that at 400 kHz, the step-up ratio for B-5 should be about 0.5 (or 1:2), while that for B-10 should be about 2.0 (or 2:1). Thus, it would be predicted that transduction efficiency for B-5 could be improved using a 1:2 step-down transformer, while efficiency for B-10 could be improved using a 2:1 step-up transformer.

Table 6: Voltage Step-Up Ratios for MEAS			
Frequency (kHz)	300	400	500
B5	0.45	0.54	0.62
B6	0.45	0.55	0.63
B9	1.00	1.13	1.25
B10	1.79	1.98	2.15

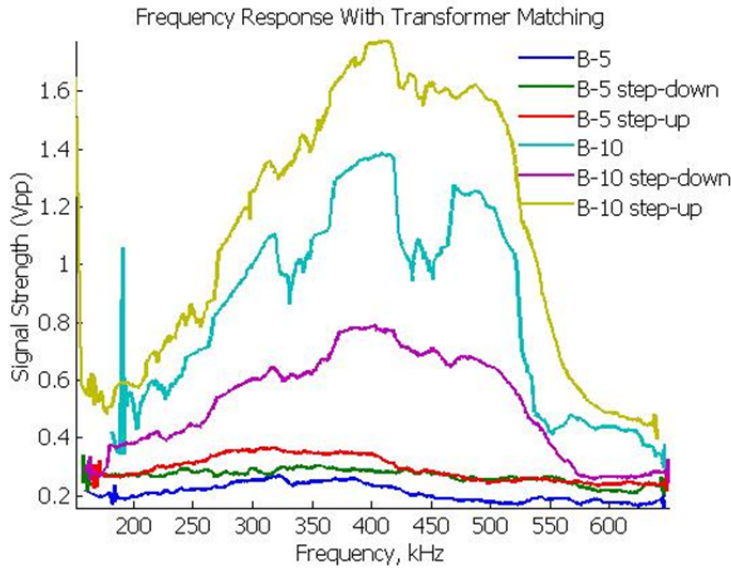


Figure 15 Frequency response of transducers B-5 and B-10 with transformer matching.

Figure 15.

Interestingly enough, the response of B5 was increased by the addition of any transformer—either step-up or step-down. Yet contrary to expectation, the step-up transformer produced the larger increase in transduction efficiency. The response of B-10 was significantly increased by the addition of the step-up transformer, and significantly reduced by the addition of a step-down transformer, in agreement with expectation.

2.1.1.5.3. Balanced Transducer Method

The impedance matching methods considered in heretofore make the implicit assumption that the transducer itself cannot be changed. That is, the methods attempt to improve impedance matching between an arbitrary specified power supply and a transducer of known but arbitrary impedance. However, if transducers are being fabricated in-house, as they were, it is expedient to inquire whether the transducer itself can be designed to match the known impedance of the power supply with which it will be used.

The impedance of an omnidirectional MEAS consists of a real part arising from the resistance of the excitation coil and an imaginary part arising primarily from the inductance of the coil. The internal impedance of the RITEC RAM-5000 is known to be 50 Ω resistive, and so for maximum power transfer, it is desirable to make the impedance of the MEAS 50 Ω resistive as well. The impedance of a series combination of electrical components is equal to the sum of their individual impedances, so at a given frequency, it should be possible to cancel out the imaginary part of MEAS impedance by connecting the coil in series with a capacitor of appropriate size. The real part of impedance, i.e. the resistance, of the coil is simply a function of the length and diameter of the wire from which the coil is wound and the resistivity of the wire, according to the equation

$$R = \frac{4\rho\ell}{\pi d^2}, \quad (3)$$

where R is resistance, ρ is resistivity, ℓ is total wire length, and d is wire diameter. If the coil is assumed to be a stack of perfect spirals of known inside and outside diameter, ℓ can be estimated from

To test this prediction, transducers B5 and B10 were alternately driven with no matching, with a 1:2 step-down transformer, and with a 2:1 step-up transformer. The frequency response functions the two transducers were measured and compared. It should be noted that when driving a transformer (either step-up or step-down) with the RAM-5000 directly, the transformer introduced severe nonlinearities into the signal. Thus, to preserve the waveform, it was necessary to drive the transformer through a 50-Ohm resistive load-balancing circuit provided by RITEC. In this experiment, the resistive circuit was also employed when driving the transducer without an intervening transformer. The resulting frequency plots are shown in

the overall dimensions of the coil. Assuming the resistivity of copper wire to be $6.77 \times 10^{-7} \Omega\text{-in}$, it is possible to derive the following relation:

$$R = \frac{t}{d^4} (53.9D_o^2 + 569.4D_oD_i - 623.3D_i^2) \times 10^{-9} \quad (4)$$

where R is coil resistance in ohms, t is coil thickness in inches, D_o is coil outside diameter in inches, D_i is coil inside diameter in inches, and d is wire diameter in inches. Solving this formula for t , it is possible to calculate how thick a coil of given size and wire gage would have to be in order to have a resistance of 50Ω . For a coil of inner diameter 0.250" and outer diameter 0.750" (similar to most of the B and C series transducers made for this study) and wire of AWG 32, the coil thickness would be 2.036 in. Upon consideration of the formula above, a 0.050"-thick pancake coil was wound from AWG-40 magnet wire, and a shielded MEAS was fabricated using the coil. The resulting transducer was labeled C3. Using a PWAS as a receiver, the FRF of this transducer was recorded, and is shown in Figure 16a. The FRF was then divided by the previously-determined FRF of the PWAS, to obtain the FRF of C3 itself, shown in Figure 16b.

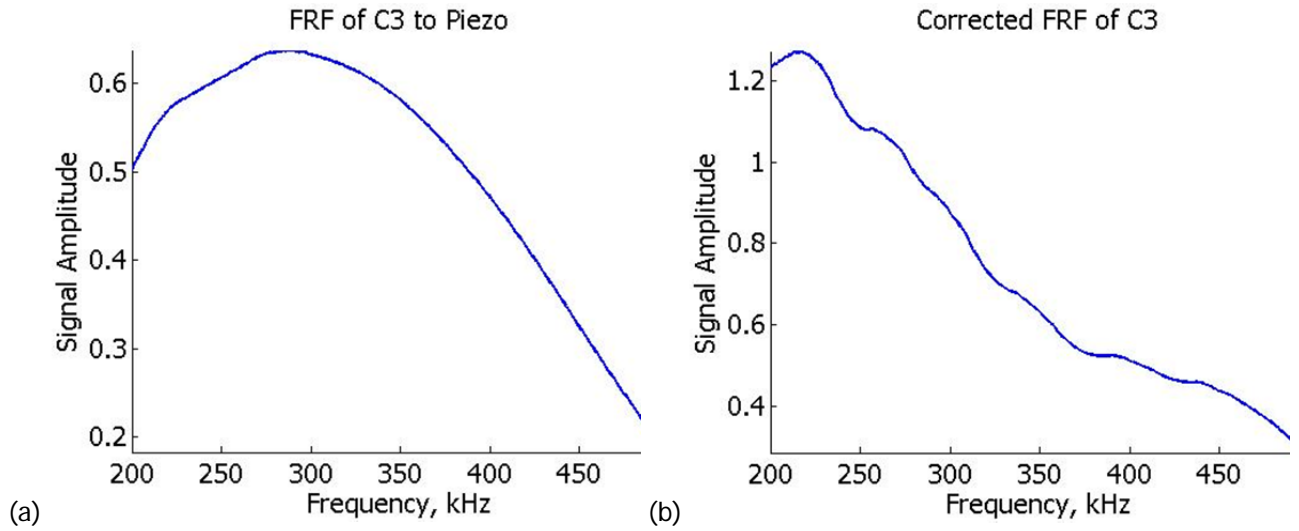


Figure 16 (a) Received signal amplitude transmitted from C3 and received with a PWAS. (b) FRF of C3, corrected for frequency response of PWAS.

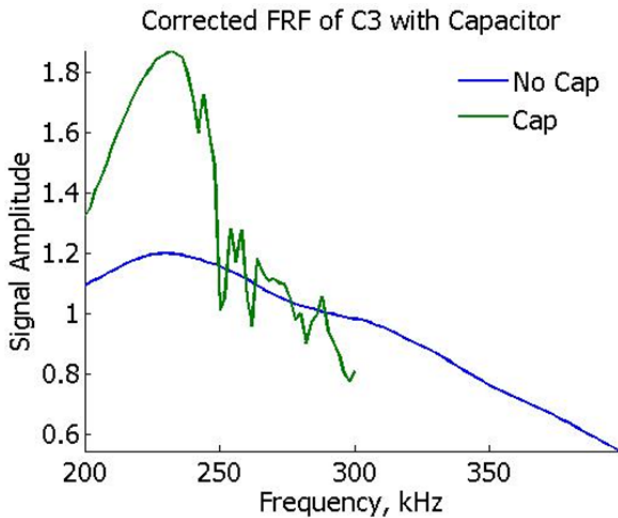


Figure 17 Comparison of FRFs of transducer C3 with and without an impedance-balancing capacitor.

Integration of the capacitors into the circuit driving the MEAS was considered. The frequency response function of C3 with the attached capacitor was recorded, receiving with the same PWAS, and corrected for the PWAS response as before. Comparative plots of transducer FRF for C3 with and without the attached capacitor are shown in Figure 17. Clearly, the addition of the capacitance increases signal strength, but reduces bandwidth, as would be predicted. Moreover, with capacitive impedance balancing, the transmitted signal appeared to become unstable above about 240 kHz.

Several more transducers were fabricated using AWG #30 coils with varying numbers of turns. Each transducer was connected in series with a capacitive element so as to cancel its imaginary impedance at a frequency of 250 kHz, and the FRF

of each transducer was measured. MEAS C2 was used as a receiver. Since C2 had comparable frequency response to the experimental transducers, no FRF correction such as had been used when receiving with a PWAS was required. The resulting response functions are shown in Figure 18. The FRFs of C1 with and without capacitive circuit balancing are included for reference.

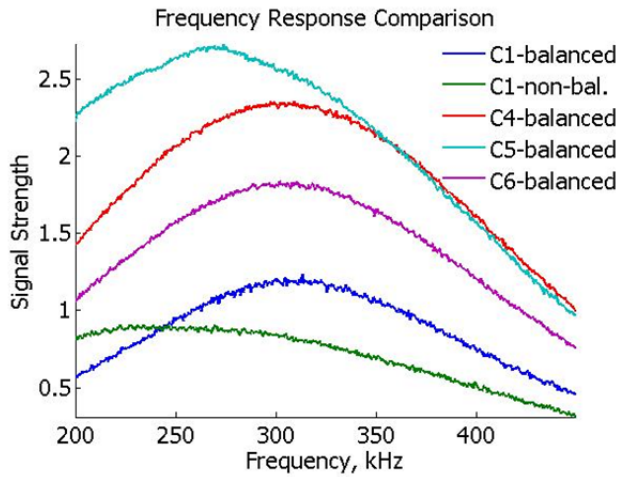


Figure 18 FRF of various transducers with capacitive impedance matching.

sinusoidal tone burst, it was necessary to drive the transducer through the 50- Ω load supplied with the system by RITEC. This, in effect, connects a 50- Ω resistor in parallel with the transducer, and thereby alters the effective transducer impedance. With the load in place, the lower the impedance of the transducer, the greater the electrical current that will flow through its coil.

In the first series of experiments addressing transducer efficiency, it was observed that with current held constant, as coil thickness increases effective current density over the work piece increases, increasing transduction efficiency, while magnet liftoff also increases, reducing transduction efficiency. Now, however, it is observed that coil thickness also affects transducer impedance, which in turn affects the amount of current that flows through the coil. For a given wire diameter, the thicker the coil, the higher its impedance, and thus the lower the current that will flow through it for a given power supply setting. It may be that when no impedance matching is attempted, the transducer impedance is high enough that small changes in coil thickness do not appreciably affect current, and thus, the two effects noted earlier dominate transducer response as a function of coil thickness. However, when impedance matching is affected as above, the current (or rather the impedance, which for a given excitation voltage determines the current) becomes the dominant factor affecting transduction efficiency. This would explain why, in the absence of capacitive impedance matching, a 9-layer coil produces optimal transduction efficiency, while with the addition of capacitive matching, a 2-layer coil is optimal.

2.1.1.5.4. Receiver Matching

The goal of impedance matching in general is to improve energy transmission efficiency. Thus, impedance matching efforts pertaining to EMATs and MEAS usually focus on matching of the transmitter to the power supply. However, it is also important to achieve impedance matching on the receiving end. Using C-8 with impedance matching as a transmitter, a variety of transducers were utilized as alternative receivers, and their FRFs were recorded. As a reference, C2 was included without matching (transducers C1 and C2 are identical). The resulting FRFs are shown in Figure 19, while the measured impedance of the transducers is given in Table 7.

Two unanticipated trends become apparent in Figure 18. First, whereas it was expected that the highest response would be obtained with transducers whose impedance most nearly matched the power-supply impedance of 50 Ω , it is observed that as transducer impedance decreases, response increases, even for impedances below 50 Ω . Second, whereas all the transducers were balanced to exhibit strictly real impedances at 250 kHz, all the balanced transducers except C5 exhibit peak responses above 300 kHz.

The unexpectedly high efficiency of transducers with impedances less than 50 Ω is likely explained by the presence of the resistive load in the power transmission system. With all the transducers tested, it was found that in order to obtain a reasonably

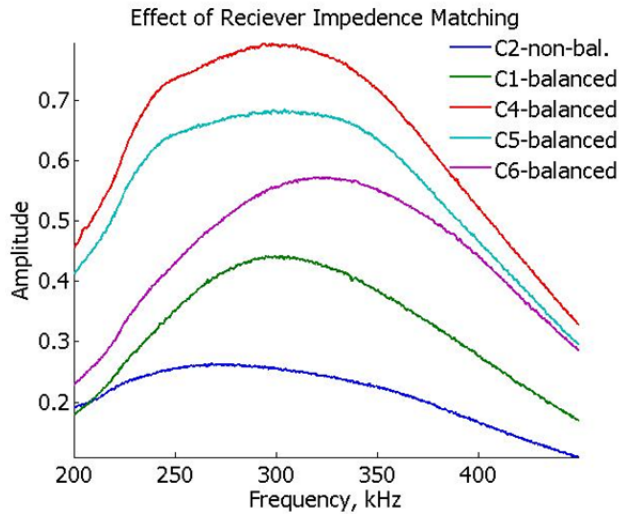


Figure 19 Comparison of signal FRF with various impedance-matched receivers.

Table 7: Impedance of Transducers from Figure 19	
Transducer	Impedance measured at 250 kHz
C1—Balanced	107 Ω
C2—Non-Balanced	340 Ω (@ 70 deg)
C4—Balanced	45 Ω
C5—Balanced	12.8 Ω
C6—Balanced	57 Ω

It is observed from Figure 19 that receiver matching does, in fact, significantly improve received signal amplitude. In this case, the receiving instrument was a National Instruments PXI-5142 digitizer.

The digitizer can be operated in one of two internal impedance modes: 100 M Ω resistive or 50 Ω resistive. For the purpose of SHM experiments with MEAS, it was always operated in the 50 Ω mode. Since this is the same nominal impedance as the Ritec RAM-5000 power supply, it makes sense that similar sensors would tend to provide the best matching for each, and this is exactly what is observed. In both transmitter and receiver matching experiments, transducers C4 and C5 with capacitive matching provide the best available signal strength. In reception, C4 seems to offer a slight advantage, while C5 offers a slight edge in transmission, at least at lower frequencies. Nevertheless, the fact that optimal transducers for both transmission and reception end up being of very similar design is an important conclusion, and simplifies the MEAS design process considerably, as it makes it reasonable to assume that for all practical purposes, a transducer optimized for reception is also optimized for transmission, and vice versa.

2.1.2 MEAS Miniaturization

Current designs of electromagnetic acoustic transducers (EMAT) are far from compact. To facilitate embeddability, the design must be adjusted to facilitate SHM applications. As it was mentioned earlier, transducers developed with optimization strategies for embeddability are termed magneto-elastic active sensors (MEAS) by analogy to piezoelectric active sensors (PWAS). Having investigated the design of pancake-coil MEAS transducers for maximum signal strength, it is now of interest to determine how compact a sensor of this type can be made and still produce an acceptable operational characteristics.

2.1.2.1 Coils Fabrication

Pancake-type excitation coils for miniaturized MEAS were wound in the same manner as those produced earlier in the study, though to accommodate the winding of coils of smaller diameter, a smaller mandrel was designed and fabricated. However, a coil of the same wire with smaller outer diameter and the same thickness will have smaller real impedance, and it is desirable to hold the real impedance at the optimal levels. The impedance can be increased by adding layers to the coil, but when minimum size is required, thick coils are not desirable. Thus, for very small coils, it may be necessary to trade off real impedance matching against coil thickness in order to achieve an optimal compromise between sensor size and sensor performance. By trial and error, it was determined that for sensors on the order of half an inch in outer diameter, a three-layer coil provides a good balance between the two, and thus, three-layer coils were employed in all the miniaturized MEAS.

2.1.2.2. Connectivity

Impedance matching procedures implicitly assumed that cable impedance was negligible, as cables connecting the transducers to the power supply were relatively short (<1 m). However, at the frequencies typically used for ultrasonic diagnosis, this is not necessarily the case, and so it is desirable that the cable to be used with the transducer be included in the driving circuit when the transducer impedance is first balanced. It is also desirable to minimize the amount of noise, interference, and distortion that can be caused by the presence of the capacitive element, with its un-shielded wires and temporary alligator-clip connections.

Therefore, instead of letting the transducer, the matching circuit, and the cable be separate circuit elements assembled only at the time of transduction, these three were integrated into one in the miniaturized MEAS design. A piece of 0.81mm OD coaxial cable was soldered to the excitation coil on one end, and to the capacitive matching circuit and an appropriate connector at the other end. This resulted in a one-piece cable-transducer assembly with built-in impedance matching, thus ensuring good connections to the matching circuit and taking account for cable impedance in the balancing process.

2.1.2.3. Shielding

It has been shown that ferromagnetic shielding enhances MEAS performance by reducing electromagnetic interference and concentrating the static bias field in the region of transduction. To capitalize on these benefits, the large C-series transducers fabricated earlier in this study were designed with a machined steel cup enclosing the excitation coil and magnet assembly. While the steel cup was a highly effective means of providing ferromagnetic shielding, and had the added benefit of making the C-series transducers very structurally robust, it was also substantially increased the size and weight of the transducer. Thus, when MEAS miniaturization was undertaken, alternative shielding methods were sought.

To obviate the need for a machined shield, Magnetshield foil was employed. Magnetshield is a ferromagnetic alloy with a magnetic permeability roughly ten times that of ordinary steel and very high magnetic saturation point. It is available in thin sheet stock online (www.lessemf.com). Measuring 0.010 inches in thickness, this sheet stock was roughly a tenth as thick as the machined steel enclosures of the C-series transducers. Since the permeability is about ten times higher, however, it should provide roughly comparable magnetic shielding. Therefore, upon fabrication, the miniaturized MEAS transducers were clad with Magnetshield foil.

2.1.2.4. Miniaturization Results

A miniaturized MEAS typical of those fabricated in this study is shown in Figure 20. Sensors of this design were fabricated with varying coil diameters and magnet thicknesses. Transducers E1 and E2 incorporated half-inch-diameter coils with eighth-inch thick magnets, while E3 similarly employed a half-inch coil, but with a magnet only one sixteenth of an inch thick. Transducers E5 and E6 employed coils whose outer diameter was only three eighths of an inch, with a magnet only one thirty-second of an inch thick. As mentioned heretofore, each coil was three layers thick and wound from AWG #30 magnet wire, which made it about one thirty-second of an inch thick. Figure 21 provides a comparison of the overall size of these transducers to each other and to C1.

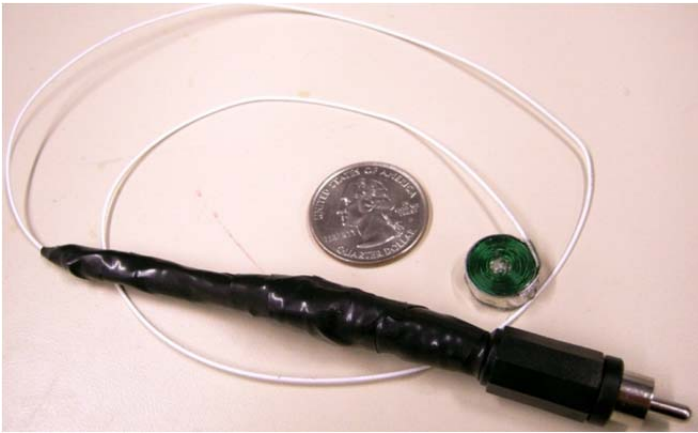


Figure 20 Typical miniaturized MEAS.

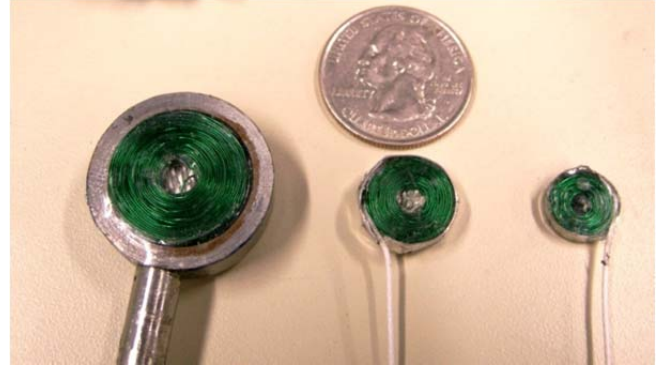


Figure 21 Comparison of transducer size. From left to right: C1, E2, E5.

To compare the relative efficiencies of these transducer designs, a PWAS was employed as a standard receiver, and the frequency response of each MEAS was recorded in turn. The resulting frequency response curves are plotted in Figure 22. Because the curves represent the product of the transmitting MEAS FRF and the receiving PWAS FRF, and because the response of the PWAS is not flat over this frequency range they do not necessarily represent the absolute FRF of these MEAS. However, since the receiver was the same in all cases, they do provide a means of comparison among the MEAS.

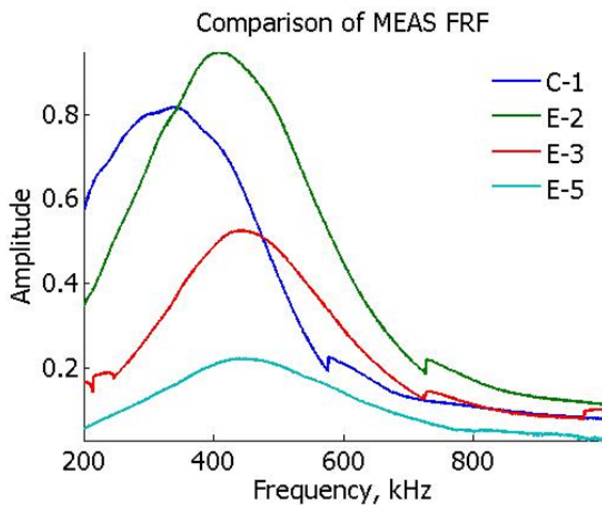


Figure 22 Comparison of MEAS FRFs as measured by a PWAS receiver.

As can be seen in the plot, the miniaturized transducers tend to exhibit a peak response at higher frequencies than C1. Due to their smaller diameter, this is precisely what would be expected. More surprising, however, is the fact that E2 exhibits a higher peak response than C1. C1 and E2 incorporate magnets of the same grade and thickness, so this would tend to indicate that the integrated impedance matching and alternate shielding material of E2 more than compensated for any loss of efficiency associated with the reduction in size. Further size reduction within the E-series comes at a price in terms of signal strength, as the plot clearly illustrates. E3 is the same diameter as E2, but has a magnet only half as thick, and appears to be roughly half as powerful in transmission. E5, in addition to being smaller in diameter than E3, incorporates a magnet half as thick,

and exhibits a peak response roughly half that of E3. Therefore, there appears to be a roughly-linear decrease in transduction efficiency with decreasing magnet thickness. All the magnets used in these transducers were the same type and grade; namely - neodymium-iron-boron N52.

For miniaturized sensors, MEAS-to-MEAS transmission was verified in a separate experiment. E1 was used as a transmitter and E2 as a receiver, and several signals were recorded at different frequencies as illustrated in Figure 23. At 300 and 500 kHz, these half-inch transducers produce a clear signal with a high signal-to-noise ratio. However, as frequency is increased to 1200 kHz, it has practically receded into the noise, though the arrival of the initial pulse is still visible as a pair of peaks in the plot. It should also be noted that for all practical purposes, these sensors generate only the S_0 wave mode. Any contribution of the A_0 mode is below the noise threshold of the measurements.

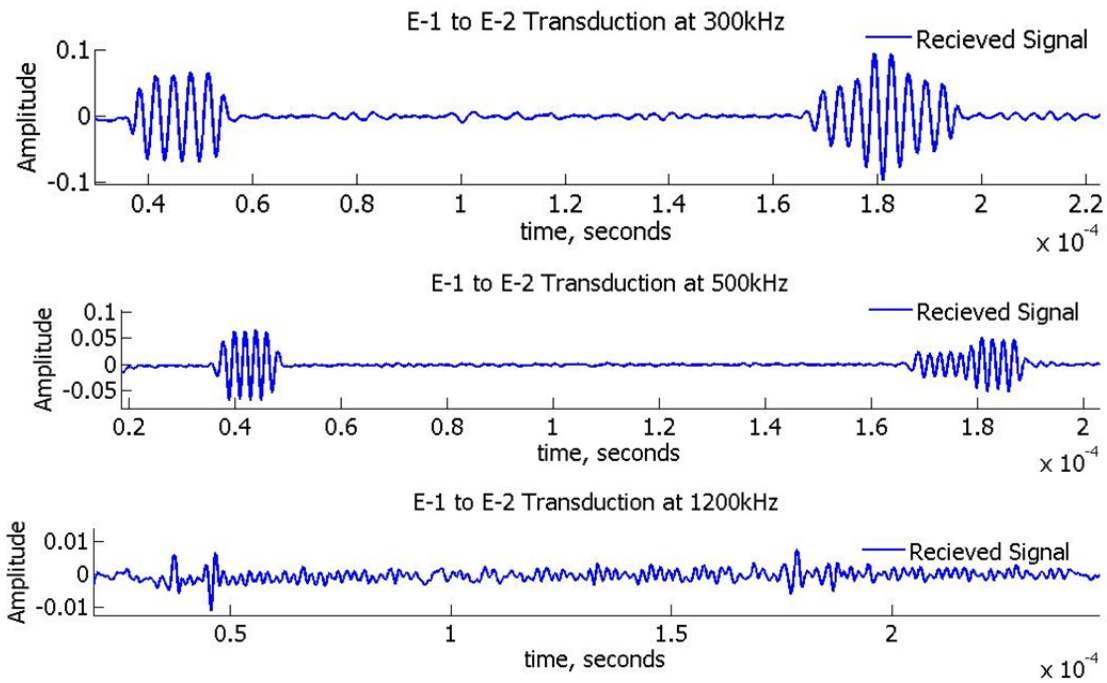


Figure 23 Miniature MEAS signal at various frequencies.

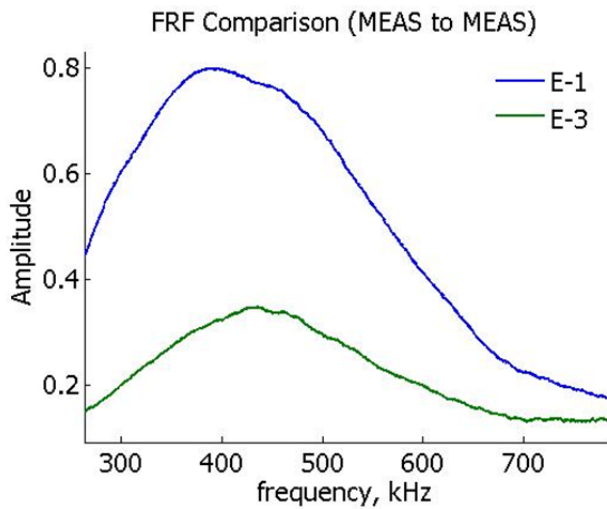


Figure 24 Frequency response of E1 and E3, receiving with E2.

magnets thinner than one thirty-second of an inch. Thus, E5 and E6 were made to these minimum-size specifications. Signals were then transmitted between these two sensors on a thin aluminum plate, and recorded with various levels of averaging. The same was done using sensors E1 and E2 for comparison. The results are shown in Figure 25 and Figure 26.

As a further demonstration of MEAS-to-MEAS transmission using the smaller sensors, E2 was used as a receiver and frequency response functions were recorded for both E1 and E3. The resulting curves are plotted in Figure 24. They seem to show much the same trend as observed in Figure 22, indicating that the response of the PWAS may be similar enough to the response of E2 that the distortion in Figure 22 was not significant.

Finally, it is desirable to know just how small MEAS can be made while retaining a usable signal level. Using the sensor design and fabrication practices employed in this study, it was deemed impractical to fabricate sensors with coils smaller than three eighths of an inch OD, or with

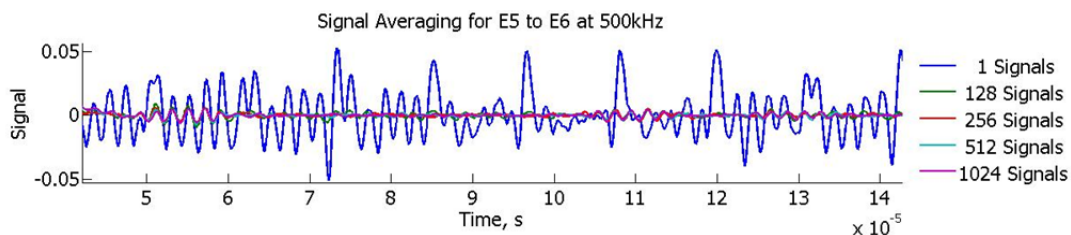


Figure 25 Signal transmitted and received with E5 and E6 for various levels of signal averaging.

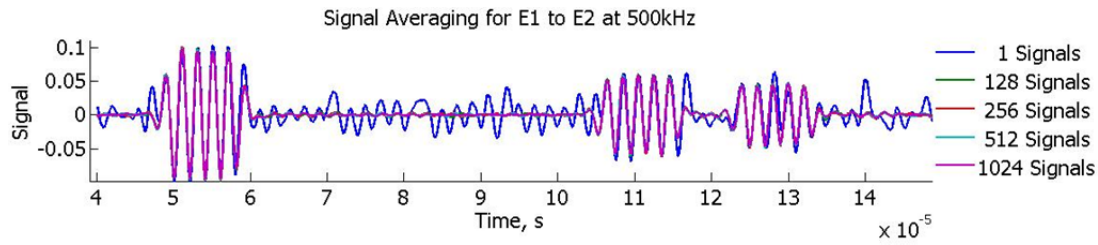


Figure 26 Signal transmitted and received with E1 and E2 for various levels of signal averaging.

For the smallest transducers, E5 and E6, the signal is completely obscured by noise when only a single record is considered. Taking the average of 128 signals, the initial pulse becomes marginally visible. Averaging 256 signals, the first echo starts to materialize, and by averaging 1024 signals, a relatively clear signal may be obtained, though some noise is still evident. In contrast, when using the slightly larger but still highly compact transducers E1 and E2, the initial pulse and the first two echoes are clearly visible for a single record. Averaging 128 signals does significantly improve the signal to noise ratio. As the number of averaged signals is increased from 128 to 1024, little change in the signal is observed.

The research efforts have demonstrated that it is possible to fabricate highly compact MEAS capable of producing usable signals. Sensors on the order of half an inch in diameter by three sixteenths of an inch thick have been produced which are readily capable of transmitting and receiving elastic-wave signals on thin aluminum plates in pitch-catch mode. Transmission and reception has also been demonstrated with smaller sensors, down to about three eighths of an inch in diameter by a little over a sixteenth of an inch thick. However, signal strength is observed to fall off rapidly with decreasing magnet thickness, and at this point, these smallest transducers can only be used with extensive signal averaging. In the future, advancements in permanent magnet technology may make the use of even smaller MEAS practical. At this point, however, the half-inch transducer design embodied in E1 and E2 was chosen as the primary workhorse for demonstration of embeddable MEAS-based SHM.

2.1.3 Shear-Wave MEAS

Shear waves have found many applications in conventional NDE. The SH_0 mode is non-dispersive, which is advantageous for many damage detection methodologies. Hence, shear-wave MEAS were considered for SHM applications.

2.1.3.1. Design and Fabrication

There are a variety of designs that can be used to excite and detect SH waves. One of the popular designs considers a masked racetrack coil with a periodic permanent magnet (PPM) array affixed to the side of the coil remote from the host structure, as illustrated in Figure 27. When a time-varying excitation current is passed through the coil, the Lorentz force under the straight portions of the racetrack will be predominantly in the plane of the host structure, and oppositely directed under opposite magnetic poles. Thus, a shear wave with wavelength equal to the magnet period should be generated in the host structure. The mask serves to isolate the host structure from currents flowing in the rounded ends of the coil.

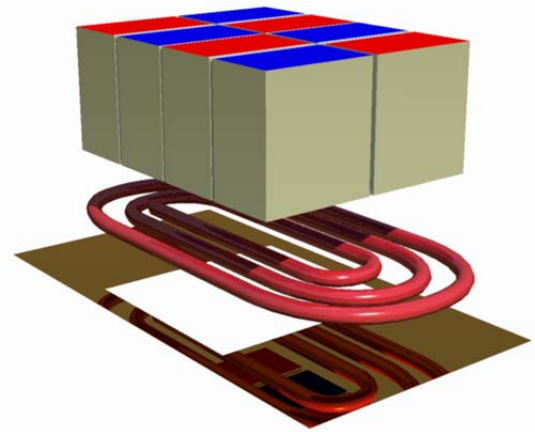


Figure 27 Exploded view of racetrack coil MEAS for SH-wave excitation, showing periodic permanent magnet array (PPM), coil, and copper mask.

In order to implement this design, racetrack coils had to be fabricated. This was accomplished using a wire-winding technique very similar to that employed for winding pancake coils, save that a double-post mandrel was used. Where necessary, the foil was soldered to ensure that it remained in place. The magnet array was affixed to the back of the coil using fiberglass adhesive tape. In some cases, ferromagnetic backing plates with grooves milled out for the magnets were attached to the back of the magnet array, to ensure that it was maintained in the correct orientation and configuration. Photographs of two racetrack-coil transducers fabricated for this study are shown in Figure 28.

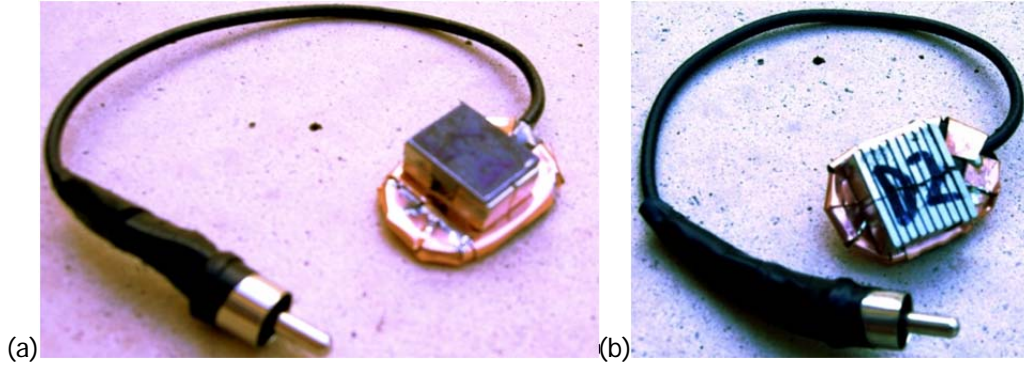


Figure 28 Photographs of transducers D5 (a) and D2 (b), consisting of a masked racetrack coil and PPM array with a half-period of $1/4$ and $1/32$ of an inch respectively.

It is anticipated that the racetrack-coil transducers described above produce a highly directional radiation pattern. However, for many SHM applications, omnidirectional transduction is desirable. Thus, it is natural to inquire whether an omnidirectional SH-wave MEAS can be fabricated. No designs for omnidirectional shear-wave EMATs were found during the literature survey. Wilcox (2005) shows excitation force distribution that would be required to produce an omnidirectional SH-wave, but makes no comment about how such a distribution might be realized, and chooses to use an omnidirectional Lamb-wave EMAT for the research presented in the paper. To produce omnidirectional SH waves, a transducer would essentially need to apply a periodically reversing torque to the material of the host structure at the point of transmission. If the transducer is to be a MEAS, this implies that it must generate a Lorentz-force distribution that is everywhere tangential to the circumference of the transducer. In principle, it should be possible to realize this Lorentz-force distribution by means of an axially polarized disc magnet and an excitation coil that induces a uniform outward radiation of current in the host structure, as illustrated in Figure 29. It was suggested that a toroidal excitation coil, such as that shown in Figure 30 might produce the desired flow of induced current.

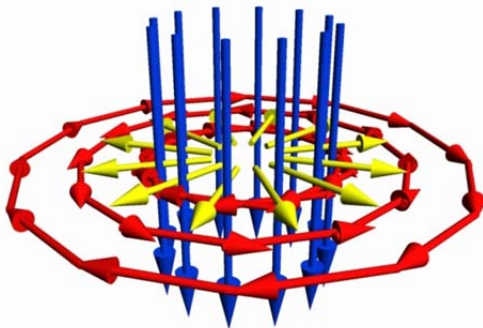


Figure 29 Transduction pattern required for omnidirectional SH MEAS. Blue arrows show magnetic field, yellow arrows show induced eddy currents, red arrows show Lorentz force direction and resulting lattice displacement.

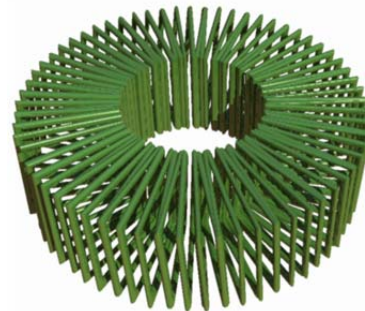


Figure 30 Toroidal excitation coil.

A flattened toroidal coil was fabricated by winding magnet wire manually around a steel washer. This coil was then incorporated into a transducer in much the same way as a pancake coil. A photograph of the resulting prototype is shown in Figure 31.

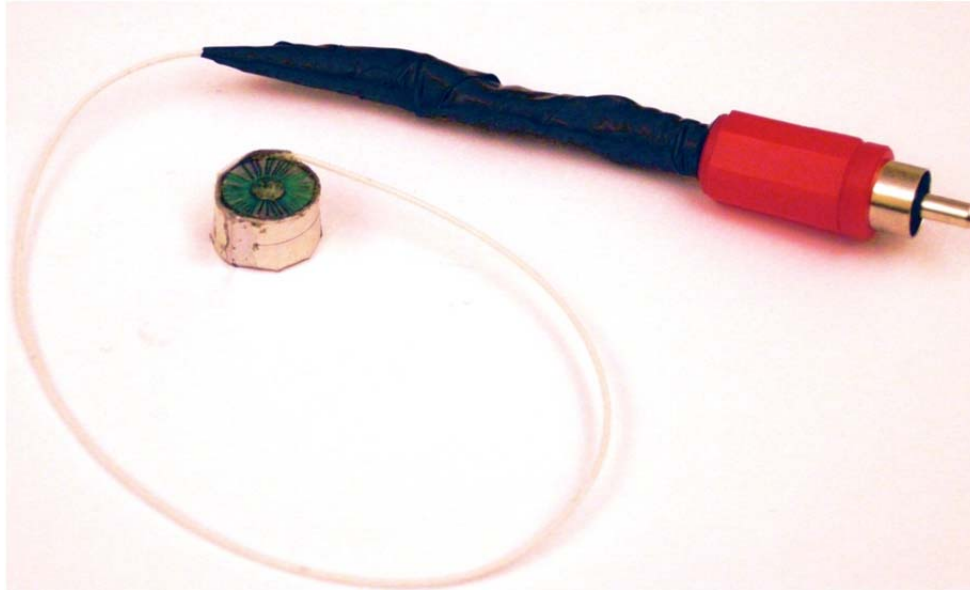


Figure 31 Prototype of omnidirectional SH-wave MEAS.

2.1.3.2. Shear-wave MEAS Performance

To ascertain experimentally whether or not the racetrack coil SH-wave MEAS indeed generate SH-waves in thin plates, dispersion curves were plotted. An elastic wave was transmitted with a MEAS, and received with a PWAS. The envelope of the received signal was calculated, and a threshold applied to the envelope to allow automatic detection of pulses. For reference, curves were first plotted for omnidirectional transducer C-1, and then compared to curves for SH-wave MEAS D-1 as illustrated in Figure 32.

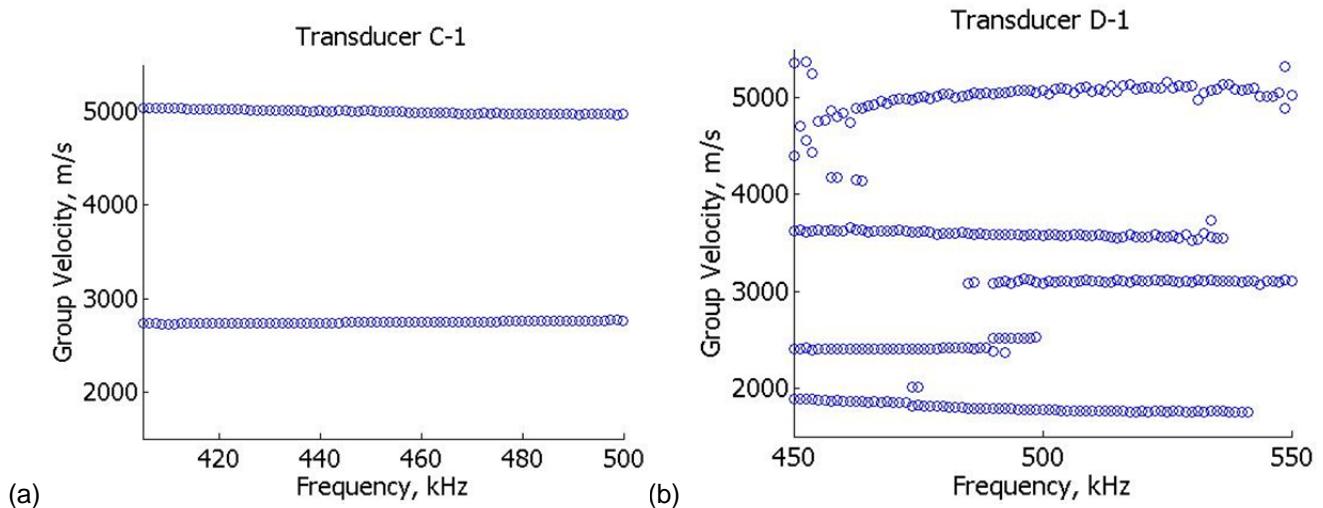


Figure 32 Dispersion data for omnidirectional transducer C-1 (a) and SH MEAS D-1.

Analysis of the figures above suggests that the D-series SH transducers excite wave modes that the C-series omnidirectional MEAS do not. However, rather than the expected appearance of a single, non-dispersive SH_0 pulse in addition to the S_0 and A_0 pulses, a number of additional wave modes are observed to appear. Dispersion data for D-4 shear-wave MEAS shows comparable results.

For all three transducers, the S_0 mode, with a characteristic group velocity of about 5000 m/s over this frequency range is clearly visible. For transducer C-1, the A_0 mode is also clearly visible, with a group velocity of about 2750 m/s. Both D-1 and D-4 show a wave mode with group velocity around 3100 m/s, which could represent the A_0 or SH_0 mode. However, with current measurement method, distinction between the two was not possible. In addition, PWAS is not configured to receive shear waves and hence reported results may be approximate at best.

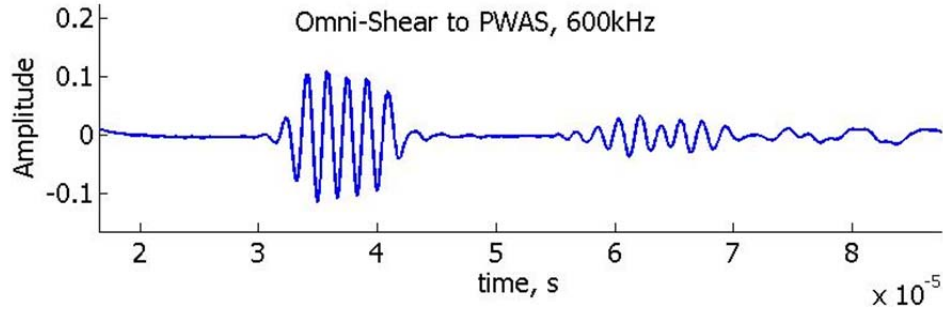


Figure 33 Typical signal transmitted by toroidal-coil MEAS and received by PWAS.

Two identical toroidal-coil MEAS were fabricated, and transmission between the two on a thin aluminum plate was attempted. However, no meaningful signals could be distinguished in the output of the receiving MEAS. Thus, a PWAS was substituted for the receiver, and each toroidal-coil MEAS was used in turn as a transmitter. A typical signal received using the PWAS is shown in Figure 33. Based on wave speed analysis, the first pulse in the figure must be the S_0 Lamb mode, while the second pulse is probably the A_0 Lamb mode. In some signal records, such as the one shown in Figure 33, the second pulse appears to consist of two overlapping pulses. If these are indeed two separate waves, then one of them may be the SH_0 mode. It should be mentioned, that the employed experimental setup did not allow for separation of A_0 and SH_0 components of the signal and therefore this observation may only serve as a working hypothesis.

It appears that MEAS for shear-wave generation and reception is, in principle, a viable technology, but further research and development will be required to fully realize it. If either of the two transducer designs presented above is to be employed for SH-wave SHM, they will need to be refined to improve signal-to-noise ratio, and further investigated to better understand the generated wave field.

2.2 MEAS Application in Magneto-Mechanical Impedance (MMI) Technology.

The magneto-mechanical impedance (MMI) technique provides a bridge between the mechanical impedance measurements (traditional or EMI) and the eddy current testing (Zagrai and Cakan, 2007); it is a unique technology developed in this project. The MEAS in MMI consists of an electrical coil and a permanent magnet. Introduction of the latter allows for the electromagnetic generation of elastic waves in electrically conductive materials. The continuous wave (CW) excitation applied to such a sensor leads to standing mechanical waves in the structural element and yields information on its mechanical vibration response within selected frequency range. The electromagnetically measured structural response is further used in the condition assessment procedures.

This section of the report discusses principles of the magneto-mechanical impedance identification of metallic structures. The underlying theory of the MMI is presented and particularities of mechanical and electromagnetic contributions in the MMI response are investigated. Experimental validation of the model and potential of the structural modal sensing are demonstrated. Details on practical application of the method are provided and examples of MMI diagnosis are considered.

2.2.1 Overview of the MMI Technology

The suggested experimental setup for magneto-mechanical impedance includes MEAS and HP 4192A impedance analyzer. However, an alternative setup involving a digital system based on 10 Ms/s multi-purpose DAQ card and National Instrument's NI ELVIS virtual instrumentation was developed and reported by this team (Zagrai and Cakan, 2010). Because the NI ELVIS based setup demonstrated higher noise level than HP 4192A, in the following discussion only data collected with the standard impedance analyzer HP 4192A is presented. In all tests, the impedance analyzer was controlled via a GPIB interface from a PC. A Labview[®] program was developed to communicate with the analyzer and to acquire impedance data. Schematic of the experimental setup with the HP 4192A impedance analyzer is illustrated in Figure 34.

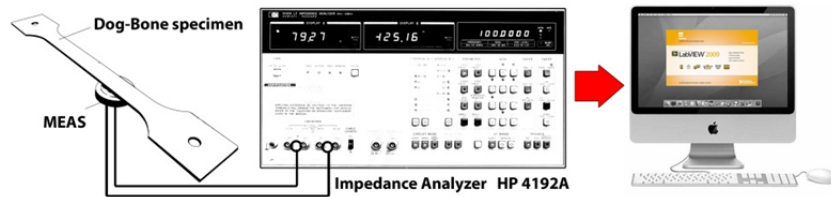


Figure 34 Experimental setup for MMI measurements using HP4192A phase gain impedance analyzer.

To illustrate application of the MMI technology to structural dynamic testing, consider an aluminum 2024-T3 beam (length – 304.8 mm, width – 25.4 mm, and thickness – 1.587 mm.) with free-free boundary implemented by suspending a beam on thin fishing line. MEAS was positioned underneath the beam with the gap of approximately 1 mm. Essentially, this setup of the experimental sample and the sensor permitted non-contact MMI measurements. MMI response of the aluminum beam obtained with to MEAS in 0.5-7 kHz frequency band is presented in Figure 35. Noticeable in the figure, the inductive component of the MEAS impedance is modulated the by structural dynamic contribution. Although the slope of the MMI response significantly depends on sensor characteristics as illustrated in Figure 35, impedance peaks associated with structural (mechanical) response are observed at the same frequencies in impedances of both sensors. This observation suggests independence of local impedance peaks from the magneto-elastic active sensor employed. For this reason, and in order to emphasize the structural dynamic contribution, the inductive contribution in the MEAS response may be eliminated by fitting it with a polynomial function and subtracting the resultant function from the total MMI response. A result of such processing of the MMI signature in Figure 35 is illustrated in Figure 36.

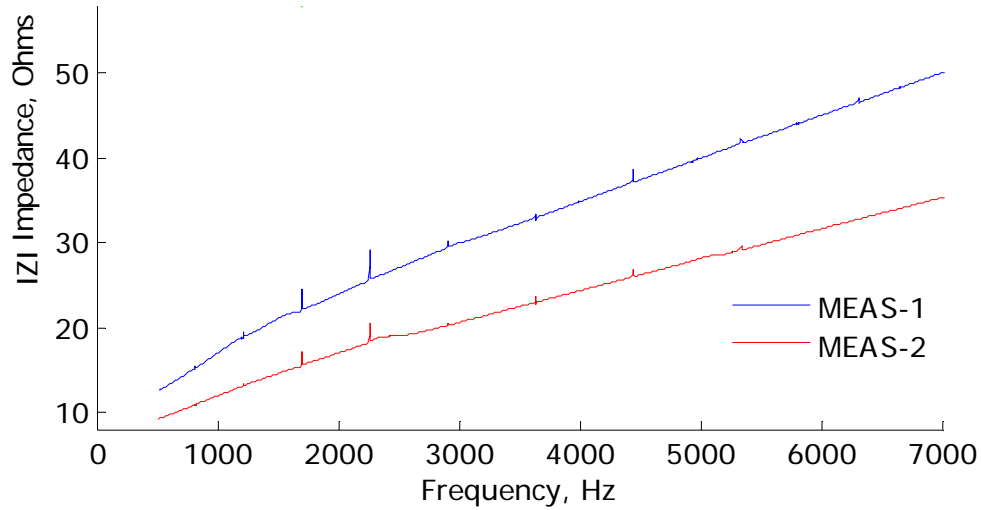


Figure 35 MMI responses of the aluminum beam measured with MEAS-1 and MEAS-2.

Also available in Figure 36 are theoretically calculated values of beam's natural frequencies. Correspondence between calculated natural frequencies and position of peaks in the MMI response is remarkable. We attribute very small differences between theory and experiment to limitations of the simplified beam theory used to calculate natural frequencies and to deviation of material parameters from the reported values. It should be noted that manifestation of impedance peaks in the MMI response depends upon MEAS position. This aspect of MMI measurements was thoroughly discussed in Zagrai, 2009. The effect is analogous to the selection of sensor placement in traditional structural dynamic tests. MEAS will not detect modes having a node at the measurement point.

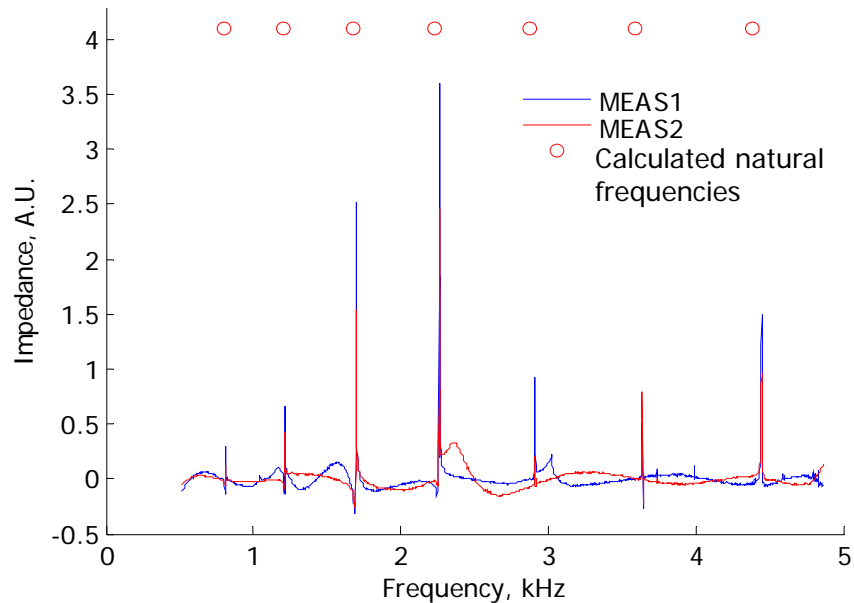


Figure 36 Structural responses extracted from MMI signatures and superimposed theoretically calculated natural frequencies of the free-free aluminum beam.

To confirm correspondence of the MMI peaks to the structural dynamic response, we conducted additional tests involving two identical aluminum beams. The beams were tested in free-free boundary condition with MEAS positioned in a non-contact mode at the center of the beam. Magneto-mechanical impedances for both beams were acquired with HP-4192A impedance analyzer. In addition, the electro-mechanical impedance (EMI) measurement was taken using a thin rectangular piezoelectric sensor bonded with the cyanoacrylate adhesive at the center of a beam. The MMI and EMI data were processed using a polynomial fitting procedure to yield responses presented in Figure 37. The figure suggests that MMI responses of two beams are nearly identical, which is expected for structures made of the same material and having similar geometrical dimensions. Although EMI data were acquired with a lower resolution, it is clear that both EMI and MMI responses reflect the same structural dynamic features. Since previous work on EMI (Park et al., 2003) has shown a direct relationship between the electro-mechanical impedance signature and the structural dynamic response, it is advocated that similar conclusion can be made about magneto-mechanical impedance of metallic structures.

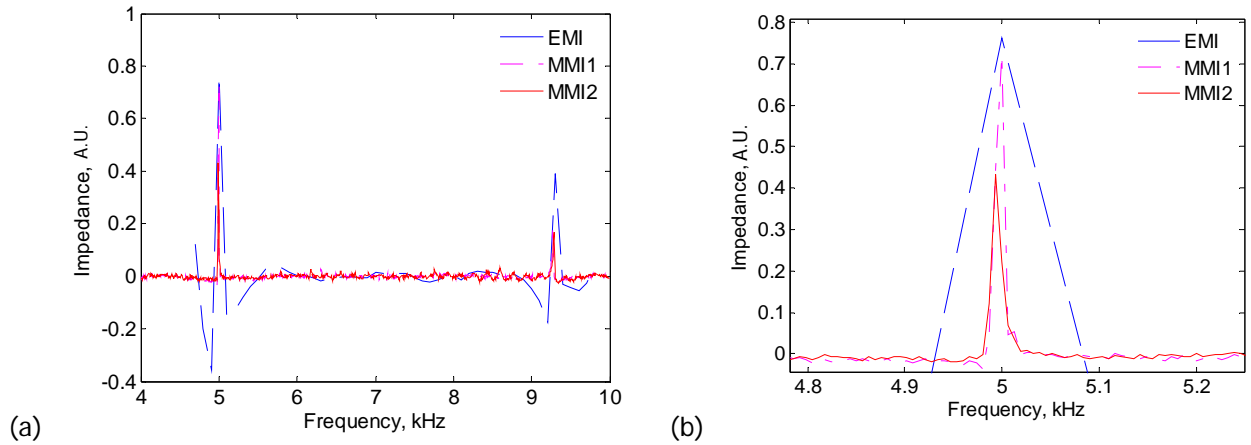


Figure 37 (a) Magneto-mechanical and electro-mechanical impedances of small aluminum beams. (b) Details of MMI and EMI responses at 5 kHz.

2.2.2 MMI Analytical Modeling

Electromagnetic generation and reception of elastic waves facilitates utilization of MEAS in both impulse and CW modes. In the latter case, standing waves are formed in the structure and the resonant behavior can be observed at respective natural frequencies. It is evident that the model describing the MMI response must include structural dynamics, MEAS electromagnetic characteristics, and the sensor/structure interaction mechanism (Zagrai, 2009). In non-ferromagnetic metallic structures, interaction between MEAS and a structural element is accomplished via the Lorentz force.

$$F_L = \int_V J \times B \, dV, \quad (5)$$

where J is the electric current and B is the magnetic induction. According to Eq. (5), the Lorentz force depends on mutual orientation of J and B , which are controlled by the coil design and the magnet assembly respectively. MEAS consists of a pancake coil and a permanent magnet arranged as illustrated in Figure 1. Spatial distribution of the Lorentz force for the sensor design in Figure 1 is rather complex and may be obtained by calculating the integral in Eq. (5). Work of Sodano et al. (2006) may be consulted for details on calculating such integrals and obtaining associated spatial distributions.

It should be remembered that the Lorentz force generated by MEAS in Figure 1 consists of horizontal and vertical components. In principle, such a force could excite both longitudinal and flexural vibrations. In the developed model, however, we considered only a vertical component responsible for

excitation of flexural vibrations in a one-dimensional structure – the Euler-Bernoulli beam. A complex distribution of the Lorentz force is reduced to three cases approximating spatial effects of the sensor placement. Figure 38 signifies (a) an infinitely small sensor positioned at x_{fa} , (b) a sensor of length L_a exerting forces at x_a and $x_a + L_a$, and (c) a sensor of length L_a exerting linearly distributed forces. Formulations associated with each excitation force are as follows:

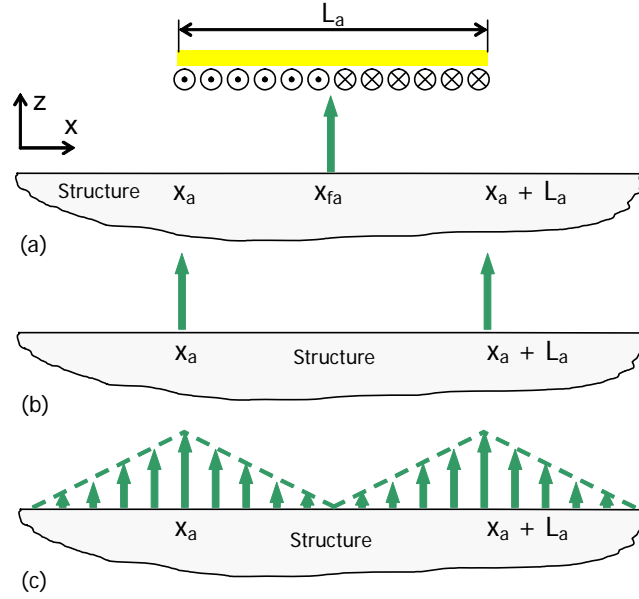


Figure 38 Vertical component of the excitation force exerted by MEAS onto the metallic structure: (a) single-point load, (b) pin-force load, (c) triangular load.

$$F_s(x, t) = J_y \cdot B_x \cdot b_a \cdot \delta(x - x_{fa}) \cdot e^{i\omega t}, \quad (6)$$

$$F_p(x, t) = J_y \cdot B_x \cdot b_a \cdot 0.5 \cdot (\delta(x - x_a) + \delta(x - (x_a + L_a))) \cdot e^{i\omega t}, \quad (7)$$

$$F_T(x, t) = J_y \cdot e^{i\omega t} \cdot B_x \cdot b_a \cdot \begin{cases} [x + L_a - x_a]/L_a & x_a - L_a < x \leq x_a - L_a/2 \\ [x_a - x]/L_a & x_a - L_a/2 < x \leq x_a \\ [x - x_a]/L_a & x_a < x \leq x_a + L_a/2 \\ [x_a + L_a - x]/L_a & x_a + L_a/2 < x \leq x_a + L_a \\ 0 & \text{otherwise} \end{cases}, \quad (8)$$

where J_y is the electric current, B_x is magnetic induction, L_a is the x-axis dimension of the sensor, b_a is the y-axis dimension of the sensor equal to beam's width, x_{fa} and x_a denote position of the sensor in single-point and pin-force excitation models described by Dirac delta function $\delta(x)$. Harmonic steady-state excitation with frequency ω is assumed as indicated by the exponential term in the force definition.

2.2.2.1. Generalized Structural Response of the Elastic Beam

One-dimensional structure in this study is the Euler-Bernoulli beam subjected to the Lorentz force defined by Eqs. (6)-(8). Forced flexural vibration of such a structure is described by a non-homogeneous partial differential equation in terms of displacement $w(x, t)$.

$$\rho A \cdot \frac{\partial^2 w(x, t)}{\partial t^2} + EI \cdot \frac{\partial^4 w(x, t)}{\partial x^4} = F_L(x, t) \quad (9)$$

The equation above includes parameters of the beam: density – ρ , modulus of elasticity – E , cross-sectional area – A , and moment of inertia – I . Eq. (9) is solved using modal expansion.

$$w(x, t) = \sum_{n=0}^{\infty} W_n(x) \cdot T_n(t) \quad (10)$$

where the spatial modal distribution is governed by

$$W_n(x) = A_n \left[\cosh \gamma_n x + \cos \gamma_n x - \sigma_n (\sinh \gamma_n x + \sin \gamma_n x) \right]. \quad (11)$$

Amplitude of the modes is $A_n = 1 / \sqrt{\int_0^L W_n^2(x) dx}$, where L is the length of the beam. Modal parameters in Eq. (11) are calculated numerically for a particular set of boundary conditions. Although free-free boundary conditions are considered in this study, the presented theoretical development is rather and permits incorporating other sets of structural constraints. Most textbooks provide tabulated values for γ_n and σ_n , which for free-free boundary conditions and $n > 5$ yield $\gamma_n = 0.5 \cdot \pi (2n+1) / L$ and $\sigma_n = 1$. Natural frequencies can be determined using formulations $\omega_n = \gamma_n^2 c_w$ and $c_w = \sqrt{EI / \rho A}$.

The temporal component in Eq. (10),

$$T_n(t) = C_n \cdot e^{i\omega t}, \quad (12)$$

includes a harmonic term and the modal participation factor C_n . The latter is obtained by substituting the modal expansion (10) into the governing equation (9) and employing the orthogonality condition. For the system with damping, modeled using the viscous damping ratio for each vibration mode – ζ_n , modal participation factor is

$$C_n = \frac{1}{\rho A} \sum_{n=0}^{\infty} \int_0^L W_n(x) \cdot F_L(x) dx / \left(\omega_n^2 + 2i\zeta_n \omega_n \omega - \omega^2 \right). \quad (13)$$

Substitution of (13) into (10) yields displacement

$$w(x, t) = \sum_{n=0}^{\infty} \frac{W_n(x) \cdot WF_n(x)}{\rho A \cdot \left(\omega_n^2 + 2i\zeta_n \omega_n \omega - \omega^2 \right)} \cdot e^{i\omega t}, \quad (14)$$

where $WF_n(x) = \int_0^L W_n(x) \cdot F_L(x) dx$ accounts for the applied force $F_L(x)$.

In impedance diagnosis, the magneto-elastic active sensor is utilized not only to exert the excitation force, but also to sense the structural response. Due to the reciprocal effect (Turner et al., 1969), the elastic wave propagating under MEAS induces voltage, V , in the sensor coil, which can be described in terms of vibration velocity $\dot{w}(x, t)$ and magnetic induction B_x . Distribution of the magnetic induction along y axis (beam's width) is assumed constant and hence

$$V = \int_0^{L_{Sa}} \int_0^{b_a} \dot{w}(x, t) \cdot B_x dx dy = b_a \cdot \int_0^{L_{Sa}} \dot{w}(x, t) \cdot B_x dx, \quad (15)$$

where L_{Sa} is MEAS sensing range.

The resultant impedance defined as a voltage/current ratio is

$$Z_{str}(\omega) = \frac{V}{J_y} = \sum_{n=0}^{\infty} \frac{i\omega \cdot b_a \cdot \int_0^{L_{sa}} B_x \cdot W_n(x) \cdot WF_n(x) dx}{J_y \cdot \rho A \cdot (\omega_n^2 + 2i\zeta_n \omega_n \omega - \omega^2)}. \quad (16)$$

Structural impedance in Eq. (16) is derived for the general form of the excitation force $F_L(x)$. A specific function or a tabulated curve can be used for $F_L(x)$ of the complex shape. In this case, impedance in Eq. (16) is determined numerically. Below, we provide three analytical solutions aimed at modeling the spatial effect of the magneto-elastic sensor.

2.2.2.2. Response to Various Excitation Forces

2.2.2.2.1. Single-point load

Consider a single point load described by Eq. (6). For the load applied at x_{fa} , the component associated with the structural excitation yields

$$WF_n(x) = \int_0^L W_n(x) \cdot J_y \cdot B_x \cdot b_a \cdot \delta(x - x_{fa}) dx = J_y \cdot B \cdot b_a \cdot W_n(x_{fa}). \quad (17)$$

Substitution of (17) into the impedance (16) results in the formulation describing structural impedance due to the point load.

$$Z_{str}(\omega) = \sum_{n=0}^{\infty} \frac{i\omega \cdot (b_a \cdot B_x \cdot W_n(x_{fa}))^2}{\rho A \cdot (\omega_n^2 + 2i\zeta_n \omega_n \omega - \omega^2)} \quad (18)$$

2.2.2.2.2. Pin-force load

The pin-force model reflects the notion that vertical components of the Lorentz force are maximized in the area close to MEAS ends. Hence, excitation occurs at the MEAS end-points x_a and $x_a + L_a$, where L_a is MEAS length as illustrated in Figure 38. The excitation force (7) yields the structural impedance

$$Z_{str}(\omega) = \sum_{n=0}^{\infty} \frac{i\omega \cdot (b_a \cdot B_x \cdot (W_n(x_a) + W_n(x_a + L_a)))^2}{4 \cdot \rho A \cdot (\omega_n^2 + 2i\zeta_n \omega_n \omega - \omega^2)}. \quad (19)$$

2.2.2.2.3. Triangular load

Triangular load emulates the distributive nature of the applied force. This distribution arises due to a cumulative effect of eddy currents generated by individual wires in the MEAS coil. The excitation force described by Eq. (8) can be generalized as

$$F_T(x, t) = J_y \cdot B_x \cdot \pm(x + C) \cdot e^{i\omega t} \cdot b_a / L_a, \quad (20)$$

where C is a constant containing x_a and L_a or only x_a for four regions indicated in Eq. (8). Substitution of $F_T(x, t)$ into Eq. (16) results in the structural impedance

$$Z_{str}(\omega) = \sum_{n=0}^{\infty} \frac{i\omega \cdot (b_a \cdot B_x)^2 \cdot \int_0^{L_{sa}} W_n(x) \cdot \pm(x + C) \cdot \left(\int_0^L W_n(x) \cdot \pm(x + C) dx \right) dx}{L_a^2 \cdot \rho A \cdot (\omega_n^2 + 2i\zeta_n \omega_n \omega - \omega^2)}. \quad (21)$$

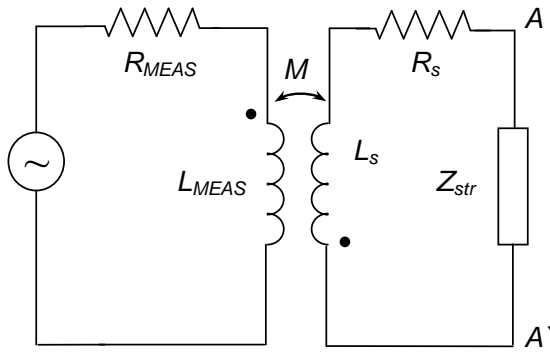


Figure 39 Equivalent circuit for magneto-elastic active sensing.

The structural impedance $Z_{str}(\omega)$ in expressions (16), (18), (19), and (21) was derived under an assumption of ideal electromagnetic coupling between MEAS and the structure. It should be noted that these expressions do not contain the impedance contributed by the sensing element. To account for both effects, a transformer and an associated equivalent electrical circuit are introduced in the MMI model.

2.2.2.3. Electro-magnetic coupling and sensor contribution

In the magneto-mechanical impedance measurement, generation and reception of the elastic wave in the material under test is facilitated by the transmitter/receiver containing coil and magnet. Transformation of the supplied electric signal into the elastic wave generated in the metallic structure depends on many factors: MEAS size and geometry, characteristics of the metallic structure, sensor lift-off, and others. Detailed investigation of these factors for each diagnostic scenario requires accurate multi-physics finite element models. Alternatively, the electro-magnetic interaction between a sensor coil and a test sample can be described using a transformer with mutual inductance M (Cartz, 1995). The transformer circuit, illustrated in Figure 39, accounts for inductance of the sensor L_{MEAS} , resistance of the sensor R_{MEAS} , inductance and resistance of the metallic structure L_S and R_S , and the coupling between the structure and the sensor represented with the coefficient M . Terminals A-A' in the circuit diagram indicate contribution of the dynamic impedance $Z_{str}(\omega)$ associated with structural resonances in the sample. The cumulative impedance seen by the magneto-elastic sensor can be obtained directly from the transformer circuit in Figure 39.

$$Z(\omega) = R_{MEAS} + i\omega L_{MEAS} + \frac{\omega^2 M^2}{i\omega L_S + R_S + Z_{str}(\omega)}. \quad (22)$$

The electromagnetic coupling in Eq. (22) is defined in terms of a mutual inductance M . For modeling purposes, it is convenient to relate the mutual inductance to the electromagnetic coupling coefficient, k_C , ranging from 0 (no coupling) to 1 (perfect coupling). The electromagnetic coupling coefficient is represented according to the following expression (O'Malley, J., 1992):

$$k_C = M / \sqrt{L_S L_{MEAS}}. \quad (23)$$

Substitution of Eq. (23), into Eq. (22) yields a formulation describing the magneto-mechanical impedance measured at the MEAS terminals:

$$Z(\omega) = R_{MEAS} + i\omega L_{MEAS} + \frac{\omega^2 L_{MEAS} L_S \cdot k_C^2}{i\omega L_S + R_S + Z_{str}(\omega)}. \quad (24)$$

The impedance presented in Eq. (24) includes the structural dynamic contribution via $Z_{str}(\omega)$, electro-magnetic coupling, and sensor characteristics.

2.2.2.4. Experimental data and results of analytical calculations.

In the following discussion, results of theoretical calculations using Eq. (24) and experimental data obtained in MMI experiments are compared. The aim of presented analysis is to demonstrate that a mechanical response can be inferred from the electrically measured MMI signature and to validate the developed analytical modeling approach.

An experimental sample utilized in the model validation experiments was an aluminum 2024T3 beam with length $L = 304.8$ mm, width $w = 25.4$ mm, and thickness $h = 1.587$ mm. Information on the exact material properties of the sample was not available and approximate values for the indicated aluminum alloy were assumed as follows: modulus of elasticity $E = 73.1$ GPa, density $\rho = 2780$ kg/m³. In the experiments, the beam was suspended in air using thin fishing to simulate free-free boundary conditions considered in the theoretical development. The magneto-mechanical impedance was measured in the non-contact mode with the 1 mm air gap between the sensor and the test specimen. To facilitate direct access to the specimen and to eliminate influence of sensor mechanical characteristics on the structural dynamic response, MEAS was positioned underneath the beam as illustrated in Figure 34. Terminals of the magneto-elastic active sensor were connected to HP 4192A impedance analyzer interfaced with a personal computer using a HPIB connector. A virtual instrument software module developed in NI Labview[®] was utilized to control settings of the impedance analyzer and to acquire the experimental data. MMI response of the aluminum beam was obtained by sweeping the excitation signal in the lower kHz frequency range. The MMI response of the aluminum beam measured in the experiment with the MEAS positioned at the $\frac{1}{4}$ of beam's length is presented in Figure 40 as a solid red line. As it could be seen from the Figure 40a, the measured MMI signature includes contribution of the sensor (related to the impedance slope) and dynamics of the test structure reflected in the impedance peaks.

Theoretical calculation of the MMI response were performed using analytical expressions (18), (19), (21) and (24) discussed in the preceding sections of the report. MEAS characteristics appearing in the formulations were determined experimentally from the impedance measurements: inductance - $L_{MEAS} = 1.9$ mH and resistance - $R_{MEAS} = 10$ Ω . The parameters of the structure and the coupling coefficient were estimated as $L_S = 0.1$ μ H, $R_S = 0.8$ m Ω and $k_C = 0.4$. The calculated MMI responses to three types of structural excitation are presented in Figure 40. MMI signatures in a broad frequency range are illustrated in Figure 40a. Noticeably in the figure, the position of impedance peaks in theoretical responses match well with peaks in the curve obtained experimentally. Minor discrepancies in the position of peaks may be attributed to limitations of the Euler-Bernoulli beam theory employed for modeling the 1-D structure. Slopes of theoretical and experimental impedance curves are comparable, but the difference increases at high frequencies. Below only most important contributions into MMI model are considered. Additional material is available in the Zagrai and Cakan (2010) publication on this subject.

2.2.2.4.1. Contribution of the applied load

To investigate impedance changes in the vicinity of impedance peaks, the narrowband responses were considered. The experimental data obtained in different frequency bands are presented in Figure 40b,c,d as solid red curves. Dashed blue, dashed purple, and dotted green, curves represent theoretical responses obtained under different configurations of the excitation force. The largest amplitude of the impedance peaks is observed for the case of the single point excitation. In general, this model is recommended when dimensions of the sensor are an order of magnitude smaller than dimensions of the inspected structural element. The pin-force model considers two point loads applied at the end of the sensor and results in lower amplitude of the impedance peak due to influence of the load spatial location on amplitude of the excited vibration mode. The triangular excitation yields results comparable to the pin-force model, but with slightly smaller amplitude of impedance peaks. It is suggested that the distributive nature of this load is responsible for reduction of vibration amplitude.

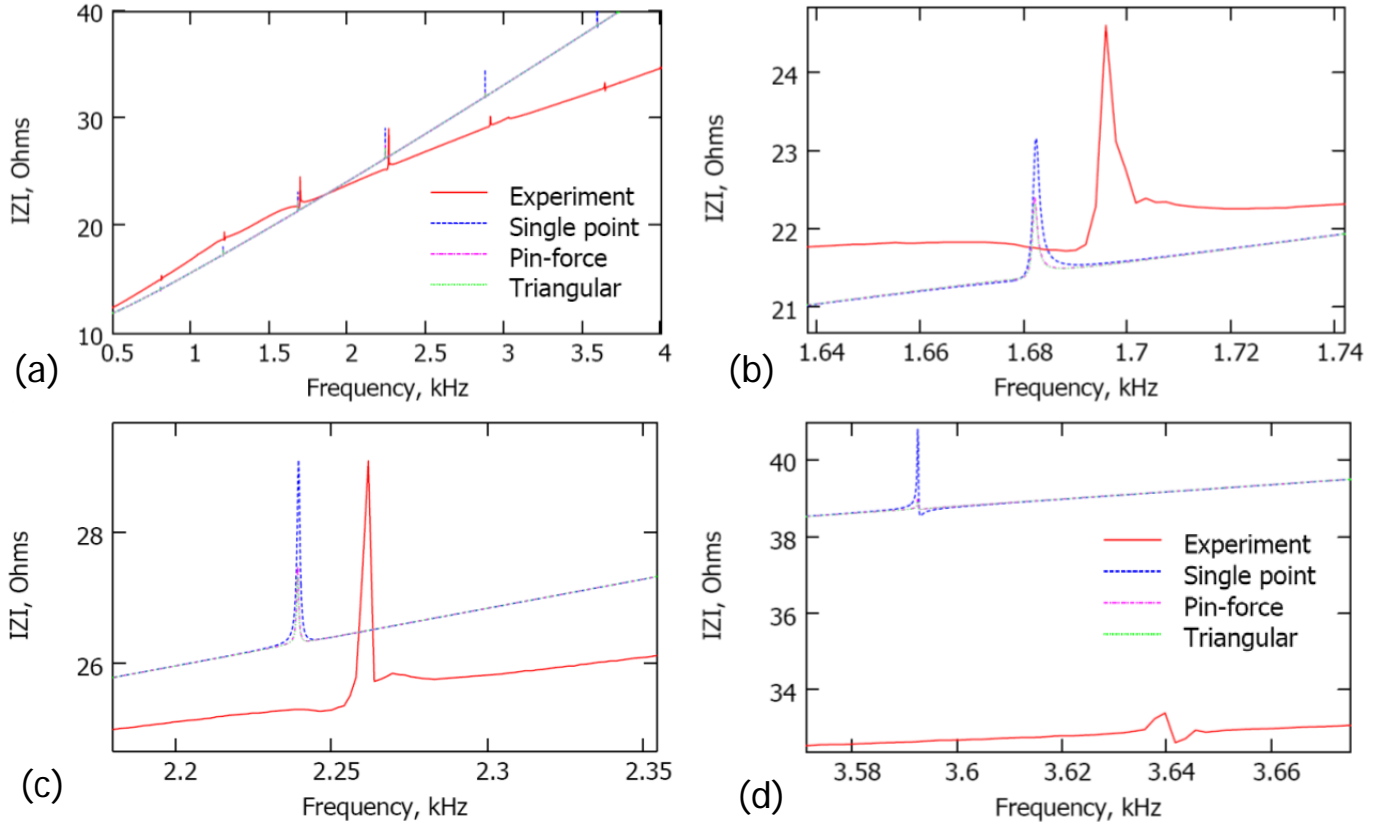


Figure 40 Theoretically calculated and experimentally measured MMI responses of an aluminum beam. Broadband (a) and narrowband (b), (c), (d) representations of MMI.

2.2.2.4.2. Effect of electrical parameters

Impedance signatures presented in Figure 40 in the narrow frequency band reveal an interesting effect related to position of the impedance minimum. At relatively low frequencies (Figure 40b), a minimum of the MMI response precedes the impedance maximum. However, at moderate frequencies (Figure 40c), the MMI response before and after the impedance peak is relatively flat so that position of the impedance minimum is difficult to discern. This situation changes at higher frequencies, Figure 40d, where the impedance minimum occurs after the impedance maximum. It should be mentioned that in impedance measurements with piezoelectric sensors position of the impedance minimum is stable – before the impedance maximum. Because an equivalent structural response participates in both electro-mechanical, (Liang et al., 1994), and magneto-mechanical impedance measurements, the mechanical part is unlikely to cause such an unusual impedance manifestation. It is suggested that the observed effect may be attributed to electrical characteristics of the experimental setup and particularities of the sensor/structure interaction.

Analysis of Eq. (24) reveals that position of the impedance minimum is influenced by the electrical resistance R_S and inductance L_S of the structural element. Theoretical calculations were performed using expressions (18) and (24) for the resistances ranging from $R_S = 0.8 \text{ m}\Omega$ to $R_S = 2.4 \text{ m}\Omega$ (i.e. $R_S, 2R_S, 3R_S$) and inductances ranging from $L_S = 0.1 \text{ }\mu\text{H}$ to $L_S = 0.3 \text{ }\mu\text{H}$ (i.e. $L_S, 2L_S, 3L_S$). Results of the calculations illustrated in Figure 41 suggest that increasing of R_S leads to pronounced manifestation of impedance minimum before the impedance peak. In contrast, increasing if L_S causes impedance minimum occurring after the impedance peak. The analytical model incorporating R_S and L_S in Eq. (24) rather accurate describes frequency-dependent changes in position of impedance minima as

illustrated in Figure 40 showing the experimental data (red lines) and theoretically calculated MMI responses (blue lines). Theoretical MMI curves clearly indicate changes in position of the impedance minimum. Based on these observations, it is suggested that electrical characteristics of the structural element noticeably affect the MMI response and need to be accounted for in theoretical models and experimental practices.

It should be mentioned that the presented model allows for studying influence of additional factors on MMI responses. Such parameters include influence of MEAS position, MEAS characteristics, number and strength of permanent magnets and are thoroughly discussed in the corresponded journal paper (Zagrai and Cakan, 2010). For the brevity of the discussion and availability of the reference, they are not included in this report.

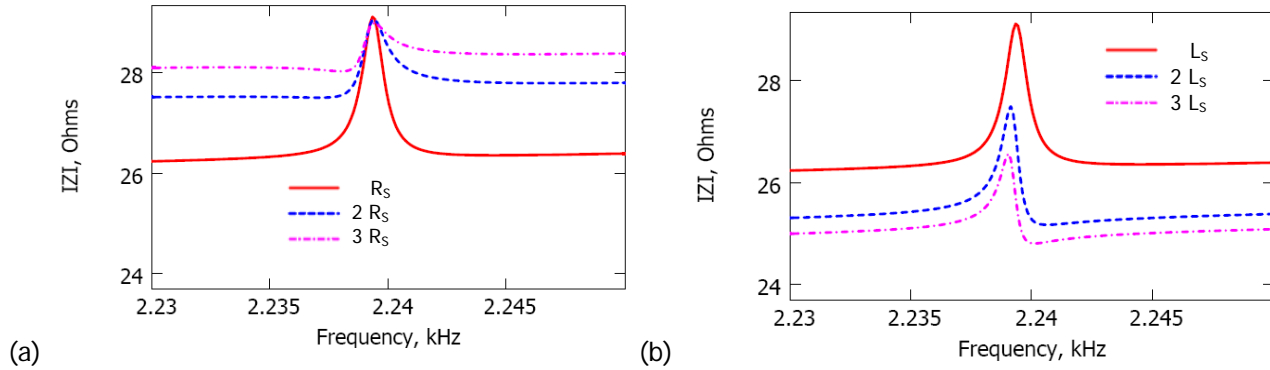


Figure 41 Effect of resistance (a) and inductance (b) of the structural element on the magneto-mechanical impedance.

2.2.3 Semi-Analytical MMI Model for Complex Structures

The analytical model discussed above accounts for a complete structural frequency response, electrical parameters of structural material as well as MEAS characteristics and position on a structure. The available analytical formulation describing the total impedance measured at sensor terminals is Eq. (24). The structural impedance in this equation appears as (Barnes et al., 2009)

$$Z_{str}(\omega) = i\omega \cdot (b_a \cdot B)^2 \cdot FRF(\omega), \quad (25)$$

where B is magnetic induction, b_a is lateral dimension of the sensor and $FRF(\omega)$ is structural frequency response function. In the presented development, $Z_{str}(\omega)$ is determined analytically for a structure of simple geometry – an elastic beam. In practical tests, however, structures of complex geometry are often investigated and this necessitates using the finite element analysis (FEA) to determine structural contribution in the total impedance. Hence, it is suggested that expression (24) can be employed in conjunction with (25), where structural frequency response function is calculated using FEA. A structure of complex geometry – an aluminum 6061 dog-bone specimen machined in accordance with ASTM 557M standard, was considered for validating the proposed concept (Figure 42a). A frequency response function was calculated with the help of Comsol finite element package and substituted into equation (25) for structural impedance. Calculations assumed a single point excitation resulting in predominantly flexural vibrations of the structure.

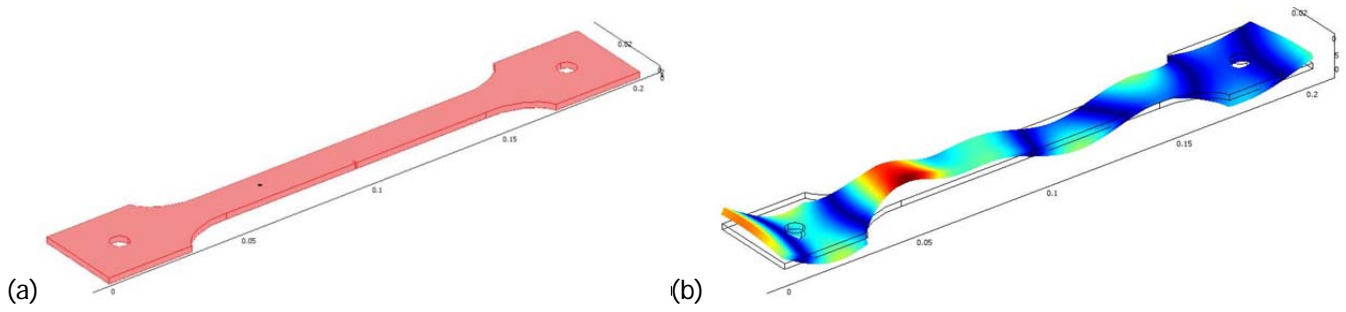


Figure 42 (a) Geometry of the dog-bone specimen used in FEA; (b) FEA results for one of vibration modes of the dog-bone specimen.

Excitation force was applied at the beginning of the thin section of the dog-bone specimen, as could be inferred from Figure 42b showing one of specimen's vibration modes. Finally, the impedance seen at sensor terminals was obtained by substituting equation (25), into equation (24). Parameters utilized in the calculation of the total impedance included: $L_{MEAS}=0.152$ mH, $R_{MEAS}=2.45$ Ω , $L_S=5 \cdot 10^{-8}$, $R_S=8 \cdot 10^{-4}$ Ω , $k_C=0.4$. To verify applicability of the proposed semi-analytical modeling procedure, an actual dog-bone specimen was tested in free-free boundary conditions. During experiments, MEAS was positioned underneath the specimen in the non-contact mode with 0.5 mm air gap. A HP4192A impedance analyzer was employed to measure MMI of the sensor-structure system.

Experimentally determined MMI of the aluminum dog-bone sample is presented in Figure 43 as a solid red curve. The blue curve corresponds to MMI calculated using the described semi-analytical model. Figure 43 indicates rather accurate matching of experimental and theoretical data. Slight deviations between the curves may be attributed to variability of electrical parameters and difficulties in achieving an exact match of modeled and actual structural geometries.

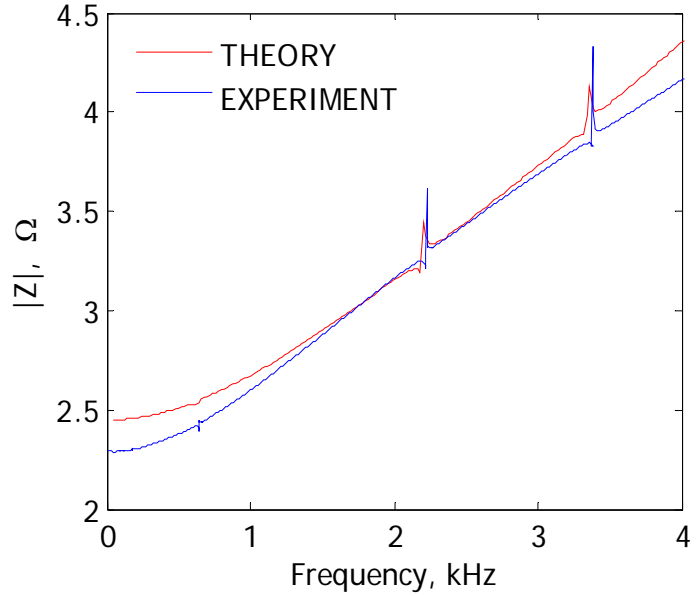


Figure 43 Comparison of experimental and theoretical MMI responses of the dog-bone specimen.

2.2.4 Examples of MMI SHM Applications

The magneto mechanical impedance technique explores electromagnetic excitation of structural vibrations and thus permits inferring structural dynamic characteristics. Changes in structural boundary conditions and/or variation in structural material properties may alter structural dynamics and, as a result, change the MMI signature. This effect motivates consideration of MMI for structural health monitoring and nondestructive evaluation (Barnes et al., 2009).

2.2.4.1. Aluminum samples with structural notches and a fatigue crack.

In the following section, effect of structural notches (structural cracks) on the MMI response of aluminum beams is investigated. Three different types of the aluminum 2024-T3 alloy specimens were considered, one – in pristine condition; second – with 0.3 mm cut at the 37mm distance from the one end of the beam; third – with the same size, two-sided cut at the same distance from the end (Figure 44).

Geometry of samples was: length - 150mm, width – 12.5mm, thickness – 1.5mm. Each experimental specimen was suspended on a fishing line to simulate free-free boundary condition. The MEAS was placed under the aluminum specimen. The distance from MEAS to specimen was maintained approximately 0.5mm.

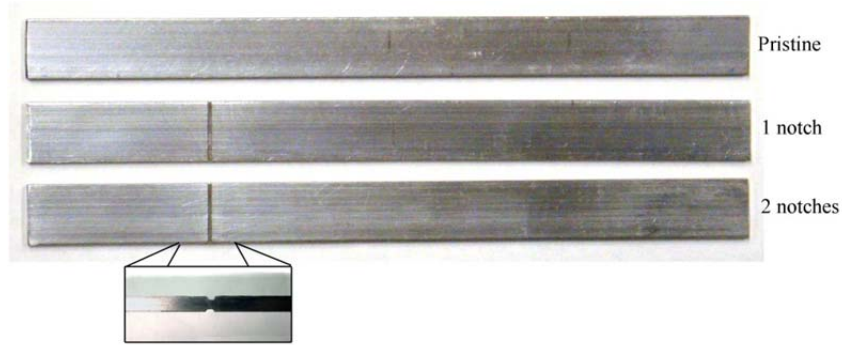


Figure 44 Aluminum beam used in experiments.

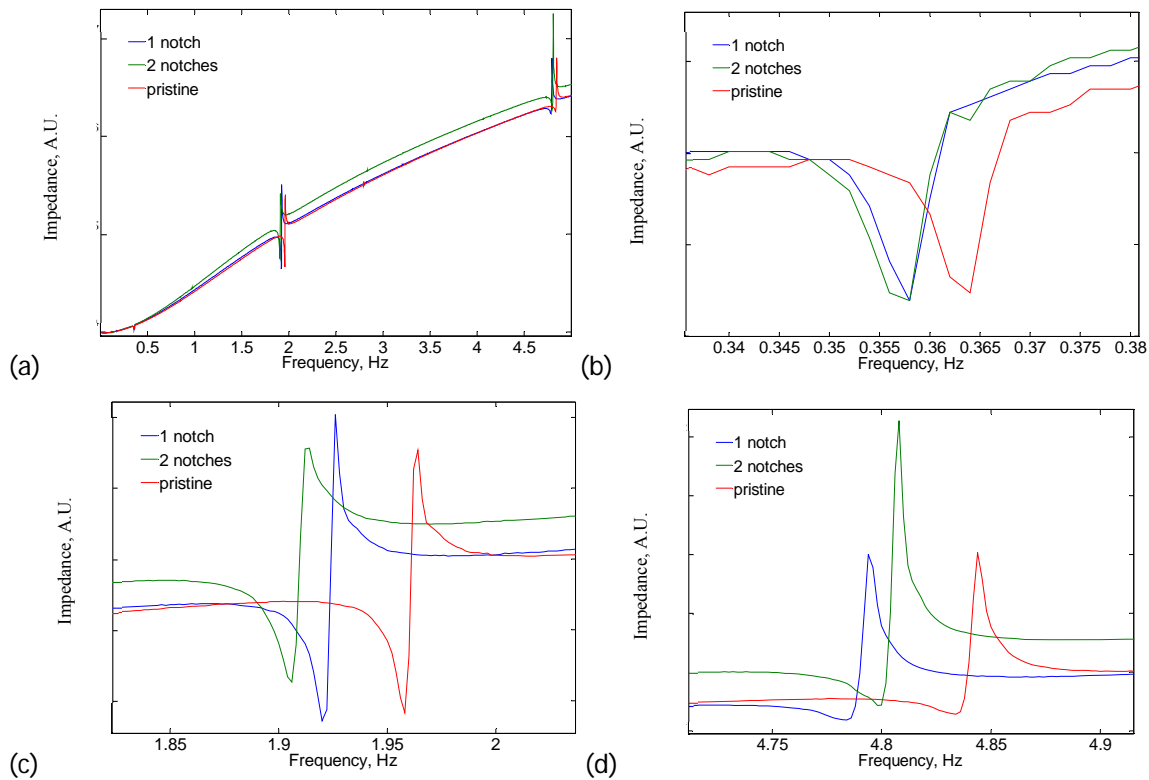


Figure 45 Magneto-mechanical impedance of beams (a) and (b,c,d) with selected zoom-in

The MMI response of aluminum beams are presented in Figure 45a with zoomed-in impedance peaks in (b), (c), and (d) portions of the figure. The latter shows decreasing of the impedance peak frequency as the imitated crack (notch) starts appearing on it. High frequencies in the MMI spectra show larger change due to presence of notches than the low frequencies. Therefore, it is suggested that the higher the operation frequency range, the higher possibility to detect damage.

Although structural damage in the form of a notch could provide a reasonable imitation of an open crack, by all means, a notch can not fully represent a fatigue crack. For this reason, an aluminum sample with real fatigue crack was considered in an additional set of experiments.

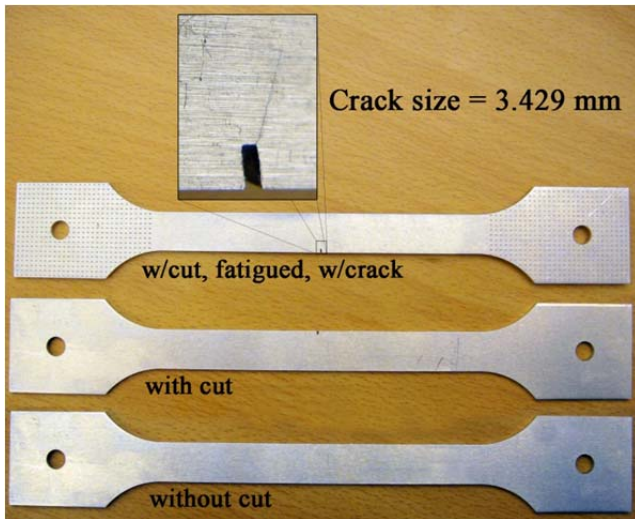


Figure 46 Dog-bone specimens measured in test.

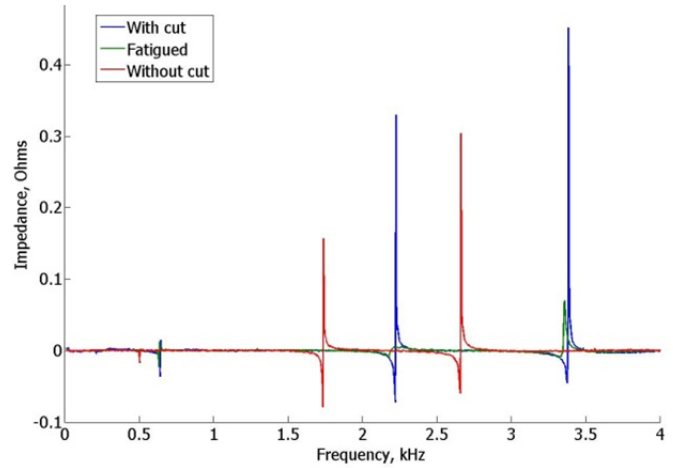


Figure 47 Dog-bone specimens MMI signatures.

A set of samples included three dog-bone specimens depicted in Figure 46: intact specimen (undamaged) without the crack initiation notch, intact specimen with the crack initiation notch, and a specimen fatigued up to initiation and development of 3.4 mm fatigue crack. Instrumentation utilized in MMI experiments included HP 4192A impedance analyzer and MEAS positioned in the non-contact mode underneath the aluminum specimen. Free-free boundary conditions were implemented by supporting the specimen on thin fishing lines. Experimental data were collected via Labview interface and were imported in Matlab for further processing and analysis. In order to reduce contribution of inductive components masking manifestation of structural dynamic features in the MMI signature, the raw data was fitted with a polynomial, which was then subtracted from the original data. Processed experimental results are presented in Figure 47. Noticeable in the Figure 47, a specimen without the crack initiation notch (cut) shows considerably different response than specimens with the cut. Frequencies of impedance peaks in response of the specimen without the cut are lower. Specimens with cuts show comparable MMI signatures, but frequencies of impedance peaks in the response of the sample with a crack are lower than frequencies found in response of the undamaged sample. Possibly, this indicates a local stiffness reduction of the specimen. It should be noted that larger differences were observed for higher frequencies due to apparent stiffness reduction. This experimental observation proves effectiveness of MMI in detection of fatigue crack.

2.2.4.2. Fatigued dog-bone specimens.

The capability of the magneto-mechanical impedance method to detect and monitor fatigue damage was explored in a series of tests using aluminum 2024-T3 Dog-bone specimens with increasing accumulation of fatigue damage. Fatigue testing was carried out with an MTS Landmark material testing machine configured for 10 Hz harmonic load. Data on the magneto-mechanical impedance of the dog-bone samples was collected at a designated number of fatigue cycles labeled as fatigue increments in Table 8 . Fatigue settings for each tested sample are presented in the same table.

During the MMI measurements, the specimens were removed from the testing machine, suspended on a fishing line to approximate free-free boundary conditions, and interrogated with MEAS positioned in a non-contact mode approximately 0.5 mm from the specimen's surface and 70 mm from one of specimen's ends. The resulting MMI signatures for eight samples measured at different stages of fatigue process are illustrated in Figure 48 through Figure 51. The MMI responses of samples are presented with zoom-in impedance peaks in (b), (c), and (d) portions of the figure.

Table 8 Fatigue characteristics of experimental samples in MMI tests.

Sample ID	Stress Level	F_{max}, kN	R - ratio	Fatigue increments in number of cycles	Comments
S2B	155	1.45	0.1	Unfatigued 10,000	no crack
S3B	155	1.45	0.1	Unfatigued 10,000 15,500	Crack appeared at 15,500 cycles
S4B	120	1.45	0.1	Unfatigued 12,000 24,000 36,000	no crack
S5B	100	1.0104	0.1	Unfatigued 12,000 24,000 36,000 48,000	no crack
SXB	120	2.204	0.1	Unfatigued 10,000 20,000	with external hole, Broke at 29,252 cycles
SYB	100	1.0104	0.1	Unfatigued 10,000 20,000 30,000 40,000 50,000	with external hole, no crack
S2Ba	100	1.0104	0.1	Unfatigued 12,000	no crack
S3Ba	100	1.0104	0.1	Unfatigued 12,000 24,000	no crack

In general, decreasing of the impedance peak frequency as the sample was degrading under fatigue load was observed. Higher frequencies in the MMI spectra show larger change in the frequency value than the lower frequencies. It should be noted that the last measurement point for sample S3B (Figure 48) was collected when a fatigue crack appeared at 15,500 cycles; this sample was fatigued under 1.45 kN load at 155 MPa stress level. Specimen S3Ba (Figure 49) was fatigued under lower load conditions and did not show any sign of fatigue crack. Noticeably, this sample shows a less stable frequency shift due to fatigue with frequency of intact sample being lower than frequency at some fatigue level. Such a behavior was observed for some samples, but majority of data followed the stable pattern depicted in other figures. Lower fatigue load and stress level have been used for the S5B dog-bone (Figure 50). It was fatigued to 48,000 cycles. Impedance data taken after each fatigue stage (12,000-24,000-36,000-48,000), showed a clear frequency shift toward lower values as the specimen was subjected to increasing level of fatigue. results – produced larger frequency shift. Figure 52 shows two slightly different geometry dog-bones that were used during the experiment.

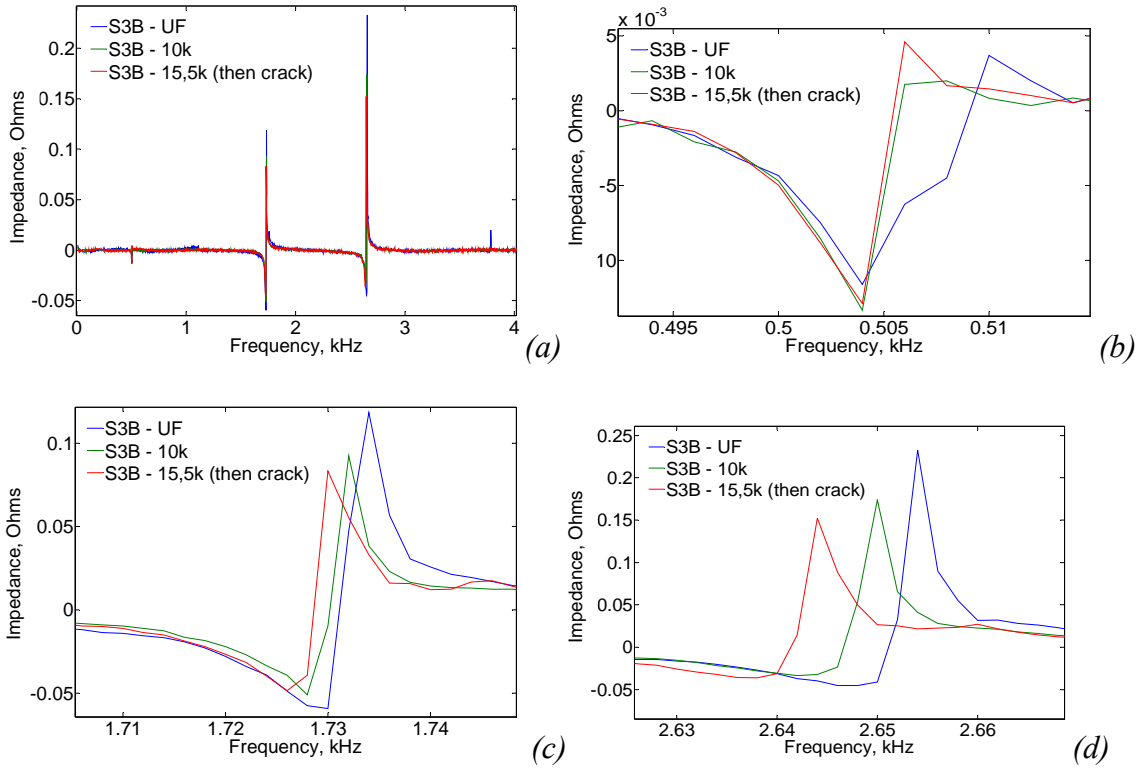


Figure 48 Magneto-mechanical impedance of the S3B sample (a) with selected zoom-in peaks (b,c,d)

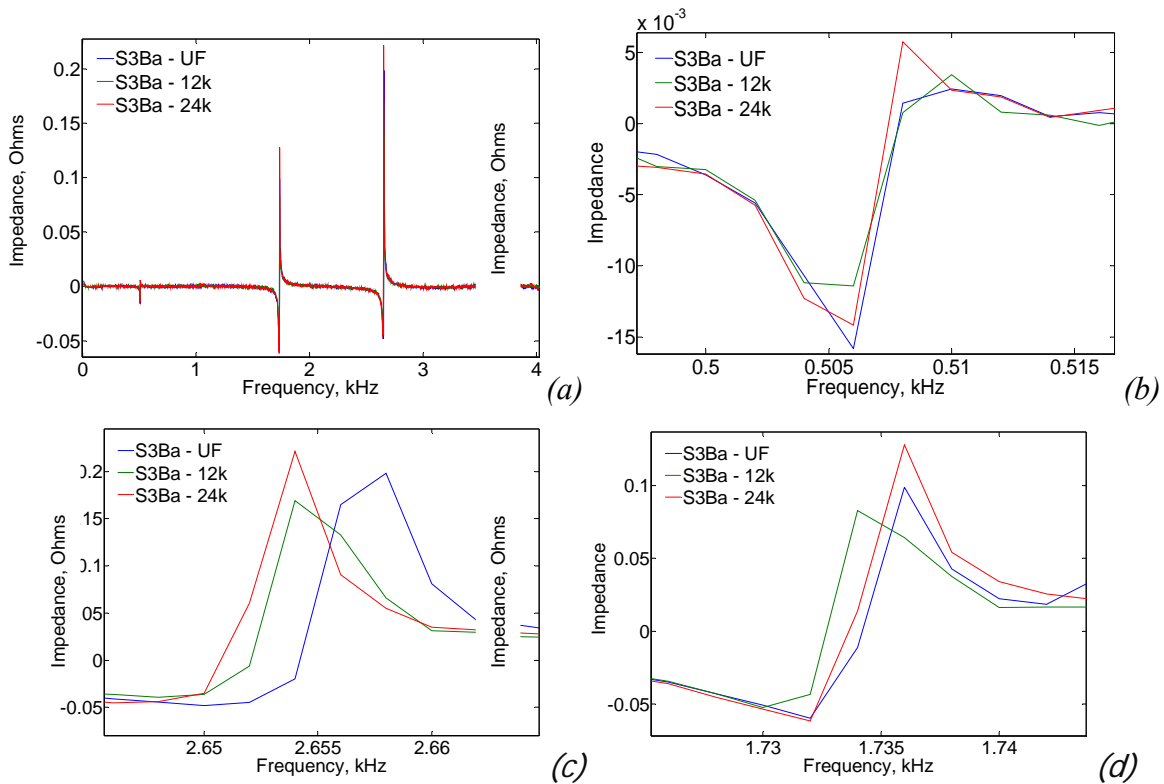


Figure 49 Magneto-mechanical impedance of the S3Ba sample (a) with selected zoom-in peaks (b,c,d)

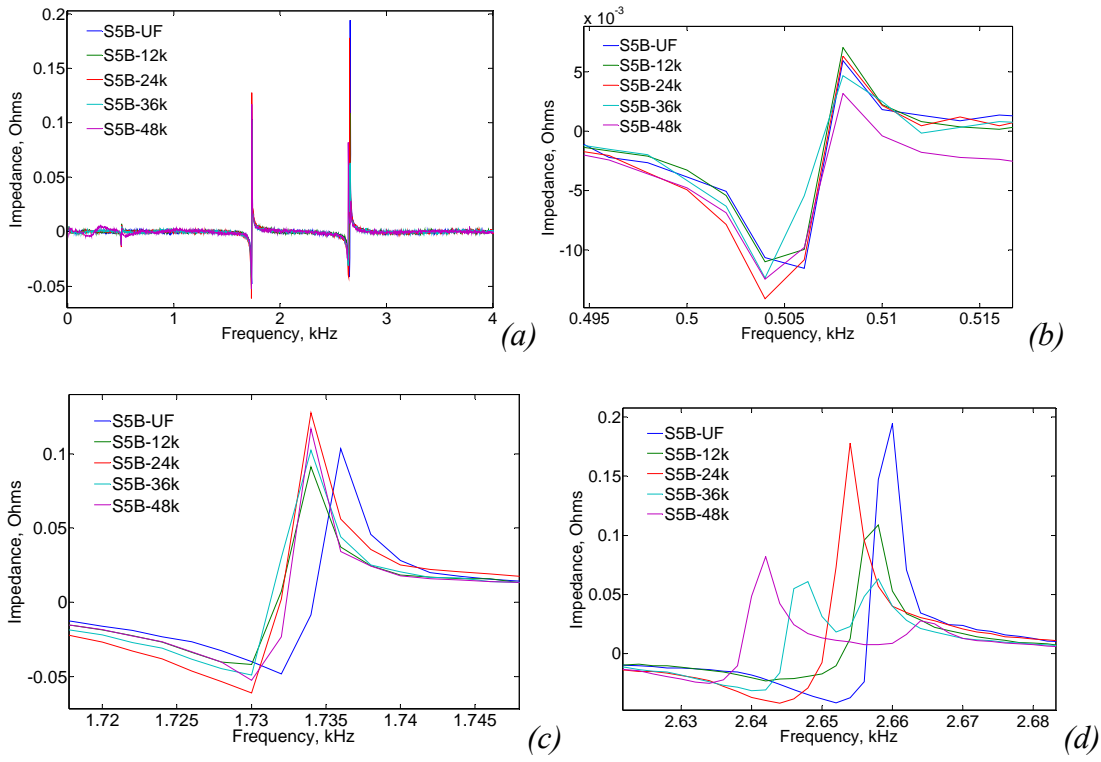


Figure 50 Magneto-mechanical impedance of the S5B sample (a) with selected zoom-in peaks (b,c,d)

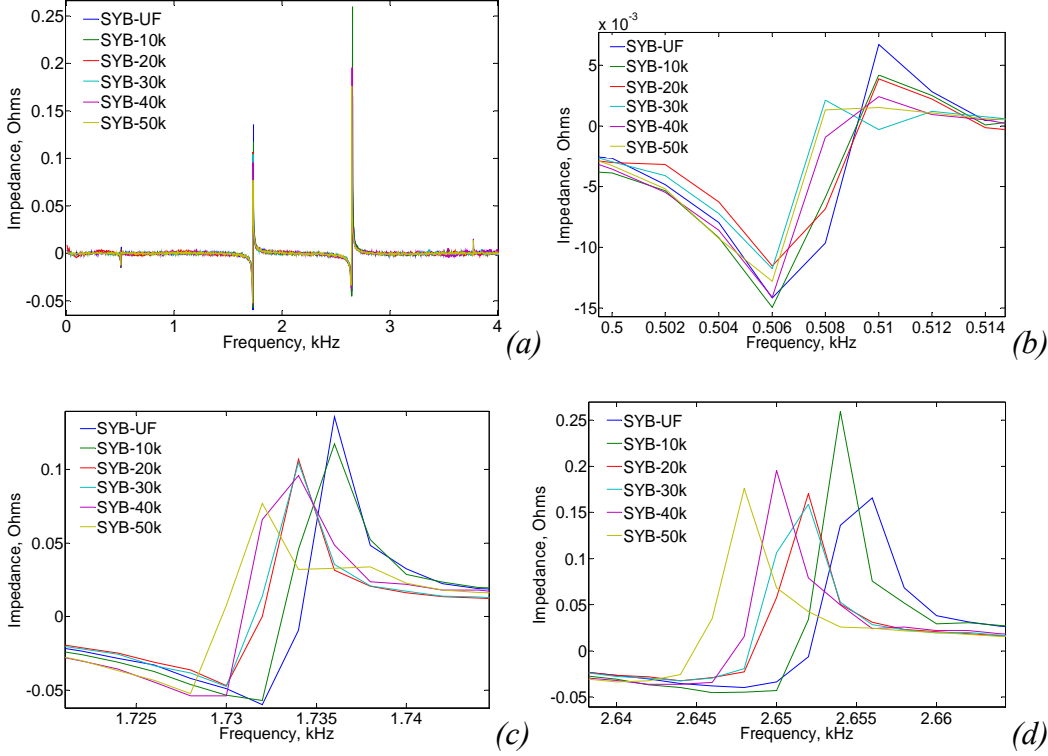


Figure 51 Magneto-mechanical impedance of the SYB sample (a) with selected zoom-in peaks (b,c,d)

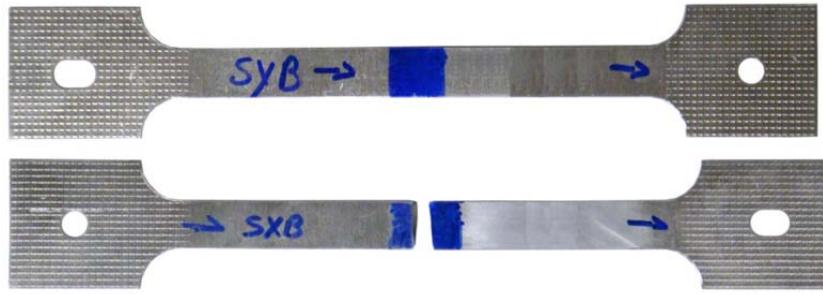


Figure 52 SYB and broken SXB Dog-bone specimens.

Figure 51 displays MMI signatures for the SYB Dog-bone specimen. Lower fatigue load (1.0104 kN) and stress level (100 MPa) has been carried out during the test. The sample was fatigued to 50,000 , but no crack development was observed. Very clear manifestation of the fatigue damage in this sample was observed, especially at the highest frequency.

After the analyzing the MMI data of fatigued specimens, it became apparent that most of the experimental specimen shows decreasing of the impedance peak frequency as the sample degraded under fatigue load. High frequencies in the MMI spectra produce larger change in the frequency value than the low frequencies. This was anticipated as higher frequencies produce shorter wavelengths in the material and are more affected by inhomogeneities.

Specimens S3Ba, S2Ba, SYB and S5B were fatigued under lower load conditions and did not show any sign of fatigue crack. Changes of impedance frequencies due to fatigue were less obvious for these samples. At rather low frequencies, detection of fatigue damage is not stable, but it is improved substantially at high frequencies. One of the most important results of this study is confirmation that MMI is able to detect fatigue damage before and after crack development. In the former case, the detection is far in advance of crack initiation and growth, which can be used for early damage detection and remaining fatigue life prediction.

2.2.4.3. MMI assessment of complex structure

An aluminum honeycomb panel was considered as an example of complex structure in MMI SHM. The panel consisted of two 1 ft by 1 ft aluminum sheets glued to aluminum foil honeycomb structure. Top and bottom portions of the plates were painted with a thin layer of white paint. A delamination of the top aluminum sheet from the honeycomb structure was introduced on one side of the panel. An approximate delamination area is 6 cm^2 . A side view of the panel is presented in Figure 53a. In all experiments, the panel was placed on foam to imitate free-free boundary conditions. MEAS was positioned underneath the panel in location indicated in in Figure 53b. Measurements were taken on top and bottom sides of the panel. MMI data were collected with HP4192A impedance analyzer, digitized and de-trended to eliminate inductive component of the impedance. The curves were then processed with 5 point moving average window to reduce measurement noise. Figure 54 illustrated MMI signatures of indicated points on a front side of the panel. Point 3 is above the delaminated area and its MMI exhibits pronounced difference in impedance peak amplitude and position when compared to other points on a front side. Moreover, in contrast to MMI signatures of other points, a peak at 3.5 kHz does not appear on the MMI curve of point 3. This response clearly allows for distinguishing intact and damaged conditions of the panel. Interestingly, response of point 3 on the bottom side of the panel is also very distinct from responses of other points and can be used for damage detection. Points located rather close to panel's center on both sides of the panel exhibit lower amplitude of the MMI response due to vibration constraints. It should be noted that response of the damage area (point 3) is distinctly different from responses of other symmetric points located near edges of the panel and of points located close to panel's center. This confirms feasibility of MMI- enabled damage detection in honeycomb panel.

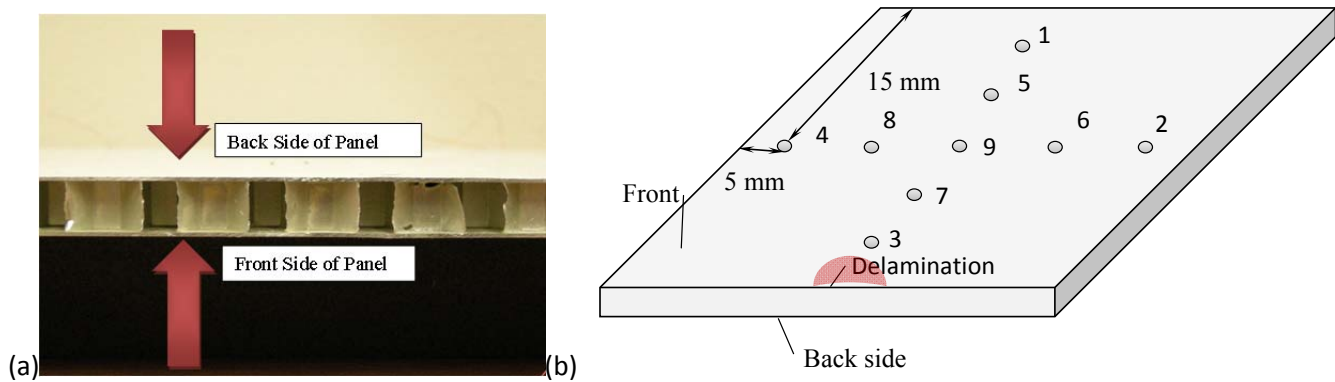


Figure 53 Side view of aluminum honeycomb panel (a) and MEAS locations in associated experiments (b).

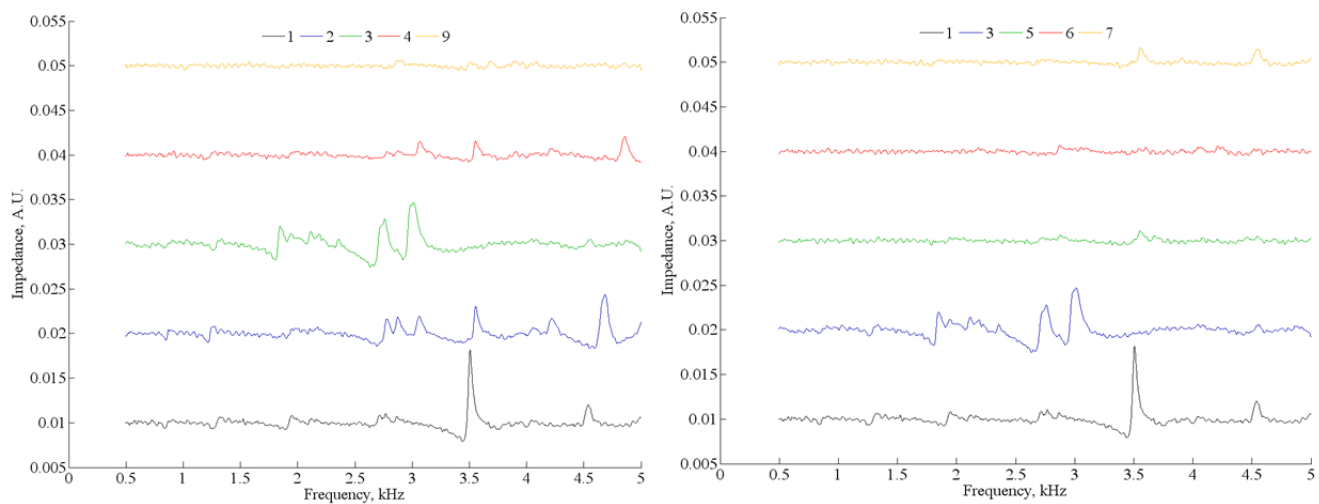


Figure 54 Impedance signatures collected at indicated locations on a front side of the honeycomb panel.

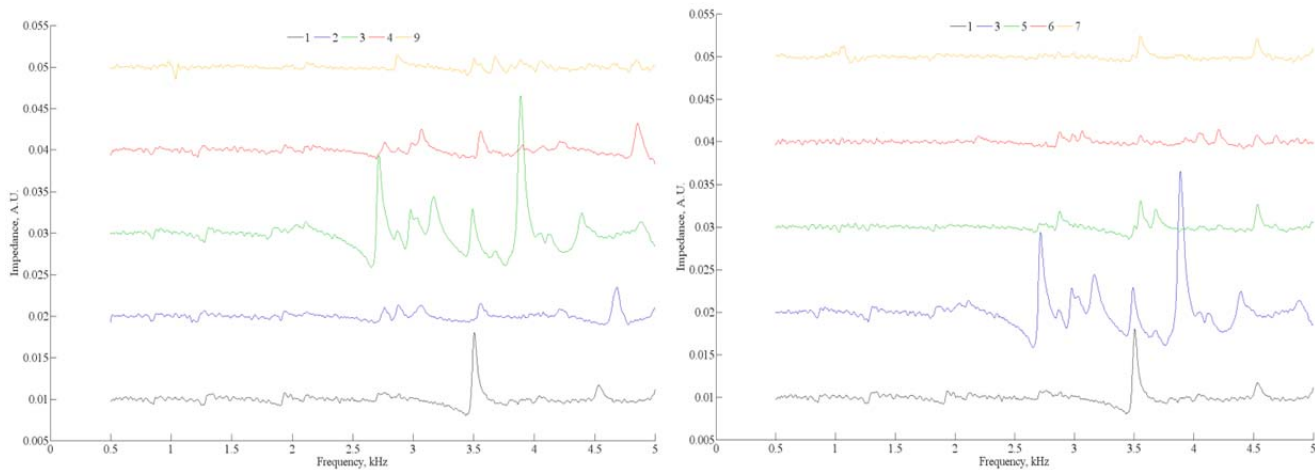


Figure 55 Impedance signatures collected at indicated locations on a back side of the honeycomb panel.

2.3 MEAS Modeling

2.3.1 Finite Element Model using COMSOL

In the preceding section of this report, an analytical model for MEAS and MMI was presented. The main limitation of the model is that it models MEAS through a transformer without explicit consideration of sensor lift-off (achieved through a coupling factor) and complex (radial and vertical) distribution of eddy currents. In addition, effect of the coil was introduced using electrical characteristics, rather than coil material, number of turns, wire diameter, etc. To address deficiencies of the analytical model, as part of this study, a number of numerical models were developed.

Comsol Multiphysics allows to solve numerically multi-dimensional problems in magnetostatics and vibration using the finite element Galerkin method. AC/DC and Structural Mechanics modules of Comsol Multiphysics package were utilized to model MEAS. The multiphysics capability of Comsol can be used to couple the electromagnetic model of a MEAS with the vibration model. The coupling of the two parts of the model can be accomplished in two ways: by a one way and a two-way couplings. The one-way coupling is created through the Lorentz force induced by the electromagnetic field of a MEAS and taken as the external load in the mechanical model. The two-way coupling is set by the electromagnetic field generated by eddy currents on the surface of the vibrating plate. Since the electromagnetic field of a MEAS is influenced by that of the vibrating mechanical structure, the readings of the electromagnetic parameters on terminals of a MEAS should reflect changes in elastic properties of the vibrating structure.

A two-dimensional (three dimensional with axial symmetry) model of MEAS is described by the Maxwell's equations in the frequency domain. Let A be the magnetic vector potential that satisfies the additional uniqueness condition $\nabla \cdot A = 0$. Since the magnetic flux density is $B = \nabla \times A$, Gauss's law is satisfied identically. The Ampere's law for a heterogeneous medium takes the form

participation factor is

$$\nabla \times \left(\frac{1}{\mu} \nabla A \right) = -J. \quad (26)$$

We assume the Ohm's law

$$J = \sigma E. \quad (27)$$

where σ is the electrical conductivity. The total force on a charged particle in a static electromagnetic field is the Lorentz force

$$F_L = qE + q \mathbf{v} \times \mathbf{B}, \quad (28)$$

which is the sum of the electric and the magnetic forces. The magnetic field of a permanent magnet is described by the equation

$$\mathbf{B} = \mu \mathbf{H} + \mu_0 \mathbf{I}_0, \quad (29)$$

where \mathbf{I}_0 is the magnetization field of the magnet.

Structural model considers flexural vibrations, which in 2-D are governed by the following equation

$$D \nabla^4 w(x, y, t) + \rho h \cdot \frac{\partial^2 w(x, y, t)}{\partial t^2} = q(x, y, t). \quad (30)$$

where w is the deflection of the middle plane of the plate, q is the external transverse load, h and ρ are the plate thickness and density, respectively, $D = Eh^3/12(1 - \nu^2)$ is the flexural rigidity, and E and ν are the Young's modulus and Poisson's coefficient. The equation is solved for a specific boundary condition (e.g. clamber, free, etc.). A beam equation is utilized for 1-D structures.

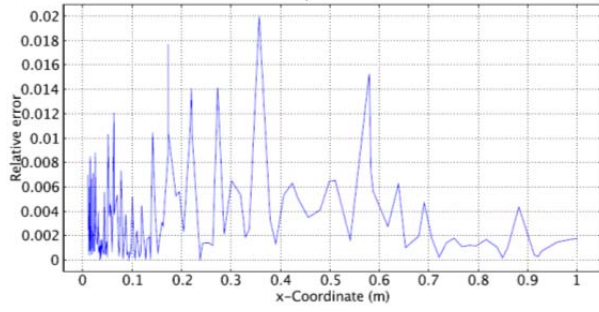


Figure 56 Infinite wire: the relative error of the numerical solution for the magnetic induction along the x-axis.

The MEAS model is coupled with the thin vibrating plate model through the external load force. The axial component of the Lorentz force in the MEAS model is extruded on the circular disk domain of the vibration problem and is used as the external transverse load force.

The modeling approach was first validated though a series of elementary models such as induction of infinite straight wire and magnetic induction of a circular wire loop. Using these models, relative errors of numerical solution were evaluated and results were compared to known analytical solutions. Examples of the model validation efforts are presented in Figure 56 and Figure 57.

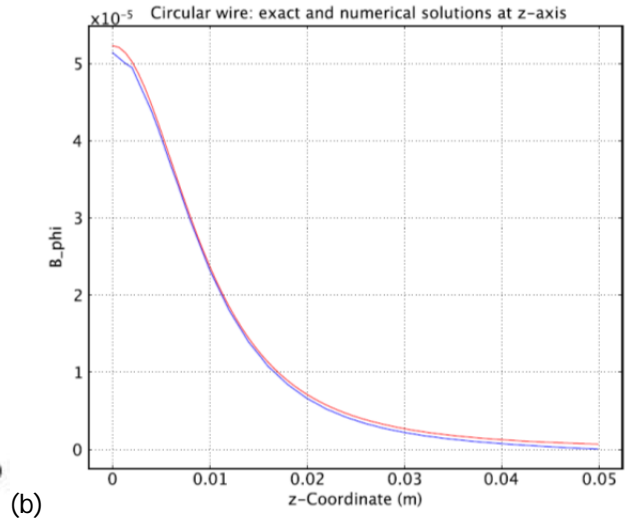
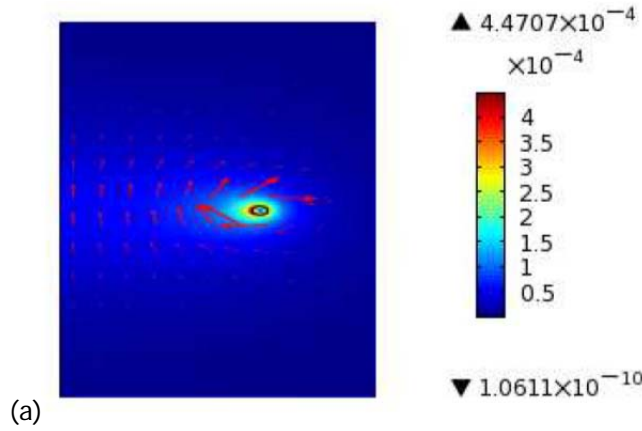


Figure 57 Circular wire: (a) the numerical solution for the magnetic induction field; (b) the exact (red) and the numerical (blue) solutions on z-axis.

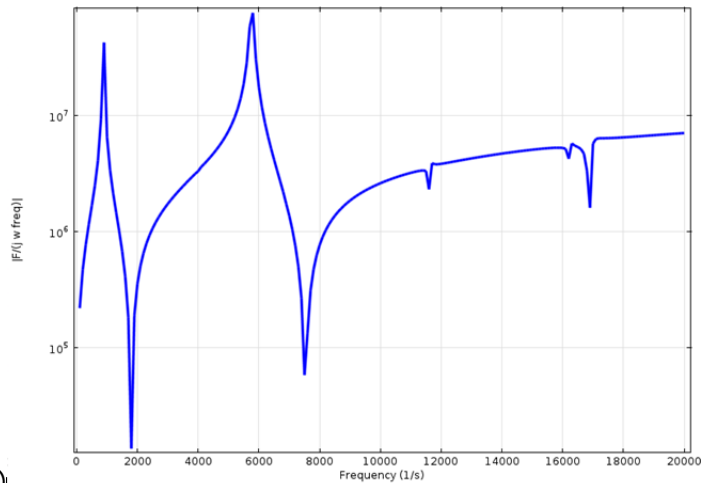
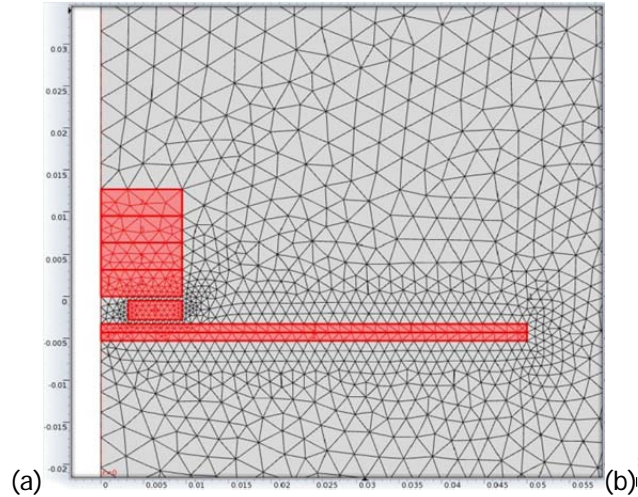


Figure 58 (a) FE mesh of 2-D axisymmetric MMI model; (b) example of calculated magneto-mechanical impedance.

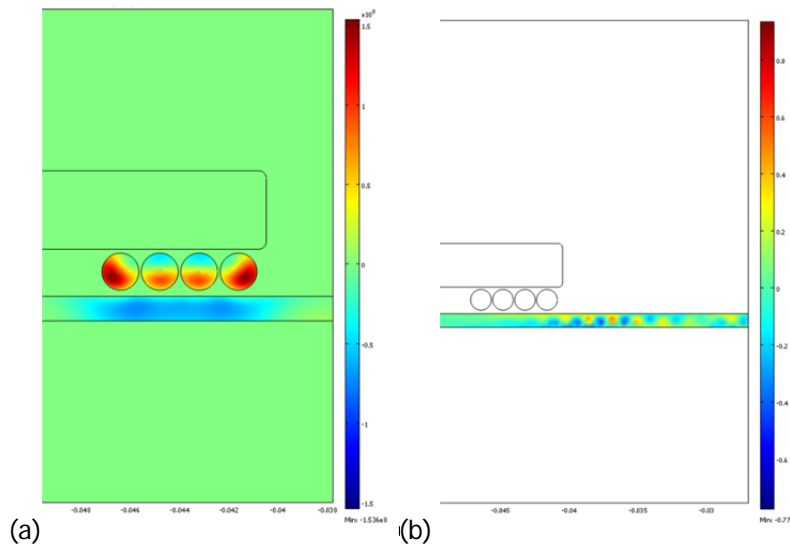


Figure 59 (a) Surface plot of current density in vicinity of MEAS. (b) Plot of particle velocity within the plate under the transmitting MEAS showing propagating Lamb wave.

2.3.2 Point-source Heuristic Model of MEAS

Insomuch as the utility of the COMSOL MEAS models was constrained by limited computational resources, alternative modeling solutions for MEAS signal prediction were also investigated. This led to the development of so called “heuristic model” of MEAS transduction, which involved some idealized assumption with regard to the transduction mechanism. Specifically, the assumptions were as follows:

1. The eddy current distribution in a conductive host structure is a perfect mirror image of the current flow in the excitation coil.
2. The Lorentz-Force transduction mechanism faithfully reproduces the waveform of the excitation signal as an elastic wave.
3. Each point where an eddy current intersects a magnetic field line can be treated as a point source of elastic waves.
4. Propagation of a tone burst signal as an elastic wave over a distance can be approximated by shifting the signal in time by an amount equal to the distance divided by the nominal group velocity of the wave-mode in question, calculated at the nominal frequency of the tone burst.
5. The elastic wave present at a given point in the host structure is the sum of the waves from all the point sources.
6. MEAS reception is the exact inverse of MEAS transmission.

The system was further idealized as one-dimensional, and a MatLab function was written to calculate the signal that would be received from transducer C2, when it was placed 18.75 inches from C1 on a 0.041-inch-thick aluminum plate, and C1 was excited with a tone burst. The MatLab function, authored by Timothy Barnes, is available in his MS thesis. To some extent, this model can be viewed, as a variant of point source models described by Placko and Kundu (2007).

The total impedance was calculated as a ratio of the Lorentz force to vibration velocity, which for harmonic motion was estimated as structural displacement multiplied by $j\omega$. An example of the resultant curve is given in Figure 58. Examples for other structures (such as a beam), parametric studies, and a wave propagation model (Figure 59) can be found in theses by David Kukhalashvili and Timothy Barnes.

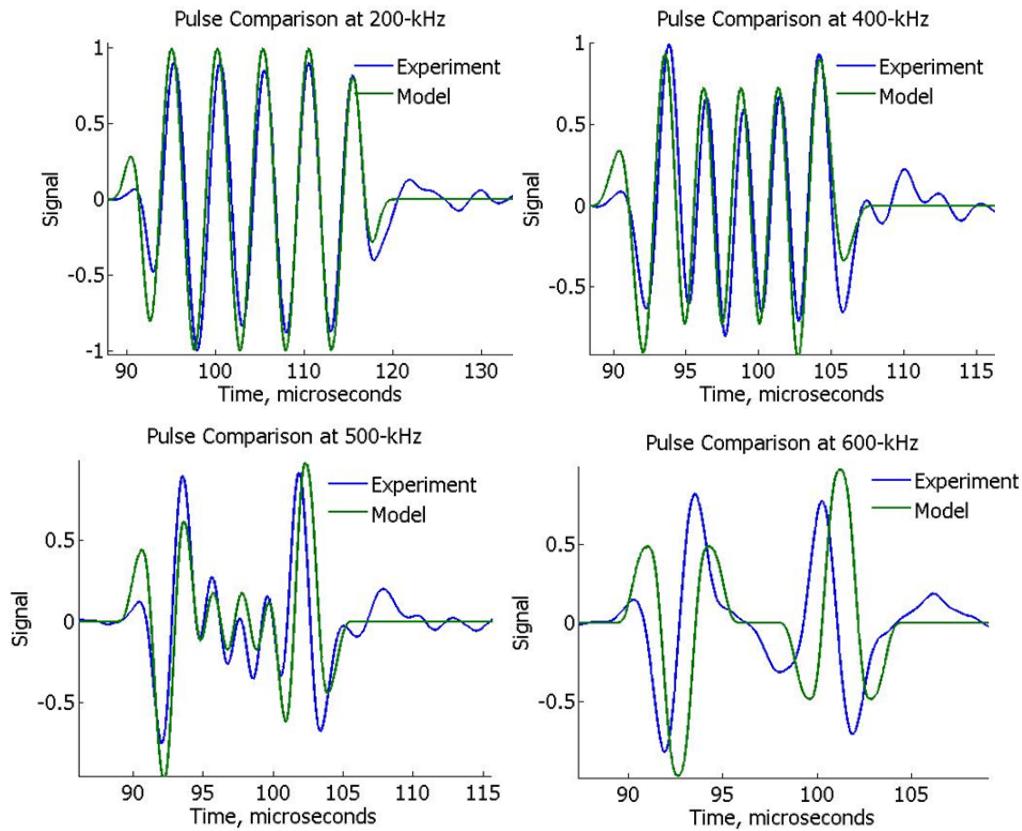


Figure 60 Comparison of measured and modeled MEAS signals at various frequencies, taking effective excitation diameter into account.

Using this approach, a series of signals at various excitation frequencies were modeled and plotted against signal obtained experimentally. Because the model does not include a method for predicting absolute transduction efficiency, the relative amplitude of the experimental and theoretical pulses was normalized to expedite comparison. Interestingly, it was found that rather than using actual coil diameter in the model, an effective coil diameter equal to 1.376 of actual coil diameter should be used. This correction is necessary to account for non-uniform distribution of the excitation force which peaks not at the actual coil diameter. Plots comparing the predicted (with coil diameter correction) and actual pulses at 200, 400, 500, and 600 kHz are shown in Figure 60. It may be observed that at low frequencies (~ 200 kHz), the signal takes the form of a sinusoidal burst of relatively uniform amplitude, and the model very closely matches the actual received signal. As the frequency of excitation is increased, the pulse first becomes concave in its envelope, while remaining sinusoidal, as seen at 400 kHz, and then loses all semblance of a sinusoidal pulse, becoming only a distorted double-peak, as can be seen at 500 kHz and 600 kHz.

The model seems to show a small phase shift with respect to the experimental data. However, all features of the experimental data including concaving of the pulse and degeneration into a double peak signal at higher frequencies are predicted correctly. Therefore, while the heuristic model obviously has its own limitations, it does seem to provide a reasonably accurate approximation of MEAS behavior.

2.4 MEAS application in Wave Propagation SHM

2.4.1 Far-Field Crack Detection

One of the first investigated applications of MEAS was the detection of cracks in thin plates by pitch-catch ultrasonics. The principle behind this technique is well-known: if a defect, such as a crack, lies on the wave propagation path between the transmitting sensor and the receiving sensor, the defect will tend to deflect some of the energy of the propagating wave, affecting the amplitude of the received signal. To demonstrate the pitch-catch technique using MEAS, two sensor placement patterns of the form illustrated in Figure 61 were laid out on opposite corners of a 0.041" thick, 3 ft square 2024-T3 aluminum plate. The pattern on one corner incorporated a simulated crack at the location of the dark line in the figure, while the other did not. The simulated crack consisted of a machined slot, 0.610" (15 mm) long by 0.023" (0.6 mm) wide. In each case, the sensors were positioned equidistant from the crack with the transmitter on one side and the receiver on the other. The total sensor separation for the various positions is tabulated in Table 9. Sensors E1 and E2 were employed in this experiment.

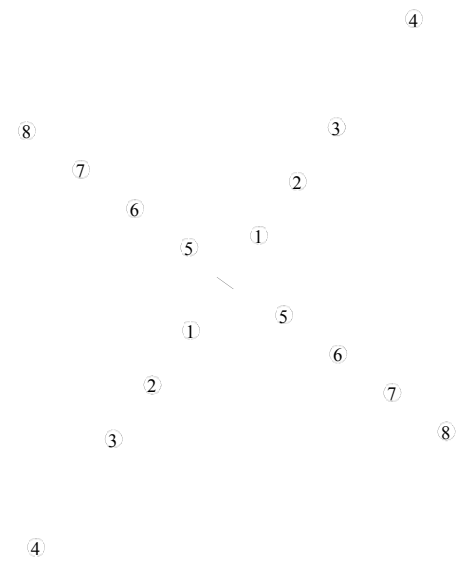


Figure 61 Sensor pair positions for pitch-catch crack detection experiment.

Position	Sensor Separation
1	4 inches (~10 cm)
2	8 inches (~20 cm)
3	12 inches (~30 cm)
4	20 inches (~50 cm)
5	4 inches (~10 cm)
6	8 inches (~20 cm)
7	12 inches (~30 cm)
8	16 inches (~40 cm)

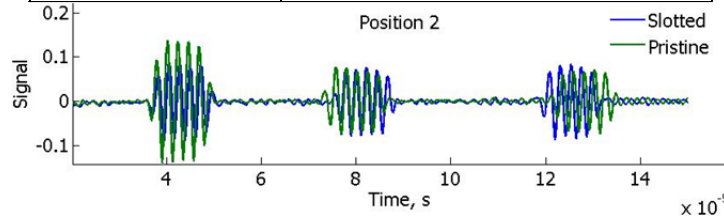


Figure 62 Typical signal through crack. First pulse is S_0 ; second and third are echoes.

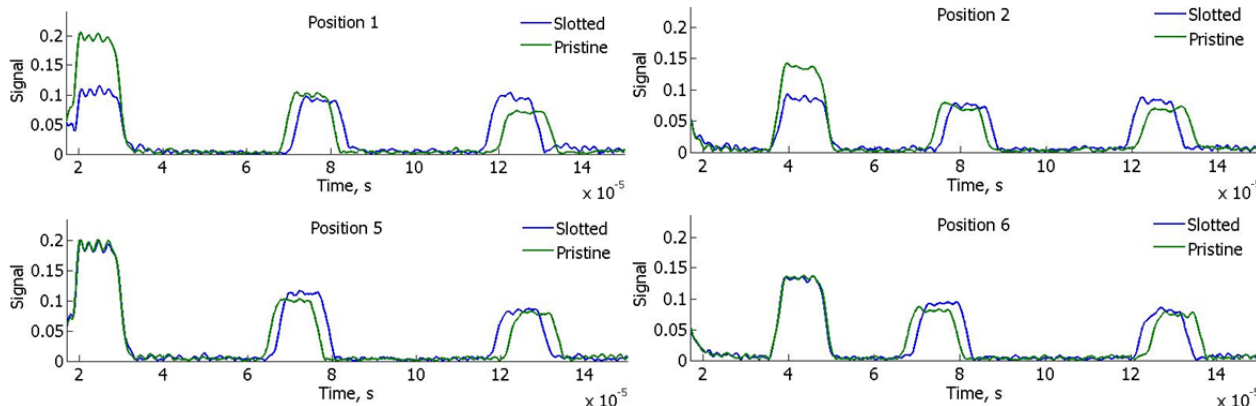


Figure 63 Envelope of signal transmitted through crack for various positions of MEAS pair.

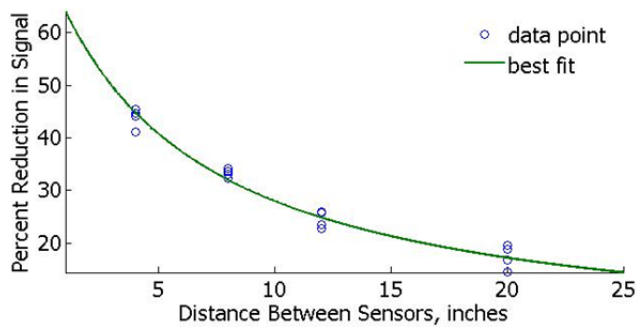


Figure 64 Effect of distance on signal amplitude reduction caused by a crack on the wave

this effect decreases with increasing distance of the sensors from the crack. A plot of the percent of amplitude reduction as a function of distance is shown in Figure 64.

When the direction of propagation is parallel to the crack, no appreciable change in amplitude is observed. In both cases, the amplitude of the echo pulses are largely unaffected, though the echoes are slightly different for the cracked and pristine conditions, due to slight differences in the placement of the two sensor patterns relative to the edges of the plate.

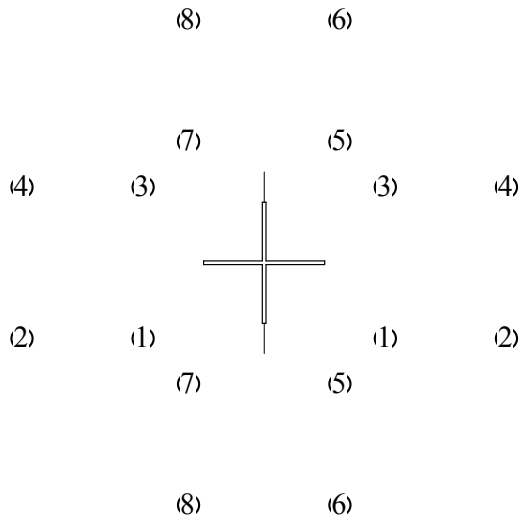


Figure 65 Position of sensor pairs for far-field crack detection on fatigued plate.

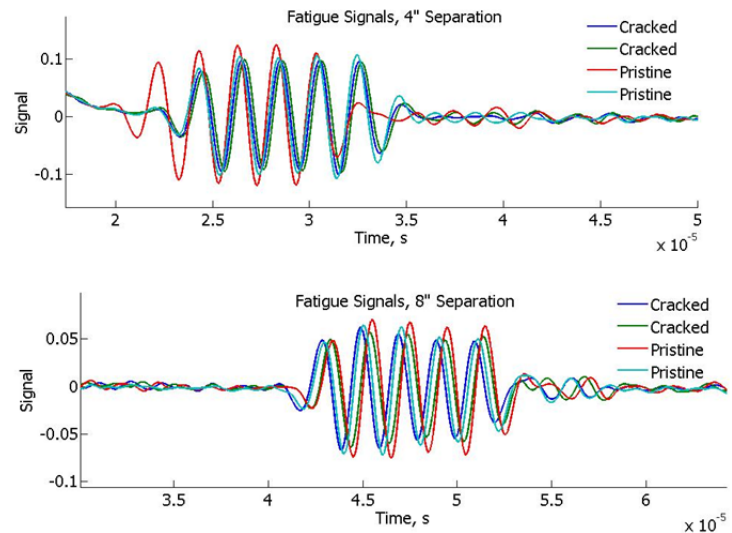


Figure 66 Comparison of recorded pulses for sensor pairs with 4" and 8" separation on fatigued plate.

After obtaining the above results for a plate with a simulated crack, verification of the technique was attempted on an aluminum plate containing actual fatigue cracks. The sensors were positioned on the plate as shown in Figure 65. Two crossing perpendicular slots had been machined at the center of the plate, providing a stress concentration to control the initiation site of fatigue cracks when the plate was subjected to cyclic loading. Due to the direction of loading, cracks initiated and grew from the two ends of one slot, but not of the other. This permitted two independent records of both the cracked and pristine conditions to be obtained with a given degree of sensor separation. The signals recorded for transmission between each of the respective sensor pairs are shown in Figure 66.

As can be seen in Figure 66, the amplitude reduction for the cracked versus pristine conditions is minimal. At a separation of 4 inches, the amplitude of the pulses that propagated through fatigue cracks is consistently less than that of those that did not, even though the magnitude of the difference is very small. When the sensor separation is increased to 8 inches, this trend is no longer visible, perhaps

because the magnitude of the difference has fallen below the threshold of random amplitude fluctuations. It may thus be concluded that while actual fatigue cracks have the same general affect on propagating signals as machined slots, that is, while both tend to cause a distance-dependent reduction of signal amplitude, the magnitude of the effect is noticeably less for actual fatigue cracks than for machined slots.

2.4.2 Near-Field Crack Detection

Because MEAS generate ultrasound by means of Lorentz Forces on induced eddy currents, anything that affects the ability of a structure to support eddy currents should also affect MEAS transduction. This provides an alternate method of near-field damage detection using MEAS: any damage that obstructs the flow of eddy currents under a MEAS should cause a reduction in the amplitude of the elastic waves generated by that sensor. To explore the viability of this method, two sensors were positioned on a large aluminum plate with a simulated crack, as shown in Figure 67. The plate was three feet square by 0.041 inches thick, and simulated crack consisted of a machined slot 0.610" (15 mm) long by 0.023" (0.6 mm) wide. Distances from the right endpoint of the simulated crack to the leftmost point on the circumference of the transducer for the five positions at which data was taken are given in Table 10. In the table, a negative distance indicates the sensor is partially covering the crack, while a positive distance indicates that it is not. Waveforms of the resulting signals are shown in Figure 68, and the corresponding signal envelopes are shown in the same figure.

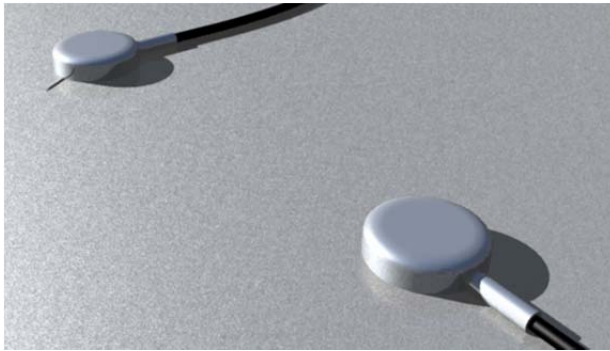


Table 10: Sensor Positions for Near-Field Experiment.	
Sensor Position	Distance
"Off Crack"	+0.500 inches
"Near Crack"	0.000 inches
"1/4 On Crack"	-0.090 inches
"1/2 On Crack"	-0.250 inches
"On Crack"	-0.550 inches

Figure 67 Illustration of sensor placement for near-field crack detection experiment.

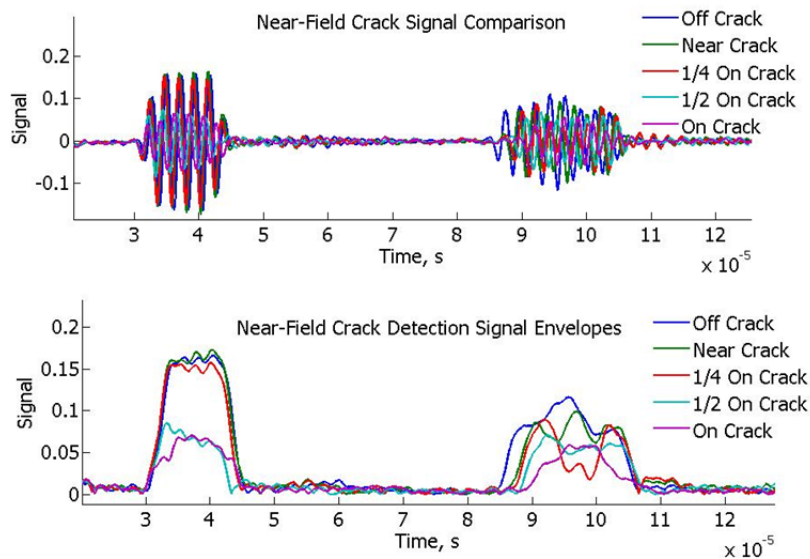


Figure 68 Waveforms and signal envelopes obtained in near-field crack detection experiment.

Based on measurement results presented in the figure above, there is clearly a decrease in signal amplitude when a defect is underneath the transmitting sensor. However, the magnitude of the effect does not become noticeable until the defect extends far enough under the sensor to appreciably inhibit the flow of eddy currents, and the signal level appears to drop off sharply as this point is reached.

2.4.3 Detection of Disbonds in Honeycomb Panels

As honeycomb panels are commonly used in construction of aerospace structures, detection of disbonds in such panels is a problem of interest in SHM. This problem is perhaps particularly amenable to the use of MEAS, because commercial honeycomb panels are usually painted, and the non-contact coupling mechanism of MEAS allows them be used without regard to the paint, whereas PWAS would require removal of the paint for mounting of the sensor. A photograph of a typical honeycomb panel is shown in Figure 69.

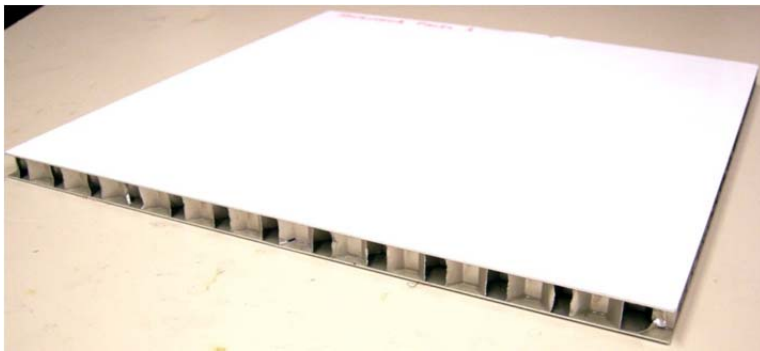


Figure 69 A typical aluminum honeycomb panel.

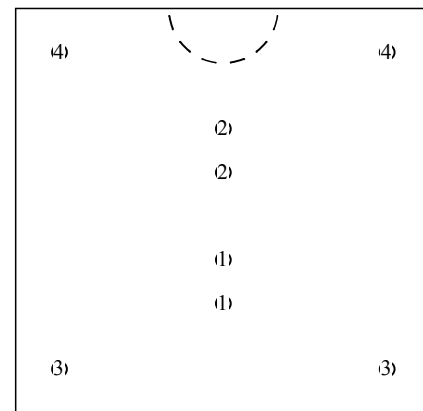


Figure 70 Diagram of disbond and sensor locations on honeycomb panel.

To explore the utility of the prototype MEAS for detection of disbonds in honeycomb panels, a roughly semi-circular disbond was induced in a honeycomb panel by prying a portion of the panel off the honeycomb structure to which it had been bonded, and MEAS were used to transmit and receive signals on the panel at the locations shown in Figure 70. In positions 1 and two, the signal was transmitted by the transmitting transducer and reflected off the perpendicular side of the panel back to the receiving transducer. In the case of position 2, the echo would pass through the disbond, while in the case of position 1 it would not. Thus, for the perpendicular echoes, position 1 represents the pristine condition, while 2 represents the disbonded condition. In positions 3 and 4, the signal was transmitted parallel to the side of the plate along a side either containing the disbond, as in 4, or containing no defects, as in 3. Thus, for the thru-transmitted signals, position 3 represents the pristine condition, and position 4 represents the disbonded condition. The received signals are shown in Figure 71 and Figure 72.

When the perpendicular echo signals of Figure 72 are examined, there appears to be very little difference between the pristine and disbonded conditions. However, when the signals transmitted parallel to the sides of the plate are considered, a significant increase in signal amplitude is observed for the disbonded case. Based on integration of the Hilbert signal envelope over a time interval from 40 to 100 microseconds, it may be calculated that the presence of the disbond increases the amplitude of the received signal by 62 percent.

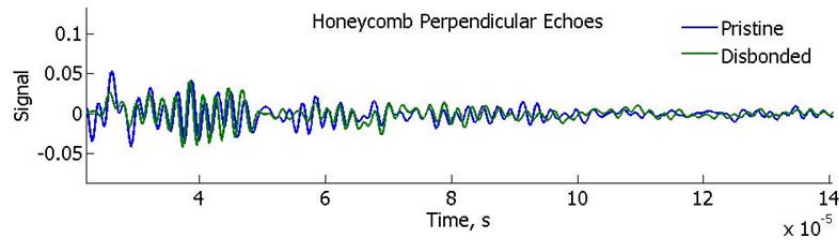


Figure 71 Signals from honeycomb panel experiment transmitted perpendicular to plate edges and reflected back to receiver.

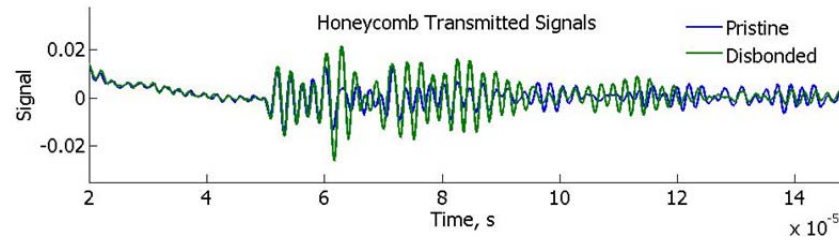


Figure 72 Signals from honeycomb panel experiment transmitted parallel to the plate edges.

This result agrees well with expectations that the disbond would prevent acoustic waves from flowing into the honeycomb structure, or through it to the opposite side of the panel, and would thereby tend to concentrate acoustic energy in the top plate. Why this effect would be pronounced for the thru-transmitted signals but not for the reflected signals is more enigmatic. It may be that the disbond did not extend as far into the interior of the panel as was supposed, having been induced by a deliberate overload at the edge of the plate. If the disbond actually occurred only in a narrow region near the edge of the plate, then the transmitted signals would have propagated through the disbond for a much greater distance than the reflected signals, producing the observed result.

2.5 Nonlinear SHM with MEAS

2.5.1 Acousto-elastic Assessment of Bolted Joints in Elastic Plates

Acousto-elasticity is a nonlinear effect of dependence of the sound speed on applied mechanical stress (Norris, 1997). This team has developed an acousto-elastic damage detection technique based on amplitude and phase measurements of the elastic wave propagating through a bolted joint (Doyle et al., 2009). The technique allows not only to detect a loose bolt in a complex joint, but also estimate its location. Prior work on this SHM method involved piezoelectric wafer active sensors and, in this study, was extended to MEAS.

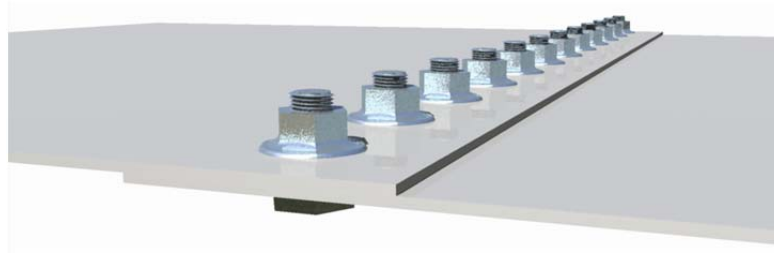


Figure 73 Illustration of bolted joint.

A series of experiments has been conducted in which magneto-elastic active sensors were employed for assessment of the bolted joint. Two aluminum plates were bolted together, as shown in Figure 73. In total, the joint incorporated twelve 3/8NC bolts, which were placed at 2-inch intervals across the breadth of the two plates. Two MEAS were placed on opposite sides of the joint near the row of bolts and at the equal distances from edges of the plate. A short pulse of the elastic wave was propagated from a transmitting MEAS to the receiving MEAS and elastic waves were collected for different conditions on a central bolt. Initially, all bolts in the joint were in “tight” condition estimated to yield about 50 ft-lbf. Then, the bolt was loosened to establish “finger tight” condition, tightened to 25 ft-lbf and further tightened to original “tight” condition of 50 ft-lbf. Records of elastic waves corresponding to these conditions are presented at Figure 74. Noticeable in the figure, “tight” and “loose” (finger tight) conditions of the bolt are clearly distinguishable as well as an intermediate phase position of the signal corresponding to 25 ft-lbf. Remarkably, the signal almost returns to its original condition when a bolt is re-tightened to 50 ft-lbf suggesting that both “tight” cases match well. This experiment confirmed feasibility of acousto-elastic measurement using MEAS and its ability to detect loose bolts. However, it was also important to determine possibility to measure a particular torque on a bolt in the joint and a new set of experiment was conducted.

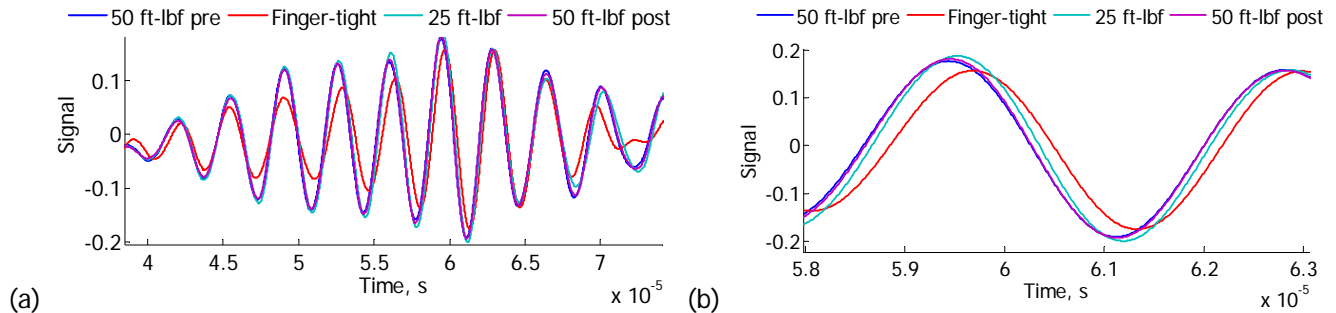


Figure 74 Signals transmitted through bolted joint at five conditions of the central bolt.

Following a procedure described above, two MEAS were placed on opposite sides of the joint, and a bolt near the center of the plate was loosened. This bolt was then re-tightened in steps, and transmitted signals were recorded for each step. The received signals and signal envelopes, respectively, are plotted in Figure 75 and Figure 76, which also features a best linear fit of the data.

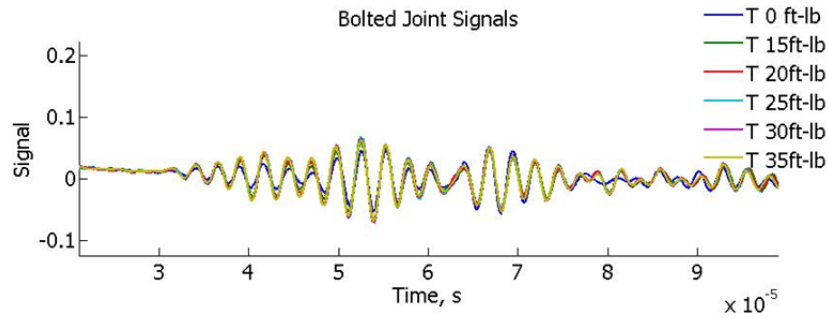


Figure 75 Signals transmitted through bolted joint at various torque levels.

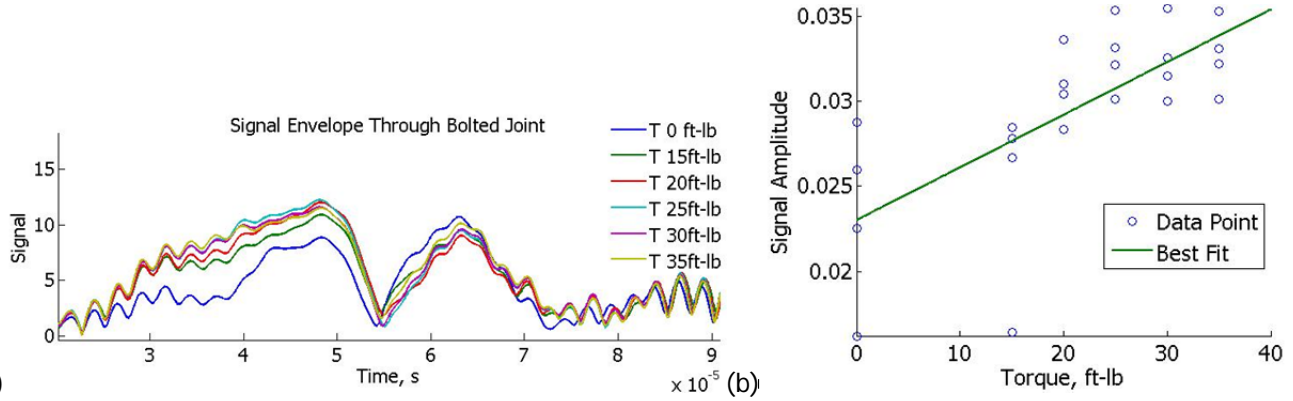


Figure 76 (a) Envelopes of signals transmitted through the bolted joint, (b) measured signal amplitude as a function of bolt torque.

From zero to about 25 foot pounds of torque, signal amplitude appears to increase linearly with torque. However, above 25 ft-lb, the actual data appears to level off. This threshold of linearity would tend to impose limits upon the utility of amplitude-based methods for measuring bolt torque. Nevertheless, the difference between fully-tight and fully-loose conditions should be substantial, so the method could certainly be used for binary detection of the loose condition, and within certain limits, even to provide an estimate of bolt torque.

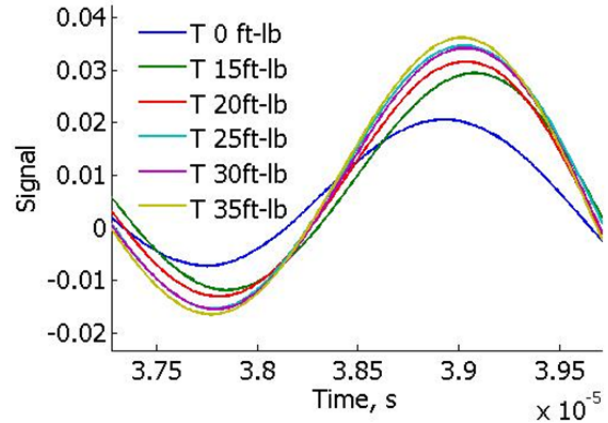


Figure 77 Zoomed-in view of a portion of the signal shown in Figure 75.

It was noted during analysis of the signals that, in addition to the reduction of signal amplitude associated with a loose bolt, there seems to be a torque-dependent phase shift of at least portions of the signal. An example of the shift can be seen in Figure 77. Sometimes, the phase shift increased with increasing torque on the bolt, but this dependence was not stable and, hence, is not recommended to be solely used for determining the torque level. Such instability was also confirmed in additional tests. Further details of this study are available in Timothy Barnes MS thesis.

It should be emphasized, however, that MEAS was effective in detecting a binary, i.e. “loose” vs. “tight” scenario and additional aspects such as MEAS position and range were investigated. For example, MEAS were considered in four tests investigating the effect of sensor distance from a “loose” bolted joint and contribution of structural features in a wave propagation signature. Figure 78 illustrates position of sensors with respect to bolted joint and the “loose” bolt shown in red. In the experiments, the “tight” condition was achieved by setting all bolts in the joint to 40 ft-lb torque. The “loose” condition was defined as a minimum torque to hold plates, i.e. several ft-lb. Both transmitting and receiving

MEAS were attached to plates using double-sided tape. Because the generation and reception of the elastic waves occurred inside the plate, contribution of sensor adhesive was not essential in this experiment. A transmitting MEAS was excited with a 5 count electrical pulse of high amplitude. The received signals were digitized and processed in Matlab[®]. The resultant records are illustrated in Figure 79.

Detection of a loose bolt from relatively far distance was studied in experiments 1 and 2. In experiment 1, a “loose” bolt was on a direct wave propagation path between transmitting and receiving MEAS. As it could be seen in Figure 79a, a phase shift in this case occurred at the very beginning of a signal and a whole pulse was noticeably shifted in time. Interestingly, the second pulse associated with reflections from the overlap portion of the plates (50 mm overlap), shows an even more pronounced phase shift. Apparently, this occurred because a larger portion of the signal was longer subjected to stresses exerted on the plates by a bolt. The direction of a phase shift in the second pulse is different possibly because of reflections in the overlapping section of the joint. Experiment 2 also shows a phase shift

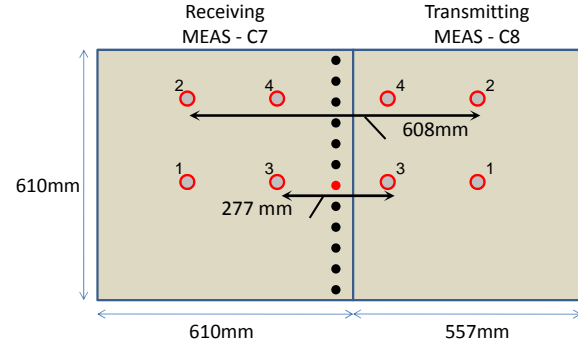


Figure 78 MEAS position on bolted plates in 4 experiments.

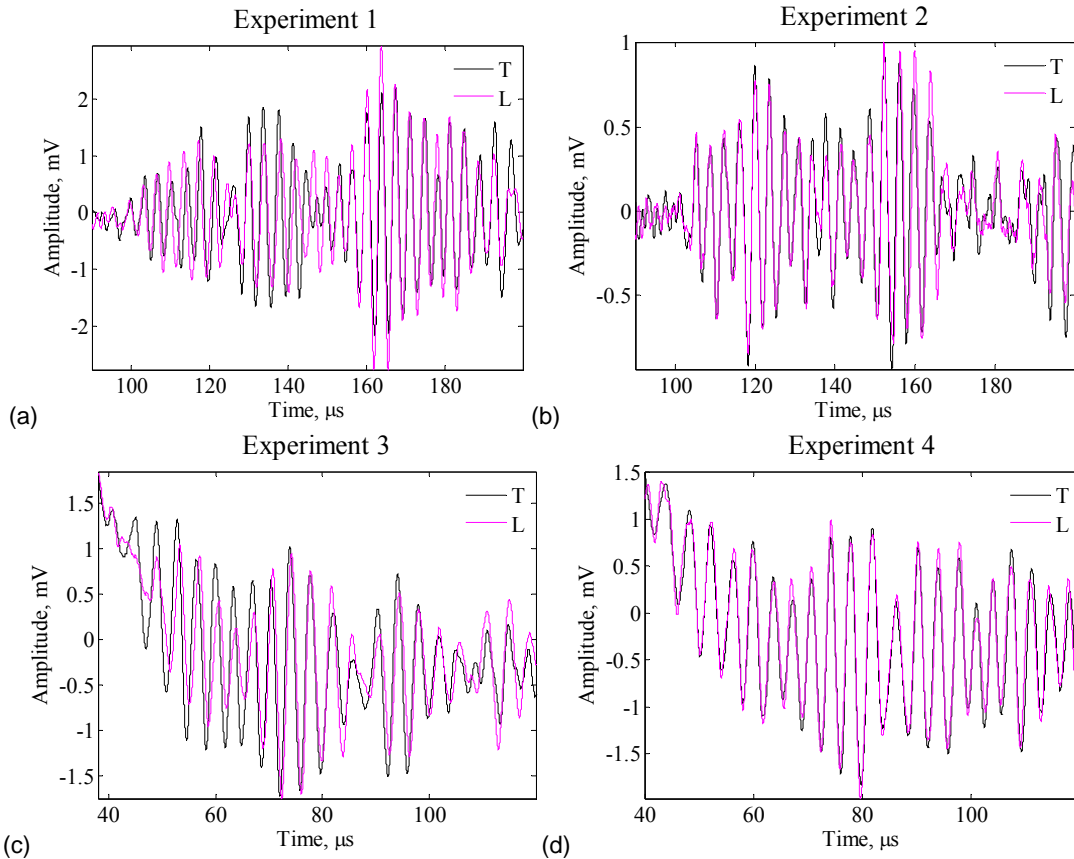


Figure 79 Signal records corresponding to “tight” and “loose” conditions of a bolt for experiments 1 (a), 2 (b), 3 (c) and 4 (d).

and amplitude change between the signals associated with “tight” and “loose” conditions of the bolt, but occurring much later in time. Experiments 3 and 4, conducted for sensors in close proximity of the joint, feature signals contaminated by a DC offset from electro-magnetic interference of the initial pulse. Still, signals in Figure 79c show phase and amplitude changes occurring immediately while Figure 79d

suggest changes at much later time at approximately $110\mu s$. Because of short propagation distance, directly transmitted and reflected (from joint) pulses overlap in Figure 79c.

2.5.2 Magneto-Mechanical Impedance Acousto-Elastic Assessment of Realistic Satellite Panel

In this study, the MMI technique was considered for nonlinear acousto-elastic damage detection in a specimen of complex geometry – a realistic satellite panel depicted in Figure 80. A contact operation mode, in which the MEAS was placed directly on the metallic structure, was adopted for all reported experiments. Due to the absence of the lift-off distance, the contact mode improved efficiency of the magneto-elastic transformation, which provided additional benefits because the satellite panel was thicker than the aforementioned thin-plate specimens. The satellite panel consists of a periodic iso-grid structure which, from a structural dynamics point of view, may exhibit common vibration features associated with each quadrant of the grid. Therefore, in this investigation, we focused on a single iso-grid quadrant located close to the center of the panel. This location was selected to eliminate possible contribution of the edge effects on the structural dynamic signature. Figure 81 illustrates the position of the MEAS in the center of the iso-grid quadrant.

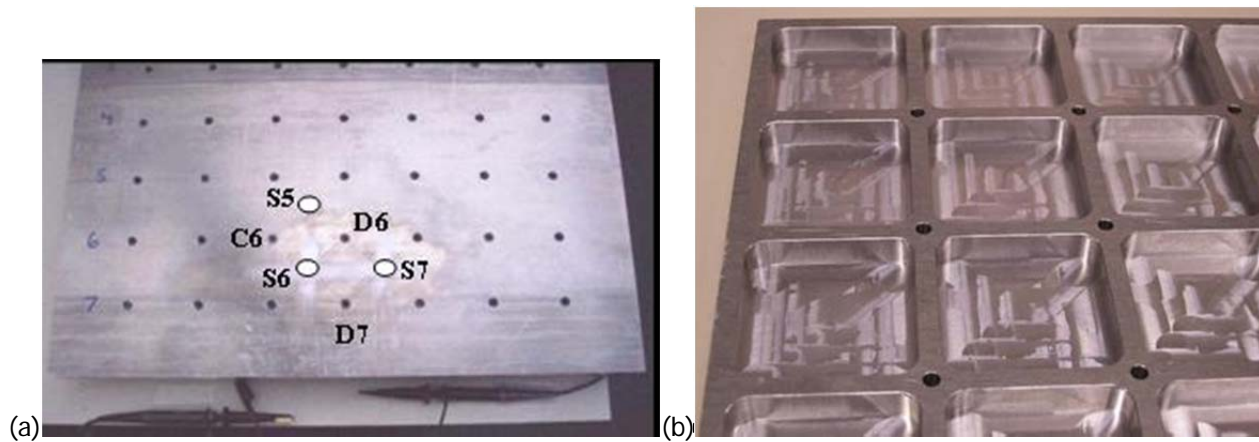


Figure 80 A realistic satellite panel consisting of two aluminum plates with iso-grid frames on the back side (a), (b) details of the iso-grid structure.

In practical satellite qualification tests it is important to distinguish between joints with fully tightened and loosened bolts. To determine variation of the magneto-mechanical impedance due to different stress conditions at corners of the iso-grid quadrant, two sets of tests were conducted. In the first set, all bolts were initially fully tightened and then incrementally loosened, while in the second set all bolts were initially loosened and then incrementally tightened. The location of both experiments was the same – quadrant DE 34 (see Figure 81).

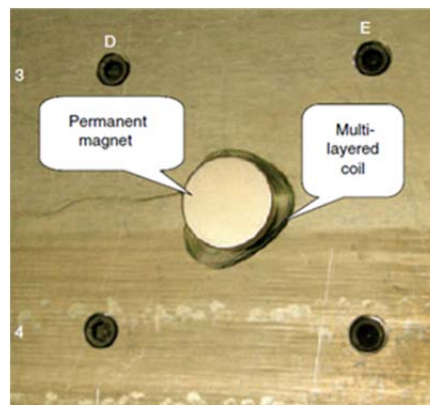


Figure 81 MEAS with a shielding cover and cable connection removed for clarity of illustration.

The first experimental condition corresponded to fully tightened bolts. MEAS was positioned at the center of DE 34 quadrant and the MMI signature was measured in the lower kHz frequency range with the impedance analyzer. The impedance was measured with HP4192A impedance analyzer and the acquired curves were de-trended to eliminate inductive contribution as described previously. In the second test, bolt D4 was loosened by 1/8 turn and the corresponding impedance signature was measured. Keeping the condition of D4 unaltered, in the third test, bolt D3 was loosened by 1/8 turn. Subsequent tests involved loosening bolts E3 and E4 by 1/8 turn. As a result, upon loosening of E4, all four bolts in the quadrant were loosened by 1/8 turn. Finally, to distinguish between slightly loosened and fully loosened conditions all bolts were completely untied, but remained in the panel. The MMI data corresponding to the described tests are presented in Figure 82. Noticeable in the figure, incremental loosening of individual bolts in the quadrant results in shifting position of impedance peaks toward lower frequencies. It is suggested that lowering of impedance frequencies may indicate a reduction of stiffness in the joint. Interestingly, the amount of the shift is not the same for each peak frequency. This advocates for higher sensitivity of certain frequencies to investigated stress conditions. For example, there is a substantial difference between MMI 7 kHz peaks corresponding to fully tightened bolts and loosened D4. The difference is smaller at 5 kHz and is very small at 6 kHz. Similar dependence is observed for another extreme case involving MMI responses associated with E3 and E4. Loosening of the last bolt E4 produced little difference at 7 kHz, some difference at 5.5-6 kHz and substantial difference at 5 kHz.

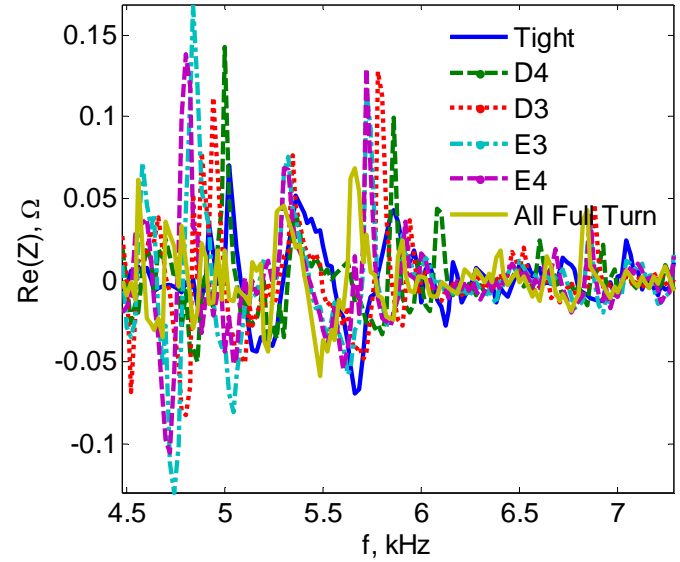


Figure 82 MMI characteristics of the DE34 quadrant during incremental loosening of structural bolts.

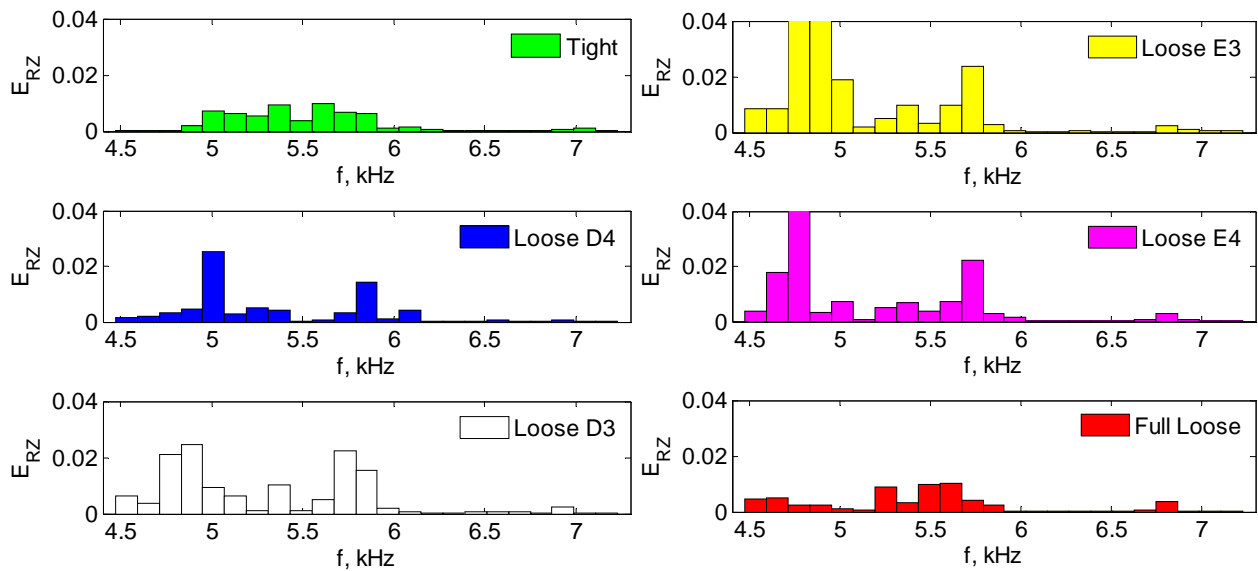


Figure 83 Energy distributions calculated for MMI responses obtained in the MMI characteristics of the DE34 quadrant (incremental loosening).

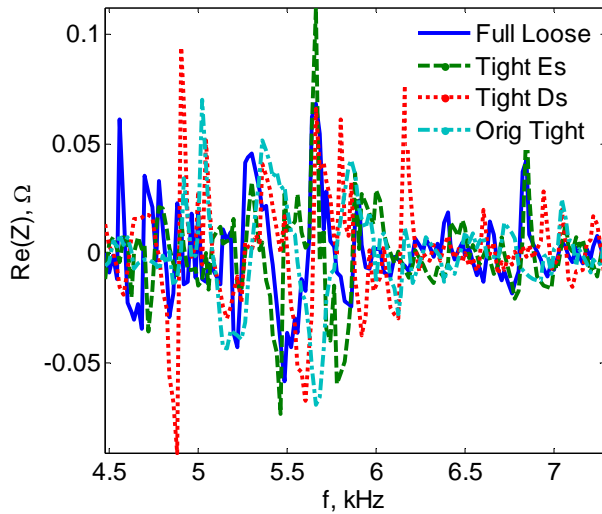


Figure 84 MMI characteristics of the DE34 quadrant during incremental tightening of structural bolts.

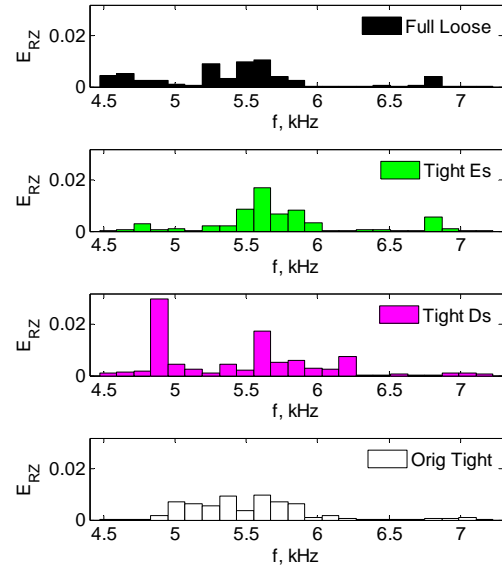


Figure 85 Energy distributions calculated for MMI responses obtained in the MMI characteristics of the DE34 quadrant (incremental tightening).

Based on the observations above, it is recommended that several impedance peaks, rather than a single peak, be considered for damage detection. This is achieved by considering energy distributions rather than isolated impedance peaks. Figure 83 shows energy distributions calculated for the data in accordance with the procedure described in the MMI repeatability test. The figure shows a distinct difference between energy distributions, with noticeable energy shift towards lower frequencies, as the stiffness of the joint decreases.

The second set of experiments started with the fully loosened condition on all four bolts in the quadrant. Then bolts E3 and E4 were fully tightened, followed by bolts D3 and D4. Magneto-mechanical impedances measured at indicated conditions of the joint are presented in Figure 84. The data generally follows the trend observed in the first set of experiments; a stiffer joint leads to higher frequency impedance peaks. Likewise, analysis of Figure 84 indicates differences in damage sensitivity for the peaks in impedance spectra. The most important observation inferred from Figure 84 is that, although sharing many similar features, responses corresponding to the originally tightened and re-tightened D bolts are not exactly the same. Therefore, the impedance data indicates hysteresis. This is of no surprise, because the bolts might be tightened to slightly different torques during the two sets of tests. Energy distributions for MMI, measured during incremental tightening, are illustrated in Figure 85. As can be seen from the figure, energy tends to shift towards higher frequencies during re-tightening of bolts. Although both show increased energy densities at high frequencies, energy distributions for conditions of originally tightened and re-tightened bolts are not the same. The mismatch is attributed to difficulties in replicating the original torques exactly. Additional details on this study may be found in publication Doyle et al., (2009).

2.5.3 Multiple Harmonic Resonance Tests

Capability of the Ritec measurement system to monitor harmonics of the fundamental frequency was explored to monitor harmonic response of dog-bone described above. Frequency response of such a specimen is presented in Figure 86, which illustrates a fundamental component (F) curve and curves associated with second (2F) and third (3F) harmonics of the fundamental frequency. As it could be seen in the figure, although a fundamental component curve features well defined response peaks, this could

be hardly postulated for curves associated with the second and third harmonics. This observation suggests that elastic wave amplitude at these harmonics lies within noise and, in the current MEAS design, is impractical to measure for application in SHM.

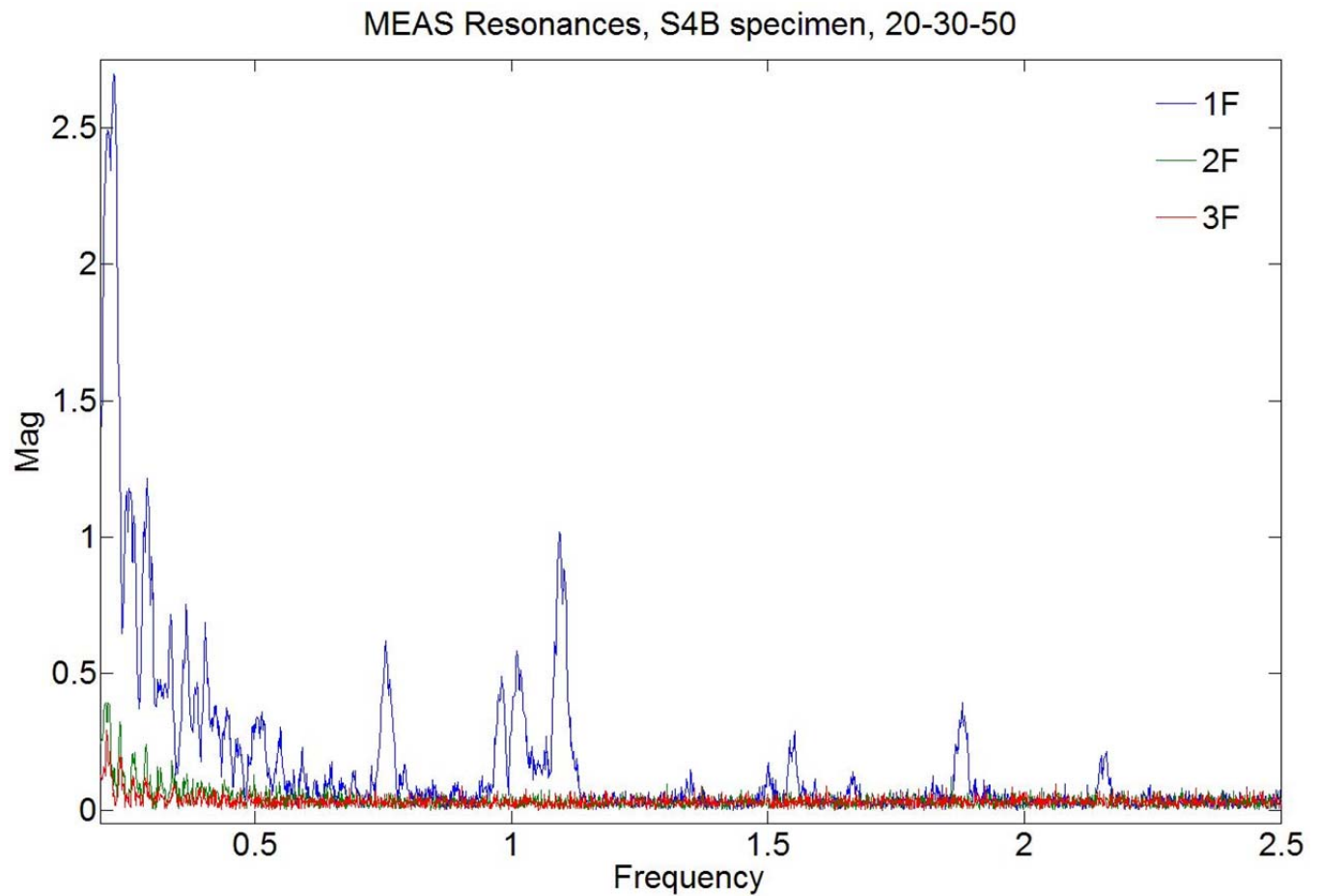


Figure 86 Frequency responses of the S4B dog-bone specimen measured using Ritec at fundamental and harmonic (2nd and 3rd) frequencies.

2.6 Magneto-Elastic Sensing during Sub-orbital flight

New Mexico Institute of Mining and Technology (NMIMT) designed, developed and launched scientific and educational payload on SL-5 suborbital flight of a commercial Space Loft vehicle provided by UP Aerospace. The aim of NMIMT's suborbital tests was to (a) verify ability of magneto-elastic active sensors, MEAS, to monitor dynamics of the payload during launch, flight duration, and landing, (b) investigate effects of launch, space, and re-entry environments on piezoelectric active sensors, (c) evaluate performance of sensor adhesive in the above mentioned environments, (d) monitor integrity of payload's bolted joints during suborbital space flight, (e) educate and train a new generation of engineers on design, assembly and testing of spacecraft's payload and sensors.

The SpaceLoft® XL has an overall height of 20.0 feet, a maximum diameter of 10.4 inches, and a maximum lift-off weight (including payload) of 780 pounds in its standard mission configuration. It can transport up to 110 pounds of payloads and experiments to a nominal apogee of 72 miles. With lower-mass payloads, the rocket can be configured to reach 140 miles. For maximum trajectory accuracy, the SpaceLoft® XL vehicle is spun during the boost portion of the flight. The nominal spin rate is 6.9 cycles per second, which is typically achieved within 12.0 seconds into the flight. Once the vehicle is out of the atmosphere the booster is separated and our de-spin system is automatically deployed which results in a residual rotational rate of less than 5 degrees / second. An illustration of the rocket is available in Figure 87.



Figure 87 SpaceLoft XL vehicle. (www.upaerospace.com).

The payload was designed to be housed within 4" (height) by 9.95" (diameter) cylindrical enclosure with a total weight not exceeding 4 lb. shows interior of the payload. Elements of the payload that are essential for this project can be seen in the bottom left corner of the photograph and include C7 MEAS bonded to the bottom aluminum plate using Hyson epoxy, a custom board housing "power on" switch and MEAS amplifier, and CMS12D evaluation board providing interface for HC12 microcontroller unit for triggering on-board experiments and MEAS data storage. This electronics draws power from high capacity 9 volts battery located under the sensor box to the right from MEAS.

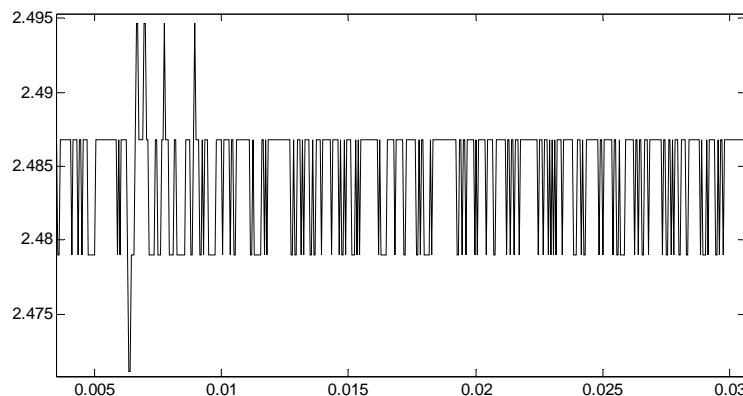


Figure 88 Example of MEAS record collected during laboratory testing.

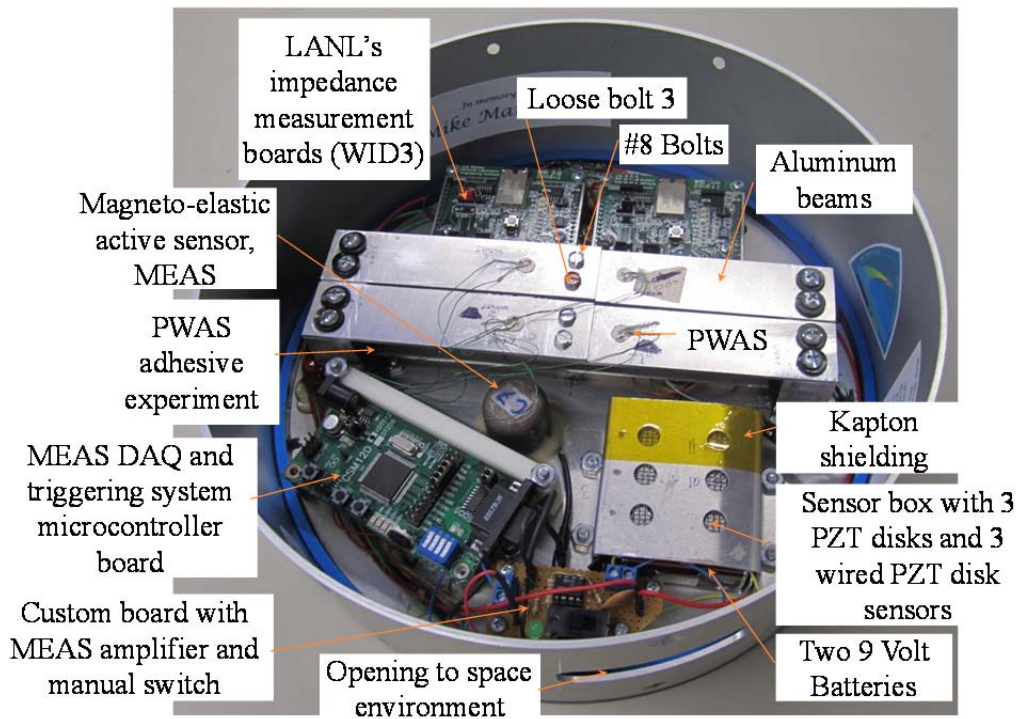


Figure 89 Interior of NMIMT payload.

As the microcontroller was not able to record data continuously due to memory limitations, a data acquisition sequence was devised to provide MEAS data records during all stages of the suborbital flight. In the presented setting, MEAS was configured to record only transient dynamics of the payload. Bandwidth of the microcontroller precluded recording of high frequency components of the dynamic response above 25 kHz. Example of MEAS measurement of payload dynamics during laboratory tests is presented in Figure 88. Low resolution precluding analysis of signal components is evident in the figure. Unfortunately, due to time constraints, no other microcontroller unit was available for integration in the payload. MEAS data recorded during the flight is presented in Figure 91 through Figure 92. A photograph of the SL5 rocket leaving the launch pad and flight profile is presented in Figure 93. Figure 94 provides altitude and acceleration data measured by ground control station and non-NMIMT participating team.

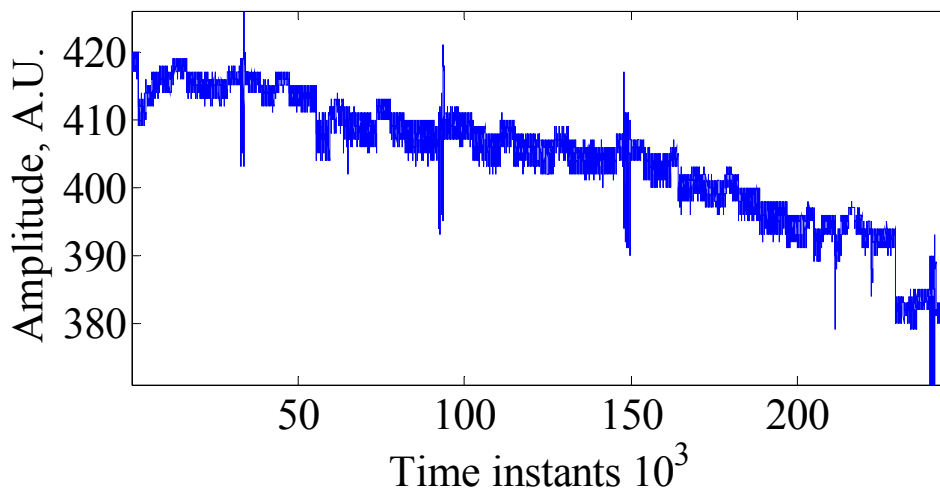


Figure 90 Unsynchronized MEAS in-flight data downloaded from the microcontroller unit.

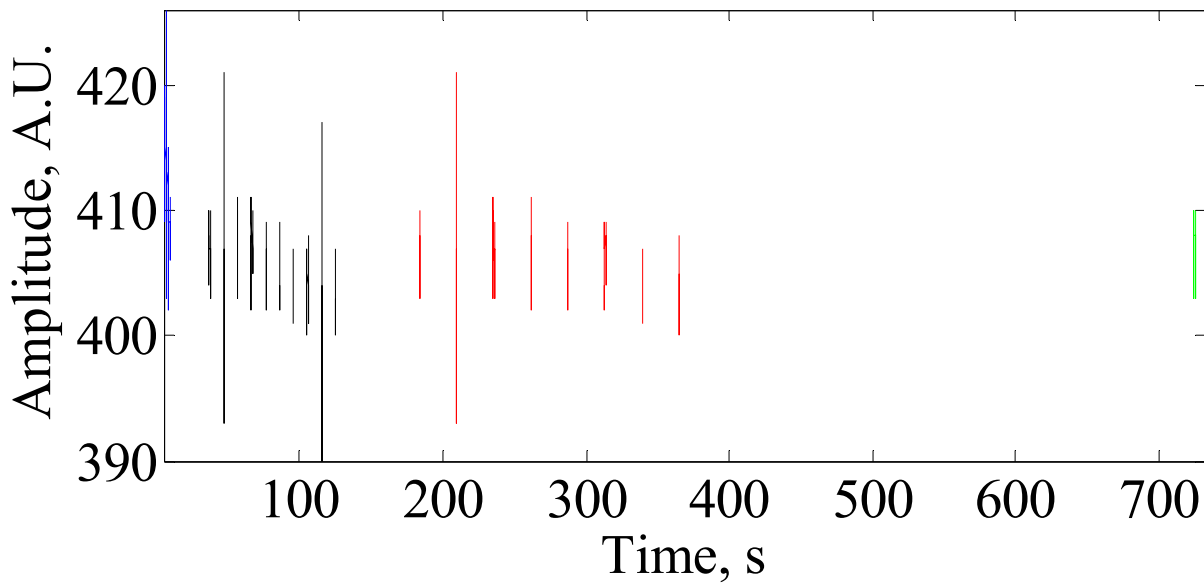


Figure 91 MEAS record during SL5 flight.

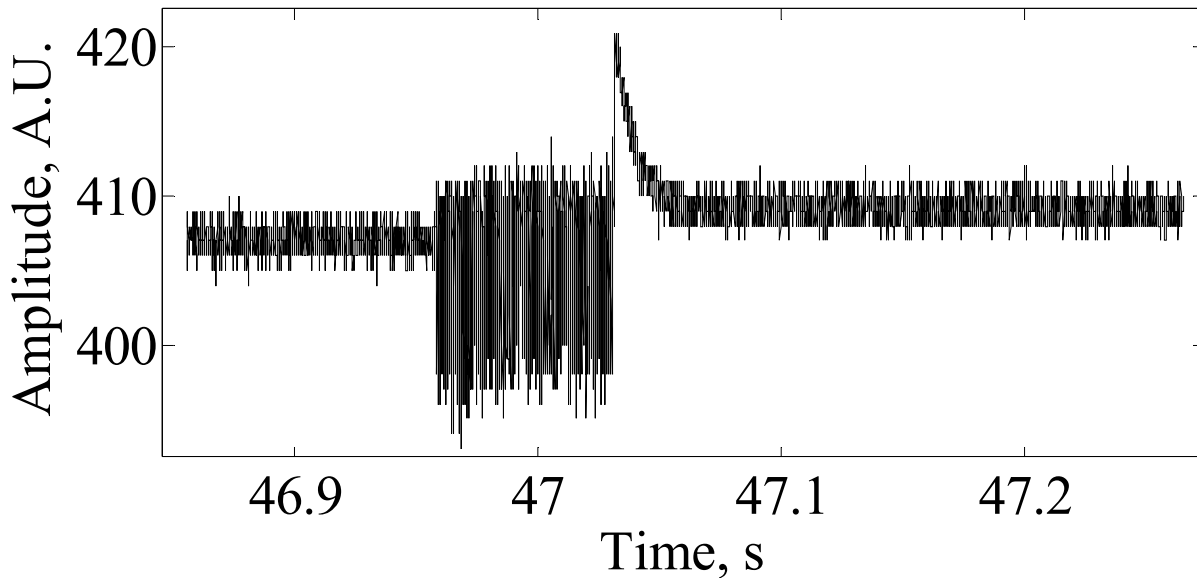


Figure 92 Zoom into MEAS in-flight record.

MEAS data recorded during flight suggest some correlation with accelerometer data, especially at the beginning and end of the flight. However, it is also likely that between 50 s to 300 s MEASE recorded parts on the payload dynamic activity which is shown as elevated noise in accelerometer data. Due to low sampling rate and saturation of MEAS data, amplitude level and frequency content of dynamics measured with MEAS may not be estimated accurately. Therefore, it is suggested that although MEAS has demonstrated ability to sense dynamic signal during SL5 mission, quality of the record is not sufficient to draw definite conclusions pertaining characteristics of the observed dynamic signal. This aspect of MEAS data acquisition must be improved in future investigations.

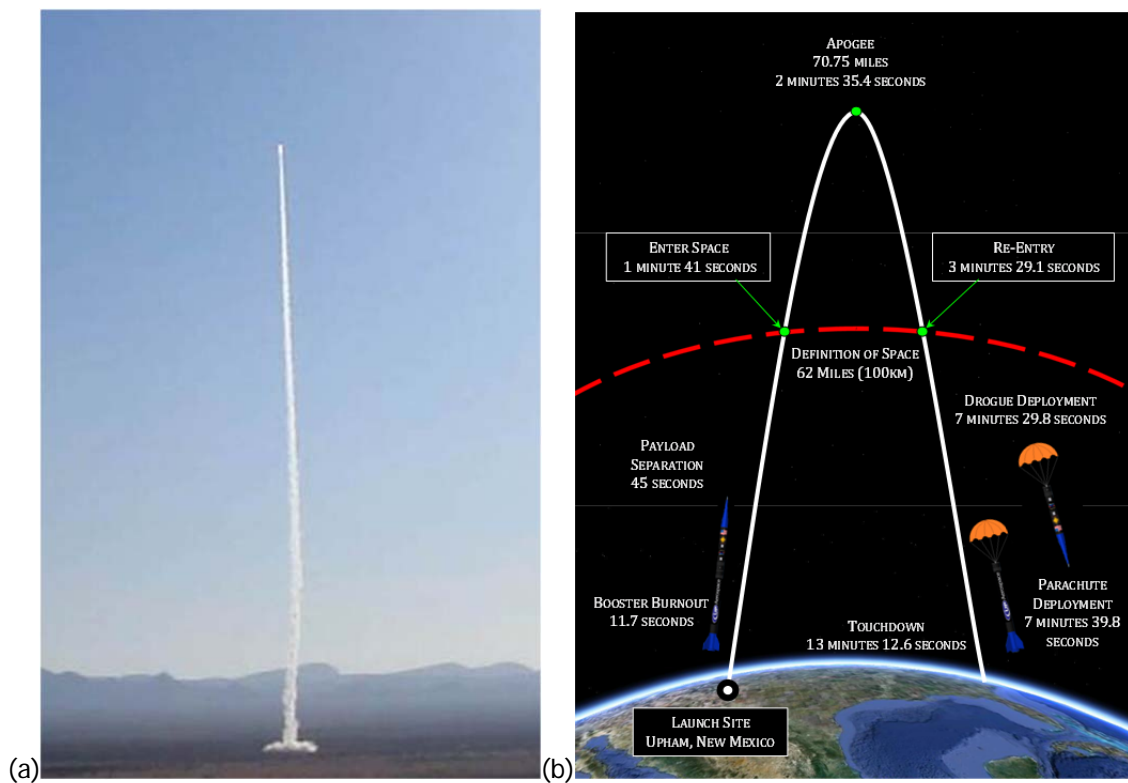


Figure 93 SL5 launch on May 20, 2011; (b) flight profile of SL5.

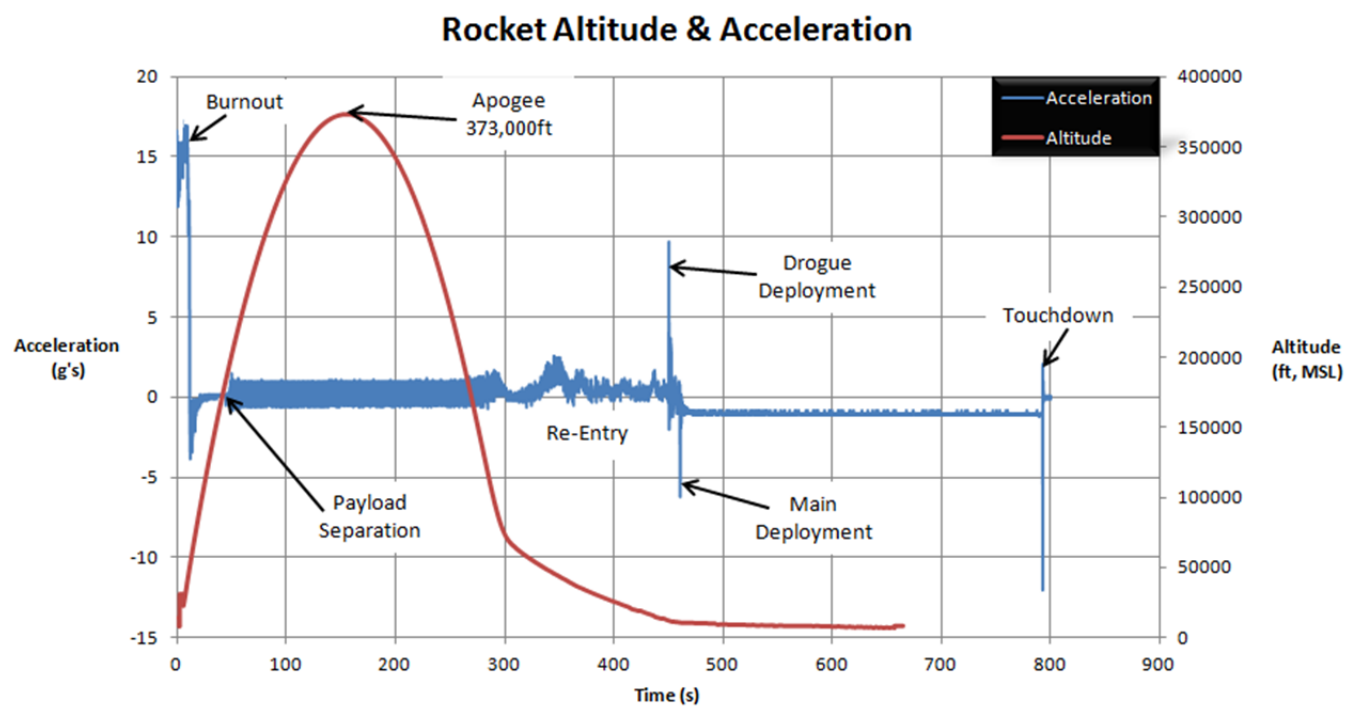


Figure 94 Altitude and acceleration of SL5 rocket.

3 CONCLUSIONS

Magneto-elastic sensors (MEAS) developed in this project have shown utility in acousto-ultrasonic SHM. MEAS constitutive components and characteristics were investigated to yield small and rather intrusive sensors for use in embedded diagnosis or non-contact inspection. Optimization and miniaturization were carried out to achieve a fragile balance of participating design factors such as MEAS size, magnet strength, shielding, and others. Pancake MEAS has shown capability to transmit and receive elastic waves; guided waves of S_0 and A_0 modes in particular. Two types of shear wave MEAS were designed, developed and fabricated. However, neither of these designs has demonstrated capability for MEAS to MEAS shear-wave transduction. It is suggested that in present form, there is not enough signal strength to support shear-wave SHM with current MEAS technology. Other types of wave, however, are available and may be used for a variety of SHM approaches.

A number of MEAS models were considered, which includes a transformer-based model in MMI, a heuristic model considering MEAS coil as a collection of point sources and a finite element 2-D model that accounted for complex field distribution in the MEAS and host structure. Analytical and numerical models for magneto-mechanical impedance were developed. Analytical model has demonstrated insights into participating physical effects, explained several key magneto-elastic manifestations and agreed well with experimental data.

Magneto-mechanical impedance (MMI) technology has been developed that allows for assessment of magneto-mechanical response of structures in the lower kHz frequency band. This technology is analogous to dynamic testing with MEAS acting both as actuator and sensor. However, in contrast to mechanical vibration methods, MMI includes both mechanical and electrical responses of the host structure. The technology has been successfully used not only for structural dynamic identification, but also for damage assessment in simple and complex metallic structures. A unique aspect of MMI application to monitoring fatigue damage was ability of MMI non-contact measure fatigue accumulation before onset of fracture and crack development, which opens a broad spectrum of opportunities in prognosis.

Ultrasonic detection of various types of damage using MEAS was considered. Similar to conventional ultrasonic transducer, MEAS has demonstrated effectiveness in detection of simulated and real cracks. It was demonstrated that a crack in the immediate vicinity of the sensor may affect generation of elastic waves by MEAS and hence can be detected. MEAS was also effective in detecting delamination in a honeycomb panel, but pitch catch method was preferable over the pulse-echo method.

Nonlinear SHM with MEAS has been considered. MEAS was effective in measuring extreme conditions (i.e. “loose” or “tight”) of the acousto-elastic response of bolted joints both in terms of amplitude and phase of elastic wave. However, it was not effective in quantifying a particular torque on bolt. This deficiency is associated with low amplitude of elastic waves generated by MEAS and will be improved as more powerful transducers considered in future. MMI method was able to furnish information on the integrity of bolted joints and detection of “loose” bolts was demonstrated on a realistic satellite panel. However, our experiments have demonstrated that multiple harmonics and combination frequencies are difficult to measure with MEAS primarily due to its low efficiency and signal generator and receiver. This aspect should improve as more powerful transducers will be introduced in future, but at the current level of development, nonlinear measurements using MEAS are not at the level of reliability to recommend them for effective SHM.

Capability of MEAS to measure dynamics of the payload during sub-orbital flight has been evaluated. MEAS did provide indications of transient dynamics, but characteristics of the dynamic response could not be evaluated due to amplitude saturation and low sampling of MEAS data. However, results of sub-orbital tests suggested possibility of using MEAS in space environment.

4 PROJECT PERSONNEL

Faculty

Dr. Andrei Zagrai (Project PI) and Dr. Rakhim Aitbaev (1 month during summer 2011)

Graduate students

Timothy Barnes, Vlasi Gigineishvili, Davit Kukhalashvili, Akshin Bakhtiyarov, David Conrad, and Andrew Murray.

Undergraduate students

William Reiser and Jaclene Gutierrez

5 PUBLICATIONS

5.1 Journal papers

1. Zagrai, A. and Çakan, H., (2010) “Magneto-mechanical Impedance Identification and Diagnosis of Metallic Structures,” International Journal of Engineering Science, Vol. 48, Issue 10, October 2010, pp. 888-908.
2. Doyle, D., Zagrai, A., Arritt, B., Çakan, H., (2009) “Damage Detection in Bolted Space Structures,” Journal of Intelligent Material Systems and Structures, Vol. 21, N. 3, pp. 251-264, first published on November 25, 2009.
3. Zagrai, A., (2009) “Emerging Technologies for Structural Damage Detection and Evaluation,” i-manager’s Journal on Future Engineering and Technology, Vol. 4, N. 2, November 2008 – January 2009, pp. 1-16.
4. Zagrai, A (2008) “Magneto-Mechanical Impedance of Metallic Structures,” published online 22 December 2008 in the Journal of the Acoustical Society of America (JASA), Vol. 125, N. 1, January 2009, pp. EL1-EL7.

5.2 Conference papers

1. Conrad, D. and Zagrai, A., (2011) “Active Detection of Structural Damage in Aluminum Alloy using Magneto-Elastic Active Sensors (MEAS),” Proceedings of ASME Conference on Smart Materials, Adaptive Structures and Intelligent Systems, paper: SMASIS2011-5219.
2. Murray, A., Zagrai, A., Conrad, D. (2011) “Diagnosis of Space Structures Using Embedded Sensors and Elastic Waves,” ” SPIE's 18th Annual International Symposium on Smart Structures and Materials and 16th Annual International Symposium on NDE for Health Monitoring and Diagnostics, 6-10 March 2011, San Diego, CA, v 7984. paper 7984-22, pp. 79840N-1-12.
3. Barnes, T., Kukhalashvili, D., Zagrai, A., (2010) “Magneto Elastic Active Sensors for Structural Health Monitoring using Magneto-Mechanical Impedance and Elastic Wave Propagation,” Proceedings of SPIE, v 7650, n PART 1, paper 7650-55, pp. 76501L-1-12.
4. Barnes, T., Zagrai, A.N. Kukhalashvili, D., Doyle, D., Arritt, B., Gardenier, H., (2009) “Development of Magneto-Elastic Active Sensors (MEAS) for Damage Detection in Aerospace Structures,” Proceedings of 7th IWSHM, 9-11 September 2009, Stanford University, CA, pp. 1096-1103.
5. Zagrai, A., Doyle, D., Barnes, T., (2009) “Ultrasonic Assessment of Satellite Structural Components and Joints,” Proceedings of SPIE , v 7295, pp. 729508-1-13.
6. Doyle, D., Zagrai, A., Arritt, B.J., Çakan, H., (2008) “Damage Detection in Satellite Bolted Joints,” Proceedings of ASME Conference on Smart Materials, Adaptive Structures and Intelligent Systems, paper: SMASIS2008-550.

6 ACKNOWLEDGMENTS

Authors would like to acknowledge Air Force Office of Scientific Research for funding this study and program manager Dr. David Stargel for valuable advice during the course of the project. Our deep gratitude is to AFRL/RVSV, Kirtland Air Force Base and its personnel Brandon Arritt, Hugh Gardenier, Whitney Reynolds and Derek Doyle for supporting and guiding reported research activities.

7 REFERENCES

- Aliouane, S, Hassam, M., Badidi-Bouda, A., and Benchaala, A., Electromagnetic Acoustic Transducers (EMATs) Design Evaluation of their Performances, <www.ndt.net/article/wcndt00/papers/idn591/idn591.htm> (2000).
- American Society for Testing and Materials 2007. Standard Test Methods for Tension Testing Wrought and Cast Aluminum-and Magnesium-Alloy Products [Metric]. West Conshohocken, PA: ASTM International.
- Banik, N.C. and Overhauser, A.W., (1977) "Electromagnetic Generation of Ultrasound in Metals," *Physical Review B Volume 16, number 89*.
- Barnes, T., Zagrai, A.N. Kukhalashvili, D., Doyle, D., Arritt, B., Gardenier, H., (2009) "Development of Magneto-Elastic Active Sensors (MEAS) for Damage Detection in Aerospace Structures," Proceedings of 7th IWSHM, 9-11 September 2009, Stanford University, CA, pp. 1096-1103.
- Boller, Christian (Editor), Chang, Fou-Kuo (Editor), and Fujino, Yozo (Editor), Encyclopedia of Structural Health Monitoring, John Wiley & Sons Inc. (2009).
- Boonsang, S, and Dewhurst, R.G., "A Sensitive Electromagnetic Acoustic Transducer for Picometer-Scale Ultrasonic Displacement Measurements", *Elsevier Sensors and Actuators A:Physical*, <www.elsevier.com/locate/sna> (May 2005).
- Cartz, L., (1995) Nondestructive Testing, ASM International, 1995.
- Davit Kukhalashvili (2010) "Experimental and Numerical Investigation of Magneto-Mechanical Impedance Method for Structural Health Monitoring of Aluminum Structures," MS thesis, New Mexico Institute of Mining and Technology.
- Doyle, D., Zagrai, A., Arritt, B., Çakan, H., (2009) "Damage Detection in Bolted Space Structures," Journal of Intelligent Material Systems and Structures, Vol. 21, N. 3, pp. 251-264, first published on November 25, 2009.
- Dutton, B, Boonsang, S., and Dewhurst, R.J. "Modeling of Magnetic Fields to Enhance the Performance of an in-plane EMAT for Laser-Generated Ultrasound", *Elsevier Ultrasonics*, <www.elsevier.com/locate/ultras> (June 2006).
- Fortunko, C. M. and Thompson, R. B. "Optimization of Electromagnetic Transducer Parameters for Maximum Dynamic Range," *IEEE Ultrasonics Symposium*, (1976).
- Giurgiutiu, V., (2007) Structural Health Monitoring with Piezoelectric Wafer Active Sensors, Academic Press.
- Hirao, M. and Ogi, H., (2003) EMATs for Science and Industry.
- Houck, J.R, Bohm, H.V. Maxfield, B.W., and Wilkins, J.W., (1967) Direct electromagnetic Generation of Acoustic Waves, *Physic Letters Volume 19*, (1967).

- Jian, X, and Dixon, S. Enhancement of EMAT and Eddy Current Using a Ferrite Back-Plate, *Elsevier Sensors and Actuators A: Physical*, <www.elsevier.com/locate/sna> (October 2006).
- Liang, C., Sun, F. P., and Rogers C. A., (1994) "Coupled Electro-Mechanical Analysis of Adaptive Material System-Determination of the Actuator Power Consumption and System energy Transfer", *Journal of Intelligent Material Systems and Structures*, V.5, Jan. 94, p 12-20.
- Maxfield, W., Linzer, B. M., McConnaughey, W. B. and Hulbert, J. K. "Design of Permanent Magnet Electromagnetic Acoustic-Wave Transducers (EMATs)," *IEEE Ultrasonics Symposium*, (1976).
- Norris, A.N., (1997) "Finite-Amplitude Waves in Solids," in *Nonlinear Acoustics* edited by Hamilton, M.F. and Blackstock, D.T., Academic Press, 1997.
- O'Malley, J. (1992) *Schaum's Outline of Theory and Problems of Basic Circuit Analysis*, McGraw-Hill, 1992.
- Park, G., Sohn, H., Farrar, C. R., and Inman, D. J., (2003) "Overview of Piezoelectric Impedance-Based Health Monitoring and Path Forward", *The Shock and Vibration Digest*, Vol. 35, No. 6, November 2003, pp. 451-463.
- Park, S., Park, G., Yun, C-B., and Farrar, C.R. (2009) "Sensor Self-diagnosis Using a Modified Impedance Model for Active Sensing-based Structural Health Monitoring," *Structural Health Monitoring*, January 2009; vol. 8, 1: pp. 71-82.
- Petersen, Gary. L-Matching the Output of a RITEC Gated Amplifier to an Arbitrary Load, <www.RitecInc.com>, (1995).
- Petersen, Gary. Winding solenoid inductors for use in high power matching networks, <www.RitecInc.com>, (2000).
- Placko, D., and Kundu, T., (2007) "DPSM for Modeling Engineering Problems," Wiley-Interscience.
- Quinn, J.J, (1967) "Electromagnetic Generation of Acoustic Waves and the Surface Impedance of Metals," *Physics Letters Volume 25A*.
- Sodano, H.A., Bae, J.S., Inman, D.J. and Belvin, W.K., (2006) "Improved Concept and Model of Eddy Current Damper," *ASME Journal of Vibration and Acoustics*, Vol. 128, pp. 295-302.
- Timothy Barnes (2010) "Development and Application of Magneto-Elastic Active Sensors for Structural Health Monitoring," MS thesis, New Mexico Institute of Mining and Technology.
- Turner, R., Lyall, K.R. and Cochran, J. F. (1969) "Generation and Detection of Acoustic Waves in Metals by Means of Electromagnetic Radiation," *Canadian Journal of Physics*, Vol. 47, N. 21, pp. 2293-2301.
- Wilcox, P.D., Lowe, M.J.S. and Cawley, P., "Omnidirectional Guided-Wave Inspection of Large Metallic Plate Structures Using an EMAT Array," *IEEE Transactions on Ultrasonics, Ferroelectrics, and Frequency Control*, vol. 53, no. 4, (April 2005).
- Wilcox, P.D., Lowe, M.J.S. and Cawley, P., "The Excitation and Detection of Lamb waves with Planar Coil Electromagnetic Acoustic Transducers," *IEEE Transactions on Ultrasonics, Ferroelectrics, and Frequency Control*, vol. 52, no. 12, (December 2005).
- Zagrai, A. (2009) "Magneto-Mechanical Impedance of Metallic Structures," *Journal of the Acoustical Society of America (JASA)*, Vol. 125, N. 1, January 2009, pp. EL1-EL7.
- Zagrai, A. and Çakan, H., (2010) "Magneto-mechanical Impedance Identification and Diagnosis of Metallic Structures," *International Journal of Engineering Science*, Vol. 48, Issue 10, October 2010, pp. 888-908.

- Zagrai, A., Doyle, D., Barnes, T., (2009) "Ultrasonic Assessment of Satellite Structural Components and Joints," Proceedings of SPIE , v 7295, pp. 729508-1-13.
- Zagrai, A.N. and Çakan, H., (2007) "Magneto-Mechanical Impedance Technique for Dynamic Identification of Metallic Structures," Proceedings of 6th International Workshop of Structural Health Monitoring, 11-13 September 2007, Stanford University, California, pp. 1693-1700.